A NUMERICAL INVESTIGATION OF TURBULENT NATURAL CONVECTION IN A 3-D ENCLOSURE USING *k-ω SST* MODEL AND PISO METHOD

KIMUNGUYI KILISWA JOSEPHS (M.Sc)

REG. NO. I84/22819/2011

A Thesis submitted in fulfillment of the requirements for the award of the degree of Doctor of Philosophy in Applied Mathematics in the school of Pure and Applied Sciences of Kenyatta University

OCTOBER, 2016

DECLARATION

This thesis is the result of my own work and includes nothing which is the outcome of work done in collaboration and neither has it been presented for a degree in any other University nor any other award.

KIMUNGUYI KILISWA JOSEPHS

REG. NO. I84/22819/2011

KENYATTA UNIVERSITY

SIGNATURE …… DATE

…….....

We confirm that the work reported in this thesis was carried out by the candidate under our supervision;

DR. AWUOR KENNEDY OTIENO

SCHOOL OF PURE AND APPLIED SCIENCES

KENYATTA UNIVERSITY

SIGNATURE …….. DATE

……..

PROF. FRANCIS KIMANI GATHERI

SCHOOL OF MATHEMATICS AND ACTUARIAL SCIENCES

TECHNICAL UNIVERSITY OF KENYA

SIGNATURE …….. DATE

……..

DEDICATION

I would like to dedicate this thesis to my mama Teresa Nasambu, my papa Jackson Mahaya, my wife Sarah Njeri and my children Mahaya Jacksons, Trizah Nasambs and Njoroge Davids, for their love, prayer, inspiration, support and encouragement.

ACKNOWLEDGEMENTS

The interest, guidance, encouragement and academic insight of my doctoral supervisors, Professor Francis K. Gatheri of Technical University of Kenya and Dr. K. O. Awuor of Kenyatta University, has been invaluable over the last three years. They have been very generous with their time and energy, and I have learnt an enormous amount from them. For me, they not only went an extra mile but went out of their way. It has been a privilege working with them and as my destiny connectors, mentors and academic parents, am greatly indebted to them and forever I shall be.

I wish to thank the Dean, School of Pure and Applied Sciences, Professor Joseph J. N. Ngeranwa, the past and present chairmen of mathematics department, Professor David Malonza and Dr. Benard Kivunge respectively, for their priceless encouragement and administrative guidance. My encounter with Prof. Leo. Odongo, Prof. I. N. Kamuti and Dr. Mutie Kavila, all of Mathematics department KU, inspired me to aspire for finer things in life without looking back.

My wife Sarah Njeri and my children Mahaya Jacksons, Trizah Nasambs and Njoroge Davids have always been bedrock of love, prayer and support. The trigger to think doctorate and the stimulus to pursue this degree have been from them. This is a wonderful gift which I am most grateful to God for. Without them, I wonder whom I would be running this race for!

My thanks go post humously to my late daddy Jackson Mahaya for modelling and horning my reading culture since childhood. My mummy has never ceased to pray and encourage me to be a man of excellence. Their parental blessings and the belief the two had in me have made me become who I am today. My appreciations would amount to naught if I did not thank God, the author and finisher of my faith. Through my spiritual father, Bishop Charles Meliyio, I know that He is faithful and 'for all the promises of God in Him are yea, and in Him Amen, unto the glory of God by us'.

ABSTRACT

In turbulent natural convection transport mechanism, fluid motion is generated by buoyancy-induced density gradients resulting from internal body forces due to heating. The objective of this study was to conduct a numerical investigation of turbulent natural convection in a 3-D cavity using the k-ω SST model and the PISO method. The problem being investigated was computational study of turbulent natural convective flow using a primitive variable to solve time averaged momentum equation instead of using the vorticity-vector potential formulation. The statistical-averaging process of the mass, momentum and energy governing equations introduces unknown turbulent correlations into the mean flow equations namely Reynolds stress *($\overline{u_\iota u_j}$)* and heat flux *($\overline{u_\iota \theta}$),* which were modeled using k-ω SST model. The RANS equations, energy and *k-ω* SST turbulent equations were first non-dimensionalized and the resulting equations were discretized using Finite Volume Method and solved using PISO and SIMPLEC algorithms. Second order upwind was set for the momentum and energy discretization equations. The residuals convergence criterion was such as to reduce the absolute residuals below of 1.0×10^{-6} for energy and 1.0×10^{-3} for continuity, momentum and k-ω SST turbulent equations. The solutions are presented at Rayleigh number of 1.58×10^{9}, an Aspect Ratio of 0.5 and Prandtl of air of 0.71. The results were then validated using experimental benchmark results. The results showed that use of PISO method improves convergence time and speed, improves computational effort per unit time, absolute error in the solution of flow variables diminishes faster, the Pressure term is solved and as a result, profiles for wall shear stress and static pressure have been obtained and convective heat transfer is more significant than conduction in turbulent natural convection in a 3-D cavity. The

velocity and thermal profiles obtained are important for thermal comfort, efficiency of energy balance and the effectiveness of the ventilation system when modeling air flow in buildings.

TABLE OF CONTENTS

LIST OF TABLES

LIST OF FIGURES

VELOCITY VECTORS BY SIMPLEC

NOMECLATURE

A_1, A_2, A_3	**Dimensionless Parameter**
A	**Aspect ratio**
B_1, B_2, B_3, B_4	**Dimensionless parameter**
c_p	**Specific heat at constant pressure**
c_μ	**Empirical constant**
e	**Specific internal energy**
F	**Body force**
g	**Acceleration due to gravity**
G_k	**Buoyant Production of turbulent kinetic energy**
h	**Mesh interval /Static enthalpy**
i, j, k	**Integer variables**
k	**Kinetic energy of turbulence**
L_1, L_2, L_3	**Dimensionless parameters**
n	**Co-ordinate normal to the boundary**
Nu	**Nusselt number**
P	**Thermodynamic pressure**
P_k	**Shear production of turbulent kinetic energy**
Q	**Non-dimensional heat transfer**
q_j	**Conductor vector**
s	**Specific entropy**
S_Q	**Source terms**
t	**Time**
T	**Thermodynamic temperature**

T_o	**Reference temperature**
u, u', U	**Instantaneous/fluctuation/mean velocity in x-direction**
U_*	**Characteristic velocity**
v, v', V	**Instantaneous/fluctuation/mean velocity in y-direction**
w, w', W	**Instantaneous/fluctuation/mean velocity in z-direction**
$(p_o^2 c_{Po} g\beta \Delta T L_o)/(\mu_o K_o) = Ra$	**Rayleigh-number**
$(\mu_o c_{Po})/(\mu_o c_{Po}) = Pr$	**Prandtl number**
$(\mu_o g/\rho_o)/(\mu_o g/\rho_o) = Gn$	**Gravity number**
$P_o/(P_o U_*^2) = Eu$	**Euler number**
$P_o/(c_{Po}\rho_o T_o) = Pn$	**Pressure number**
$P_o U_* L_o/\mu_o = Re$	**Reynolds number**
$U_*/gL_o = F_r$	**Froude number**
$\zeta = \Delta T_*/T_o$	**Non-dimensional Temperature Difference**
$\eta = \beta_o T_o$, $Ra/Pr = Gr$	**Grashof number**

GREEK SYMBOLS

α	**The thermal expansion coefficient**
β	**Coefficient of volumetric expansion**
∇	**Gradient operator**
Δt	**Time interval**

δ_{ij}	**Kronecker delta**
κ	**Turbulent kinetic energy**
ω	**Specific dissipation**
Γ	**Turbulent thermal diffusivity**
η	**Coefficient** $(= \beta_R T_R)$
Θ	**Non-dimensional mean temperature**
θ	**Non-dimensional/fluctuating temperature**
λ	**Thermal conductivity**
μ	**Dynamic viscosity**
ν	**The kinematic viscosity** $(= \mu/\rho_o)$**.**
ρ	**Density**
σ_T	**Turbulent Prandtl number in** Θ
σ_κ	**Turbulent Prandtl number in** κ
σ_ω	**Turbulent Prandtl number in** ω
τ	**Viscous stress tensor**
π	**Stress tensor**
Φ	**Dissipation function**
ϕ	**General variable**
φ	**The instantaneous fluid property**

SUPER SCRIPTS

b	**Boundary value**
c	**Cold wall**

h	**Hot wall**
i, j, k	**The $i-th, j-th, k-th$ mesh point**
o	**Reference state**

SUB SCRIPTS

$n-1$	**Previous time step**
n	**Current time step**
$n+1$	**Next time step**
$'$	**Fluctuation quantity**
$*$	**Guessed value**

ABBREVIATIONS AND ACRONYMS

ADI	**Alternating Directional Implicit**
CFD	**Computational Fluid Dynamics**
CPU	**Central Processing Unit**
DNS	**Direct Numerical Simulation**
Eq.	**Equation**
FDM	**Finite Difference Method**
Fig.	**Figure**
FVM	**Finite Volume Method**
LES	**Large Eddy Simulation**

MADP	**Mean Absolute Deviation Percentage**
MHD	**Magneto-Hydrodynamic**
PISO	**Pressure Implicit Splitting Operator Algorithm**
RANS	**Reynolds Averaged Navier Stokes Equations**
SIMPLE	**Semi Implicit Method for Pressure Linked Equations**
SIMPLEC	**SIMPLE-Consistent**
SST	**Shear Stress Transport**

CHAPTER ONE

INTRODUCTION

1.1 Background

In natural convention transport mechanism, turbulence is a flow regime characterized by chaotic and stochastic changes. This includes low momentum diffusion, high momentum convection and rapid variation of pressure and velocity in space and time. Turbulent flows exist everywhere in nature from the jet stream to the oceanic currents. Turbulent flows are highly irregular and random, they have high diffusivity, are non-linear and characterized by a strong, three-dimensional vortex stretching mechanism which makes them rotational, 3-D and transfers energy and vorticity to increasingly smaller scales until the flow gradients become so big that they are smeared out by molecular viscosity**.** Because of these properties, turbulent flows are very important to many engineering applications and industrial and agricultural systems**.**

1.2 Problem Statement and Justification

1.2.1 Problem Statement

Studies on simulating natural turbulent convection fluid flow in enclosures have been undertaken before. For instance, research on natural convention in an enclosure with localized heating and cooling was done by Gatheri (1997) and simulating natural turbulent convection fluid flow in an enclosure using the standard k-ε model by Sigey *et al.* (2004). Research has been concluded to obtain the model with the best approximation to the turbulent Reynolds stress in the RANS momentum equation by Awuor (2012). The study is about investigating the change in velocity profiles, temperature profiles, convergence time, stability and accuracy of the numerical code

and any additional findings for the case when the momentum equation is solved using the primitive variable by way of PISO and SIMPLEC algorithms.

1.2.2 Justification

In the previous related research by Awuor (2012), the vorticity-vector potential formulation is used to eliminate the need to solve the pressure term in the momentum equation. In this particular research, the pressure term is instead solved using the PISO method and SIMPLEC methods which apply the primitive variable, and hence this is likely to change everything in terms of obtained numerical data for temperature and velocity, during the assessment of the performance of *k-ω SST* model in predicting heat transfer due to natural convention in an air filled cavity. Thus research will be important to engineering, industrial and agricultural systems that require engineering solutions which depend on this kind of mathematical model.

1.3 Objectives

1.3.1 General Objective

To conduct a numerical investigation of turbulent natural convection in a 3-D enclosure using the *k-ω SST* model and the PISO method.

1.3.2 Specific Objectives

i. To obtain simulated data for the *k-ω SST* models for the temperature and velocity near the hot wall and the cold wall, using PISO and SIMPLEC algorithms.

ii. To compare simulated data for velocity and temperature, obtained using PISO algorithm, SIMPLEC algorithm and the two- equation *k-ω SST* model, near the hot wall and the cold wall.

iii. To determine the change in velocity profiles, temperature profiles, convergence time, stability and accuracy of the numerical method and any additional findings, when the primitive variable is employed to solve the pressure term as compared to the previous work undertaken by Awuor (2012) when the vorticity-vector potential formulation was used in solving the momentum equation.

iv. To determine the better method in terms of convergence, stability and accuracy between PISO method and SIMPLEC method in carrying out numerical investigation of turbulent natural convection of air in a 3-D cavity.

v. To validate the obtained numerical results using experimental data, make conclusions based on the obtained numerical data and make recommendations for future studies to be undertaken along this line of research.

1.4 Significance and Anticipated Output

i. In the work by Awuor (2012), when the vorticity-vector potential formulation was used in solving the momentum equation, the $k-\omega\,SST$ model took 1 hour to converge after 1000 iterations. It is anticipated that PISO method coupled with the $k-\omega\,SST$ model would reduce the CPU time for very large problems, higher speed flows and turbulent flows hence saving on computing resource requirement.

ii. The study is important in generating profiles upon which to model systems that facilitate room ventilation in residential buildings that hold large audiences like lecture theatres and indoor games auditoria.

iii. The data for thermal profiles found in this thesis would be helpful in determining and controlling the micro-climate in poultry houses for the thermal comfort of the birds through insulation of roofs, walls and floor, ventilation, heating, cooling and lighting.

iv. The manufacturing sector would equally benefit too as the studies would provide information for correct velocity and temperature fields for manufacturing processes, preservation, packaging and storage.

In the next chapter, we shall discuss the work done earlier on turbulent natural convection transport mechanism in order to lay the foundation for the mathematical formulation in investigating turbulent natural convection in a 3-D enclosure using the PISO algorithm, the SIMPLEC algorithm and the $k-\omega\ SST$ model.

CHAPTER TWO

LITERATURE REVIEW

2.1 Introduction

Air distributions in enclosed environments are crucial to thermal comfort, and computational fluid dynamics (CFD) has been playing an important role in evaluating and designing various air distributions. Enclosed environments, such as commercial, institutional, and residential buildings; healthcare facilities; sports facilities; manufacturing plants; animal facilities; transportation vehicles, are confined spaces with certain functionalities. It is therefore important and essential to control air distributions in the enclosed environments. Nielsen (1974) was the first one who applied CFD for airflow prediction in an enclosure. Generally, CFD predicts turbulent flows through three approaches: Direct Numerical Simulation (DNS), Large Eddy Simulation (LES), and Reynolds-Averaged Navier-Stokes (RANS) equation simulation with turbulent models.

Jones and Whittle (1992) described in detail the current capabilities of CFD in building simulation highlighting several advantages and disadvantages of turbulence modeling techniques:-

i) That the eddy viscosity method is robust and simple but when used with care can compute acceptable results.

ii) The k-epsilon model is the most widely used turbulence model as it is a compromise between level of sophistication and computational efficiency. One assumption in the k-epsilon model is that the flow is isotropic which is why the Reynolds stress model was introduced.

iii) The Reynolds stress model uses five differential equations in each cell of the domain making it better deal with swirling flows, but also making it more computationally expensive.

iv) The Large Eddy Simulation is an even more sophisticated type of turbulence modeling requiring very fine meshes. The LES model is still at the research stage and therefore not ready for use within engineering design.

v) The direct simulation or direct numerical simulation (DNS) approach solves the turbulence equations directly, with no simplification and requires large computational expense especially for large flow fields such as building simulations.

2.2 Natural Turbulent Convection

Natural turbulent convection in cavities attracts considerable interest from thermal scientists given that it can be found in many industrial and/or civil engineering applications such as energy transfer in rooms and buildings, nuclear reactor cooling, solar collectors and electrical component cooling. A significant number of experimental and theoretical works have been carried out in the past in an attempt to understand turbulent natural convective flows in enclosures.

Dol and Hanjalic (2001) carried out a computational study of turbulent natural convection in a side-heated cubic enclosure at a Rayleigh of 4.9×10^{10} using Reynolds Averaged Navier-Stokes equations (RANS) approaches. Their computations were performed with both 2-D and 3-D codes using low-Reynolds-number k-ε model and advanced second moment closures. They showed that second moment closures are better in capturing 3-D effects and strong streamlines curvature at

the corners. Davidson and Nielsen (1996) investigated the performance of low Reynolds *k-ω* model on turbulent buoyant convection flows with thermal stratification. The authors reported a problem commonly encountered at moderate Rayleigh numbers (Ra=$10^{10} - 10^{12}$)**:** when applying the *k-ω* model to buoyancy-driven cavity flows, the model is not capable of returning grid-independent predictions owing to the transition regime along the vertical walls. It was found that the buoyancy source term of the turbulence kinetic energy, G, exhibit strong grid sensitivity, as this term is modeled by standard gradient hypothesis. By introducing a damping function, the above grid dependence is eliminated. Furthermore, the modified G_k renders the correct asymptotic behavior near the vertical wall. Davidson and Nielsen (1996) did a numerical study to investigate a buoyant flow in a cavity with two differentially heated side walls by means of large eddy simulation.

Further research on natural convention in an enclosure with localized heating and cooling has been studied by Gatheri *et al.* (1994). Gatheri *et al.* (1994) further investigated how to use False Transient Factors for the Solution of Natural Convection Problems and has well done a parametric Study of an Enclosure with Localized Heating and Cooling, Gatheri (1997). Sigey (2004), not only did research on Numerical Free Convection Turbulent Heat Transfer in an Enclosure but also carried out parametric studies on a rectangular enclosure using the standard *k-ε* model. Further work on natural turbulent convection has been about the use of mesh generation for the solution of natural convection problems, Gatheri (2005), use of a variable False transient for the solution of Coupled elliptic Equations and use of Buoyancy Driven Natural Convection heat transfer in an enclosure and Magnetohydrodynamic (MHD) free convective flows past an infinite vertical porous plate with Joule heating, Gatheri (2005).

Okwoyo *et al.* (2013) did a numerical study of turbulent natural convection flow in a 3-D enclosure with heaters placed on opposite walls and two windows each on the adjacent opposite walls. The governing equations were discretized using three point central difference approximations for non-uniform mesh. The results, in form of velocity and temperature plots, showed the enclosure is stratified into hot region near the heater and cold region near the window. Areas that needed further investigation included

i) forced convection and its effect on temperature distribution temperature distribution and velocity profiles in a room
ii) a more practical approach to engineering in order to reduce theoretical assumptions in that work
iii) research of buoyancy driven natural convection in non-rectangular enclosures

Zimmermann (2014) did a numerical study of a turbulent natural convection problem with a compressible Large-Eddy Simulation. Density changes due to temperature differences are considered in the numerical model by a compressible coupled model. The fluid property profiles showed an asymmetry which is caused by the non-Boussinesq effects of the fluid. Points of further investigation in this study include

i) Use of an in-compressible turbulent model simulation
ii) Appearance of small deviations in the profiles from the similar results, mainly in the vicinity to the heated walls.

Hewitt (2014), investigated a range of porous convective systems at high Rayleigh number Ra number, using numerical, theoretical and experimental techniques. The convective systems included heat exchanger flow and high Ra porous convections in the presence of a thin, low permeability horizontal layer. Results showed that;

i) When using Direct Numerical Simulations show the nonlinear evolution of the instability results in a coarsening of the columnar flow

ii) The horizontal length scale of the plumes in the interior of the cell increases dramatically as Nusselt number Nu is increased and

iii) The presence of an interior low permeability layer can cause the Nusselt number to increase from the value in the homogeneous cell with no interior layer

Awuor (2012) did a study to assess the performance of three numerical turbulence models; $\kappa-\varepsilon, \kappa-\omega,$ and $\kappa-\omega\, SST$ to find the model with a better approximation to the experimental data in predicting heat transfer profiles due to natural convection inside an air filled cavity. This involved solving the momentum equation using vorticity vector potential formulation. To do this, the pressure gradient term is eliminated from the 2-D momentum equation by cross differentiating the two components of the momentum equation and subtracting them. The numerical data for the three models for velocity and temperature was obtained. The simulated data compared to the experimental data. It was found that $\kappa-\varepsilon$ model is ineffective at the boundaries with high temperature gradient and performs better in a free stream flows. It was further found that $\kappa-\omega\, SST$model accounts for the transport shear stress and gives highly accurate predictions of the amount of flow separation under adverse pressure gradients. Awuor (2012) further investigated the convergence time for the three models. The results showed that

$\kappa - \omega\ SST$ model is a more accurate layer simulation under high temperature gradient as compared with the $\kappa - \varepsilon$ and $\kappa - \omega$ models. A numerical data was then obtained for a test problem using the best model, $\kappa - \omega\ SST$ was found that the room is stratified into three regions: a cold upper region, a hot region in the area between the heater and a warm lower region.

Merits of using vorticity vector potential formulation were:

i) Pressure term is eliminated

ii) Equations need to be solved to get values of the stream function ψ and vorticity ζ

Demerits of using vorticity vector potential formulation included

i) Difficulty to specify boundary conditions for vorticity thus causing solution convergence issues

ii) Pressure is required for calculation of density, wall shear stress, static pressure profiles and other fluid properties

iii) To get pressure, vorticity is used which offsets computational saving

iv) Stream function does not exist in 3-D, so the method cannot be extended to 3-D

The research work by Awuor (2012) is the motivation behind this thesis because we seek to address the four challenges encountered when using of the vorticity vector potential formulation, as enlisted above, by using the primitive variable in solving the pressure term in the momentum equation instead of eliminating the term as was the case with vorticity vector potential formulation.

Chapter three discusses governing equations, turbulence, non-dimensionalisation and methodology for this numerical investigation of air in a 3-D enclosure.

CHAPTER THREE

MATHEMATICAL FORMULATION

3.1 Governing Equations

3.1.1 Introduction

The equations governing the flow of incompressible Newtonian fluid are derived from equations, which enforce the conservation of mass, the conservation of momentum, and conservation of energy. Equations governing natural convection in turbulent flow are represented by partial differential equations. These equations are then decomposed by expressing fluid properties as the sum of a mean and a fluctuating value.

3.1.2 Equation of Continuity

The equation is based on the law of conservation of mass. The law states that, the rate of increase of mass within a controlled volume is equal to the net rate of influx through the controlled surface. The general equation of continuity in Cartesian tensor notation according to Curie (1974) is;

$$\frac{\partial \rho}{\partial t} + \frac{\partial}{\partial x_j}\left(\rho u_j\right) = 0 \tag{3.1}$$

For steady state, equation (3.1) reduces to;

$$\frac{\partial}{\partial x_j}(\rho u_j) = 0 \tag{3.2}$$

This equation expresses the fact that, as a fluid flows, matter is neither created nor destroyed and that mass is conserved. The equation is applicable to any type of flow, compressible or incompressible.

3.1.3 The Momentum Equation

This equation is derived from Newton's second law of motion which states that the sum of the forces acting on a control volume must be equal to the rate of increase of fluid momentum within the control volume. In differential form, the Navier-Stokes equations can be expressed as;

$$\frac{\partial}{\partial t}\rho u_i + \frac{\partial}{\partial x_j}\rho u_i u_j = \rho F_i + \frac{\partial}{\partial x_j}(\pi_{ij}) \tag{3.3}$$

Where ρF_i represents the body force per unit volume and π_{ij} is the stress tensor, which for a Newtonian, according to White (1974), can be decomposed to;

$$\pi_{ij} = -P\delta_{ij} + \tau_{ij} \tag{3.4}$$

in which δ_{ij} is the kronecker delta and τ_{ij} is the viscous stress tensor, which is given by;

$$\tau_{ij} = \mu\left(\frac{\partial u_i}{\partial x_j} + \frac{\partial u_j}{\partial x_i}\right) + \mu_s\delta_{ij}\frac{\partial u_k}{\partial x_k} \tag{3.5}$$

where μ and μ_s are the first and second coefficient of viscosity respectively. Therefore;

$$\pi_{ij} = -P\delta_{ij} + \mu\left(\frac{\partial u_i}{\partial x_j} + \frac{\partial u_j}{\partial x_i}\right) + \mu_s\delta_{ij}\frac{\partial u_k}{\partial x_k} \tag{3.6}$$

Electromagnetic forces are not considered in this work and the force of gravity is the only body force. Hence, in equation (3.3), putting $F_i = g_i$ where g_i is the force due to gravity in the x_i direction. Substituting equation (3.6) into (3.3) yields the momentum equation;

$$\frac{\partial}{\partial t}\rho u_j + \frac{\partial}{\partial x_j}\rho u_i u_j = -\frac{\partial P}{\partial x_i} + \rho g_i + \frac{\partial}{\partial x_j}\left[\mu\left(\frac{\partial u_i}{\partial x_j} + \frac{\partial u_j}{\partial x_i}\right) + \mu_s \delta_{ij}\frac{\partial u_k}{\partial x_k}\right] \tag{3.7}$$

3.1.4 The Energy Equation

The energy equation is derived from the first law of thermodynamics. It states that the rate of energy increase in a system equals the heat added to the system and the work done on the system and is often written according to Curie (1974) as;

$$\rho\frac{Dh}{Dt} + \frac{\partial}{\partial x_j}\left(\rho u_j \mathrm{h}\right) = \frac{\partial p}{\partial t} + \frac{\partial}{\partial x_j}\left(u_j \mathrm{p}\right) - \frac{\partial q_j}{\partial x_j} + \Phi \tag{3.8}$$

where;

$$\Phi = \tau_{ij}\frac{\partial u_i}{\partial x_j} \tag{3.9}$$

is the dissipation function, h is the specific enthalpy and q_j is the local rate of heat transfer per unit area. In equation (3.9), the heat produced by the external has been neglected. The heat is modeled by Fourer's law, namely;

$$q_j = -\lambda\frac{\partial T}{\partial x_j} \tag{3.10}$$

in which λ is the thermal conductivity. Equation (3.8) can be simplified using the definition for specific enthalpy given as;

$$h = e + p/\rho \tag{3.11}$$

where e is the specific internal energy. In differential form, equation (3.11) becomes;

$$\mathrm{d}h = \mathrm{d}e + p\mathrm{d}(1/\rho) \tag{3.12}$$

Using the first and the second law of thermodynamics (Hatsopolous and Keenan, 1965), the change in specific enthalpy can be expressed as;

$$\mathrm{d}e = T\mathrm{d}s - p\mathrm{d}(1/\rho) \tag{3.13}$$

where s is the entropy. Substituting equation (3.13) into equation (3.12) yields;

$$\mathrm{d}h = T\mathrm{d}s + 1/\rho\, dp \tag{3.14}$$

Because entropy depends on the pressure and temperature, it can be written as;

$$\mathrm{s} = s(T, P)$$

$$\mathrm{d}s = \left(\frac{\partial s}{\partial p}\right)_T \mathrm{d}P + \left(\frac{\partial s}{\partial p}\right)_p \mathrm{d}T \tag{3.15}$$

and using the general thermodynamic relations (Hatsopolous and Keenan, 1965);

$$\left(\frac{\partial s}{\partial p}\right)_T = -\frac{\beta}{p}, \qquad \left(\frac{\partial s}{\partial p}\right)_P = \frac{C_P}{T}, \qquad \left(\frac{\partial [\frac{1}{\rho}]}{\partial T}\right)_T = -\frac{\beta}{p}$$

Hence equation (3.15) simplifies to;

$$\mathrm{d}s = -\frac{\beta}{p}\mathrm{d}P + \frac{C_P}{T}\mathrm{d}T \tag{3.16}$$

in which β is the volumetric coefficient of expansion and C_P is the specific heat at constant pressure. Substituting equation (3.16) into equation (3.14) results to;

$$\mathrm{d}h = C_P\mathrm{d}T + \frac{1}{\rho}(1 - \beta T)dp \tag{3.17}$$

Substituting equations (3.17) and (3.10) into equation (3.8) makes the final form of the energy equation to be;

$$\frac{\partial}{\partial t}(C_P \rho T) + \frac{\partial}{\partial x_j}(C_P \rho u_j T) = \frac{\partial}{\partial x_j}\left(\lambda \frac{\partial T}{\partial x_j}\right) + \beta T\left(\frac{\partial p}{\partial t} + \frac{\partial u_j p}{\partial x_j}\right) + \Phi \quad (3.18)$$

Equations (3.1), (3.7), (3.18) and the equation of state relating the local density to the local values of temperature and pressure, coupled with appropriate boundary conditions discussed in section 3.10, can be used to determine the velocity component u_j and fluid properties ρ, p and T in both laminar and turbulent flow. Even with the current advances in computer technology, exact solutions to turbulent flows is not possible because of

i) Lack of an explicit equation for discussing pressure

ii) Pressure and velocity are intricately coupled

iii) Presence of non-linear terms in the convective term

3.2 Turbulence Modeling

3.2.1 Reynolds Decomposition

Exact modeling of turbulent flow requires the exact solution of the Continuity and Navier-Stokes equations which can be extremely difficult and time consuming due to the many scales involved. To reduce the complexity, an approximation to the Navier-Stokes equation was developed by Osborne Reynolds (1894) called the Reynolds-averaged Navier–Stokes equations (or RANS equations). The concept entails decomposing the instantaneous fluid flow quantities in the Navier-Stokes equations into mean (time-averaged) value and fluctuating value.

Reasons why we decompose the variables are:

i) When we measure the quantities, we are usually interested in the mean values rather than the time histories.

ii) When we want to solve Navier-Stokes equations numerically, it would require a very fine grid to resolve all turbulent scales and it would also require a very fine resolution in time (turbulent flow is always unsteady since it is characterized by existence of random fluctuations in the fluid and has infinite number of scales)

Modelling of turbulence is based on the concept that fluid properties at a given point exhibit a net mean behavior with small fluctuations about it as a function of time. The instantaneous fluid property φ as a function of time t is, at a given point is shown in figure 3.1 below where an arbitrary flow property φ is shown at some location in the flow:

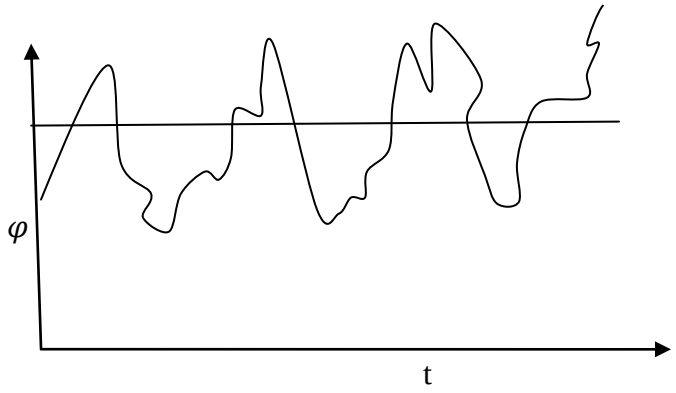

Figure 3.1 Fluid property of turbulence φ as a function of time t

The property φ could be a velocity components, pressure component, fluid temperature or any other fluid property. We define the time average variable $\bar{\varphi}$ as;

$$\bar{\varphi} \equiv \frac{1}{T_1}\int_0^{T_1} \varphi \, dt \tag{3.19}$$

where T_1 is a time large enough such that $\bar{\varphi}$ is the same for any larger time for a steady mean flow. The overbar denotes the time average of φ. The instantaneous quantity φ may be written in terms of a time average $\bar{\varphi}$ and a fluctuating quantity, as in;

$$\varphi = \bar{\varphi} + \varphi' \tag{3.20}$$

Similarly, for scalar quantities;

$$\emptyset = \overline{\emptyset} + \emptyset' \tag{3.21}$$

Where $\emptyset$ denotes a scalar such as temperature, energy, pressure or turbulent quantities.

3.2.2 Instantaneous Equations of Motion

A turbulent flow instantaneously satisfies the Navier-Stokes equations. We are generally interested in finding only the gross characteristics in such a flow, such as the distributions of mean velocity and temperature. In this section, we shall derive the equations of motion for the mean state in a turbulent flow. The method of developing these equations of motion involves, first writing the equations for the instantaneous quantities. Then we take the time average of both sides, noting that if the quantity is valid instantaneously then it is also valid on the average for some period of time. Finally we simplify the equations such that only the average quantities appear. We assume that density variations are caused by temperature fluctuations alone. Under the Boussinesq (1903) approximation, the equations of motion for the instantaneous variables are found from equations (3.1), (3.7) and (3.18) which become;

$$\frac{\partial \tilde{\rho}}{\partial t} + \frac{\partial}{\partial x_i}\left(\tilde{\rho}\tilde{u}_j\right) = 0 \tag{3.22}$$

$$\frac{\partial}{\partial t}\tilde{\rho}\tilde{u}_j + \frac{\partial}{\partial x_j}\tilde{\rho}\tilde{u}_i\tilde{u}_j = -\frac{\partial \tilde{P}}{\partial x_i} + \tilde{\rho}g_i + \frac{\partial}{\partial x_j}\left[\mu\left(\frac{\partial \tilde{u}_i}{\partial x_j} + \frac{\partial \tilde{u}_j}{\partial x_i}\right) + \mu_s\delta_{ij}\rho\frac{\partial \tilde{u}_k}{\partial x_k}\right] \quad (3.23)$$

$$\frac{\partial}{\partial t}\left(\tilde{C}_P\tilde{\rho}\tilde{T}\right) + \frac{\partial}{\partial x_j}\left(\tilde{C}_P\tilde{\rho}\tilde{U}_j\tilde{T}\right) = \frac{\partial}{\partial x_j}\left(\lambda\frac{\partial \tilde{T}}{\partial x_j}\right) + \beta T\left(\frac{\partial \tilde{p}}{\partial t} + \frac{\partial \tilde{u}_j\tilde{p}}{\partial x_j}\right) + \Phi \quad (3.24)$$

The equations satisfied by the mean flow are obtained by substituting the Reynolds decomposition to the instantaneous continuity equation (3.22), momentum equation (3.23) and energy equation and taking the average of the equations. From equation (3.22), we decompose the variable $\tilde{u}_j$ and $\tilde{\rho}$ into time average variables plus fluctuating components as given by equation (3.20). That is $\tilde{\rho} = \bar{\rho} + \rho'$, $\tilde{u}_j = \bar{u}_j + u_j'$.

3.2.3 Averaged Equations of Motion

a) Continuity equation for Turbulent flow

This equation is valid for turbulent flow, and the dependent variables ($\tilde{\rho}$ and $\tilde{u}_j$) represent instantaneous quantities. Decomposing instantaneous continuity equation into its mean and turbulent part yields;

$$\frac{\partial}{\partial t}(\bar{\rho} + \rho') + \frac{\partial}{\partial x_j}(\bar{\rho} + \rho')\left(\bar{u}_j + u_j'\right) = 0 \quad (3.25)$$

Time averaging the entire equation gives;

$$\overline{\frac{\partial}{\partial t}(\bar{\rho}+\rho')+\frac{\partial}{\partial x_j}(\bar{\rho}+\rho')(\bar{u}_j+u_j')}=\overline{\frac{\partial}{\partial t}(\bar{\rho}+\rho')}+\overline{\frac{\partial}{\partial x_j}(\bar{\rho}+\rho')(\bar{u}_j+u_j')}=0$$

Where

$$\overline{\frac{\partial}{\partial t}(\bar{\rho}+\rho')}=\frac{\partial\overline{(\bar{\rho}+\rho')}}{\partial t}=\frac{\partial\bar{\rho}}{\partial t}+\frac{\partial\overline{\rho'}}{\partial t}=\frac{\partial\bar{\rho}}{\partial t}$$

Because;

$$\frac{\partial\overline{\rho'}}{\partial t}=0$$

$$\overline{\frac{\partial}{\partial x_j}(\bar{\rho}+\rho')(\bar{u}_j+u_j')}=\overline{\frac{\partial}{\partial x_j}(\bar{\rho}\bar{u}_j+\bar{\rho}u_j'+\rho'\bar{u}_j+\rho'u_j')}$$

Taking the time average, expanding and simplifying equation (3.28), we obtain;

$$\frac{\partial}{\partial x_j}(\bar{\rho}\bar{u}_j+\bar{\rho}\overline{u'}_j+\overline{\rho'}\bar{u}_j+\overline{\rho'u_j'})=\frac{\partial}{\partial x_j}(\bar{\rho}\bar{u}_j+\overline{\rho'u_j'})\text{ since }\overline{u'}_j=\overline{\rho'}=0$$

Given that the terms which are linear in fluctuating quantities become zero when time averaged. Therefore the time averaged continuity equation becomes;

$$\frac{\partial\bar{\rho}}{\partial t}+\frac{\partial}{\partial x_j}(\bar{\rho}\bar{u}_j+\overline{\rho'u_j'})=0 \qquad (3.26)$$

b) Momentum Equation for Turbulent Flow

Decomposing the instantaneous dependent variables of the momentum equation (3.23) into their mean and fluctuating parts yields;

$$\frac{\partial}{\partial t}(\bar{\rho}+\rho')\left(\bar{u}_j+u_j'\right)+\frac{\partial}{\partial x_j}(\bar{\rho}+\rho')(\bar{u}_i+u_i')\left(\bar{u}_j+u_j'\right)$$

$$=-\frac{\partial(\bar{P}+P')}{\partial x_i}+(\bar{\rho}+\rho')g_i$$

$$+\frac{\partial}{\partial x_j}\left[\mu\left(\frac{\partial(\bar{u}_i+u_i')}{\partial x_j}+\frac{\left(\bar{u}_j+u_j'\right)}{\partial x_i}\right)+\mu_s\delta_{ij}\rho\frac{\partial(\bar{u}_k+u_k')}{\partial x_k}\right]$$

Averaging each term on both sides;

$$\overline{\frac{\partial}{\partial t}(\bar{\rho}+\rho')\left(\bar{u}_j+u_j'\right)}=\overline{\frac{\partial}{\partial x_j}\left(\bar{\rho}\bar{u}_j+\bar{\rho}\bar{u'}_j+\rho'\bar{u}_j+\rho'u_j'\right)}+\frac{\partial}{\partial t}\left(\bar{\rho}\bar{u}_j+\bar{\rho}\bar{u'}_j+\bar{\rho'}\bar{u}_j+\overline{\rho'u_j'}\right)$$

$$=\frac{\partial}{\partial t}\left(\bar{\rho}\bar{u}_j+\overline{\rho'u_j'}\right)$$

$$\overline{\frac{\partial}{\partial x_j}\left((\bar{\rho}+\rho')(\bar{u}_i+u_i')\left(\bar{u}_j+u_j'\right)\right)}=\frac{\partial}{\partial x_j}\overline{\left((\bar{\rho}+\rho')(\bar{u}_i+u_i')\left(\bar{u}_j+u_j'\right)\right)}$$

where;

$$(\bar{\rho}+\rho')(\bar{u}_i+u_i')\left(\bar{u}_j+u_j'\right)=\left(\bar{\rho}\bar{u}_j+\bar{\rho}u_j'+\rho'\bar{u}_j+\rho'u_j'\right)\left(\bar{u}_j+u_j'\right)$$

$$=\bar{\rho}\bar{u}_j\bar{u}_j+\bar{\rho}\bar{u}_ju_j'+\bar{\rho}u_j'\bar{u}_j+\bar{\rho}u_j'u_j'+\rho'\bar{u}_j\bar{u}_j+\rho'\bar{u}_ju_j'+\rho'u_j'\bar{u}_j+\rho'u_j'u_j'$$

and;

$$\overline{(\bar{\rho}+\rho')(\bar{u}_i+u_i')\left(\bar{u}_j+u_j'\right)}=\bar{\rho}\bar{u}_j\bar{u}_j+\bar{\rho}\overline{u_j'u_j'}+\bar{\rho'}\bar{u}_j\bar{u_j'}+\overline{\rho'u_j'}\bar{u}_j+\overline{\rho'u_j'u_j'}$$

so that;

$$\frac{\partial}{\partial x_j}\overline{\left((\bar{\rho}+\rho')(\bar{u}_\iota+u_\iota')\left(\bar{u}_\jmath+u_\jmath'\right)\right)} = \frac{\partial}{\partial x_j}\left(\bar{\rho}\bar{u}_j\bar{u}_j + \bar{\rho}\overline{u_j'u_j'} + \bar{\rho}'\bar{u}_j\bar{u}_j' + \overline{\rho' u_j'}\bar{u}_j + \overline{\rho' u_j' u_j'}\right)$$

$$= \frac{\partial}{\partial x_j}\left(\bar{\rho}\bar{u}_j\bar{u}_j + \bar{\rho}'\bar{u}_i\bar{u}_j\right)$$

and;

$$\overline{\frac{\partial(\bar{P}+P')}{\partial x_i}} = \frac{\partial\overline{(\bar{P}+P')}}{\partial x_i} = \frac{\partial(\bar{P}+\bar{P}')}{\partial x_i} = \frac{\partial(\bar{P})}{\partial x_i}$$

$$\overline{(\bar{\rho}+\rho')}g_i = (\bar{\rho}+\bar{\rho}')g_i = \bar{\rho}g_i$$

Therefore;

$$\overline{\frac{\partial}{\partial x_\jmath}\left[\mu\left(\frac{\partial(\bar{u}_\iota+u_\iota')}{\partial x_\jmath}+\frac{\left(\bar{u}_\jmath+u_\jmath'\right)}{\partial x_\iota}\right)+\mu_s\delta_{\iota\jmath}\rho\frac{\partial(\bar{u}_k+u_k')}{\partial x_k}\right]} = \frac{\partial}{\partial x_j}\left[\mu\left(\frac{\partial\bar{u}_i}{\partial x_j}+\frac{\partial\bar{u}_j}{\partial x_i}\right)+\mu_s\delta_{ij}\frac{\partial\bar{u}_k}{\partial x_k}\right]$$

Therefore the Reynolds form of the equation becomes;

$$\frac{\partial}{\partial t}\left(\bar{\rho}\bar{u}_j+\overline{\rho' u_j'}\right)+\frac{\partial}{\partial x_j}\left(\bar{\rho}\bar{u}_j\bar{u}_j+\bar{\rho}'\bar{u}_i\bar{u}_j\right)$$

$$= -\frac{\partial(\bar{P})}{\partial x_i}+\bar{\rho}g_i+\frac{\partial}{\partial x_j}\left(\bar{\tau}_{ij}-\bar{u}_j\overline{\rho' u_j'}-\overline{\rho u_\iota' u_j'}-\overline{\rho' u_\iota' u_j'}\right) \qquad (3.27)$$

In which;

$$\bar{\tau}_{ij} = \mu\left(\frac{\partial\bar{u}_i}{\partial x_j}+\frac{\partial\bar{u}_j}{\partial x_i}\right)+\mu_s\delta_{ij}\frac{\partial\bar{u}_k}{\partial x_k} \qquad (3.28)$$

c) Energy equation for Turbulent Flow

Similarly, the energy equation (3.24) can be decomposed using equation (3.21) and the resulting equation is time averaged and simplified by eliminating terms known to be zero to yield;

$$\frac{\partial}{\partial t}\left(C_P\bar{\rho}\bar{T} + C_P\overline{\rho'T'}\right) + \frac{\partial}{\partial x_j}\left(C_P\overline{\rho u_j}\bar{T}\right)$$

$$= \frac{\partial \bar{p}}{\partial t} + \frac{\partial \bar{p}}{\partial x_j} + \overline{u'_\iota \frac{\partial p'}{\partial x_j}} + \frac{\partial}{\partial x_j}\left(\lambda\frac{\partial \bar{T}}{\partial x_j} - C_P\bar{\rho}\overline{u'_\iota T'} - C_P\overline{\rho' u_\iota T'}\right) + \bar{\Phi} \qquad (3.29)$$

Where;

$$\bar{\Phi} = \overline{\tau_{\iota J}}\frac{\partial \bar{u}_\iota}{\partial x_j} + \overline{\tau'_{\iota J}\frac{\partial u'_\iota}{\partial x_j}} \qquad (3.30)$$

The τ_{ij} in the equation (3.30) should be evaluated as expressed in equation (3.28).

The mean continuity and momentum equations adds unknown quantities which represent the mean effect of turbulence. These terms enter the governing equations as turbulent transport terms, such as $\overline{\rho' u_\iota' u_j'}$ and density generated terms as $\overline{\rho' u_j'}$ and $\overline{\rho' u_\iota'}$. In the mean energy equation, the time averaging process introduces unknown turbulent correlation between temperature fluctuation $\overline{u_\iota' T'}$ or $\overline{u_j' T'}$, which, when multiplied by density ρ, they represent transport of heat or mass due to fluctuation motion. The term -$\rho\overline{u_\iota' T'}$ is the transport in the direction x_i or rather the turbulent heat flux. Mass weighted averages eliminate the mean mass term $\overline{\rho' u_j'}$ and some momentum transport terms such as $\rho\overline{u'_\iota u'_J}$ across mean streamline (Cebeci and Smith, 1974).

Equations (3.26), (3.27) and (3.29) are equations generally accepted as governing the mean flow quantities $\bar{u}_i$ and fluid properties $\bar{\rho}$, $\bar{p}$ and temperature $\bar{T}$. The different levels of approximations involved when closing the equation system in equations (3.26), (3.27) and (3.29) listed in increasing order of complexity, ability to model the turbulence, and cost in terms of computational work are:

i) Algebraic models
ii) One equation models
iii) Two-equation models
iv) Reynolds stress models

3.3 Reynolds Stress Equations

Let us refer to the time averaged continuity equation (3.26) and Navier-Stokes equation (3.27), in which upper and lower case of letters would be used to refer to mean and fluctuating quantities for the case of velocity components, written in Cartesian tensor below;

$$\mu \frac{\partial \rho}{\partial t} + (\rho \bar{U}_i)_{,i} = 0 \tag{3.31}$$

$$\frac{\partial \rho \bar{U}_i}{\partial t} + (\rho \bar{U}_i \bar{U}_j)_{,j} = -\bar{P}_{,i} + \left[\mu(\bar{U}_{i,j} + \bar{U}_{j,i}) - \rho \overline{u_i u_j}\right]_{,j} \tag{3.32}$$

3.3.1 Algebraic models

An algebraic equation is used to compute turbulent viscosity, often called eddy viscosity. Reynolds stress tensor is then computed using an assumption (i.e. the Boussinesq assumption) which relates the Reynolds stress tensor to the velocity gradients and turbulent viscosity. Models which are based on a turbulent (eddy) viscosity are called eddy viscosity models (EVM).

3.3.2 Boussinesq Assumption

In eddy viscosity turbulence models, the Reynolds stresses are linked to the velocity gradients via the turbulent viscosity (i.e. The eddy viscosity concept presumes an analogy between the molecular motions, which leads to Stoke's viscosity law in laminar flow, and instantaneous turbulent motion). This relation is called the Boussinesq assumption, where the Reynolds stress tensor in the time averaged Navier-Stokes equation (3.32) is replaced by the turbulent viscosity multiplied by the velocity gradients.

To show this, this assumption is introduced for the diffusion term at the right –hand side of Equation (3.32) and make an identification;

$$\left[\mu(\overline{U}_{i,j} + \overline{U}_{j,i}) - \rho\overline{u_i u_j}\right]_{,j} = \left[(\mu + \mu_t)\left(\overline{U}_{i,j} + \overline{U}_{j,i}\right)\right]_{,j} \tag{3.33}$$

Equation (3.33) on expansion and re-arrangement gives;

$$\rho\overline{u_i u_j} = -\mu_t\left(\overline{U}_{i,j} + \overline{U}_{j,i}\right) \tag{3.34}$$

If we do a contraction in equation (3.34) (i.e. setting $i = j$) the right –hand side gives;

$$\overline{u_i u_j} \equiv 2k \tag{3.35}$$

Where k is the turbulent kinetic energy. On the other hand, using the continuity equation (3.31), the right-hand side of equation. (3.34) simplifies to zero.

3.3.3 The Eddy Viscosity Concept – The closure Problem

In order to make equation (3.34) valid upon contraction, we add $2/3\,\delta_{ij}\rho k$ to the right-hand side of equation (3.34) so that;

$$\rho\overline{u_i u_j} = -\mu_t\left(\overline{U}_{i,j} + \overline{U}_{j,i}\right) + \frac{2}{3}\delta_{ij}\rho k \tag{3.36}$$

Note that the contraction of δ_{ij} gives;

$$\delta_{ii} = \delta_{11} + \delta_{22} + \delta_{33} \tag{3.37}$$

Equation (3.36) can likewise be written as;

$$\tau_{ij} = -\overline{\rho u_i' u_i'} = \mu_t\left(\frac{\partial\overline{u_i}}{\partial x_j} + \frac{\partial\overline{u_i}}{\partial x_i}\right) + \frac{2}{3}\bar{\rho}k\delta_{ij} \tag{3.38}$$

Where:

- μ_t is the turbulent or eddy viscosity, the proportionality parameter that links the turbulent stresses and the mean flow velocity gradient (or the mean strain rate). Like molecular viscosity, its unit is Pascal seconds.
- Turbulent viscosity is not homogeneous, i.e. it varies in space. It is however assumed to be isotropic i.e. it is the same in all directions.
- k is the turbulent kinetic energy (or the kinetic energy of the turbulent velocity fluctuation) given by;

$$k = \frac{1}{2}\overline{u_i' u_i'} \tag{3.39}$$

This method was first postulated by Boussinesq (1903) and consequently denoted the Boussinesg hypothesis.

Further;

$$-\overline{\rho u_j' T'} = \frac{k_t}{C_p}\frac{\partial T}{\partial x_i} \tag{3.40}$$

k_t is the turbulent conduction coefficient. In contrast to molecular viscosity μ and thermal conductivity of the fluid λ in laminar flow, μ_t and k_t are not fluid properties but flow properties. The problem at the moment is to device means of solving the turbulent stress, τ_{ij} and the turbulent heat $\overline{\rho u_j' T'}$. In this study, a two-equation model, $\kappa - \omega$ SST model, is used to solve this problem. This is actually one of the most commonly used turbulence model. In this model, the idea is to express turbulence viscosity as a function of κ and ω and then derive PDEs for κ and ω. Relationships for eddy viscosity μ_t and turbulent specific dissipation ω are required for closure.

The square root of the turbulent kinetic energy $\kappa^{\frac{1}{2}}$ can be used to represent a velocity scale for the large scale turbulent motion. Accordingly, the eddy viscosity is considered proportional to a velocity characterizing the fluctuating motion and to a typical length of this motion which Prandtl (1945) called; mixing length. Using this equation, an eddy viscosity relation yields;

$$\mu_t \propto \kappa^{\frac{1}{2}} l \tag{3.41}$$

$$\mu_t = C_\mu \kappa^{\frac{1}{2}} l \tag{3.42}$$

Where l the turbulent length is is scale and C_μ is a constant which has to be determined empirically. From the definition of turbulent length scale;

$$l = \frac{\kappa^{\frac{3}{2}}}{\varepsilon} \tag{3.43}$$

Hence

$$\mu_t = C_\mu \kappa^{\frac{1}{2}} l = C_\mu \kappa^{\frac{1}{2}} \frac{\kappa^{\frac{3}{2}}}{\varepsilon} = C_\mu \frac{\kappa^2}{\varepsilon} \tag{3.44}$$

where ε is turbulent dissipation.

The turbulent variable ω was defined by Wilcox (1998) as;

$$\omega = \frac{\varepsilon}{C_\mu \kappa} \tag{3.45}$$

Hence from equation (3.45) above, $\varepsilon = C_\mu \kappa \omega$.

The eddy viscosity for the formulation, Wilcox (1998), using equation (3.44) where $\mu_t = C_\mu \frac{\kappa^2}{\varepsilon}$ is;

$$\mu_t = \frac{\kappa}{\omega} \tag{3.46}$$

and

$$\kappa_t = \frac{\mu_t C_p}{P_r} \tag{3.47}$$

The model includes two transport equations to represent the turbulent properties of the flow. The first transport variable is the turbulent kinetic energy κ. The second transport variable is the specific dissipation ω. It is the variable that determines the length scale of turbulence.

3.3.4 The Exact Kinetic Energy Equation

The equation for turbulent kinetic energy $k = \frac{1}{2}\overline{u_i' u_i'}$ is derived from the Navier-Stokes equation, assuming steady, incompressible constant viscosity, reads;

$$(\rho U_i U_j)_{,j} = -P_{,i} + \mu U_{i,jj.} \tag{3.48}$$

Where $,j$ denotes derivation with respect to x_j.

The time averaged Navier-Stokes equation is;

$$(\rho \bar{U}_i \bar{U}_j)_{,j} = -\bar{P}_{,i} + \mu \bar{U}_{i,jj} - (\rho \overline{u_i u_j})_{,j} \tag{3.49}$$

Subtracting equation (3.49) from equation (3.48), multiplying by u_i and time averaging resultant equation yields;

$$\overline{[\rho U_\iota U_J - \rho\overline{U}_\iota\overline{U}_J]_{,J}u_\iota} = -\overline{[P-\bar{P}]_{,\iota}u_\iota} + \mu\overline{[U_\iota - \overline{U_\iota}]_{,JJ}u_\iota} + \rho\overline{\bar{u}_\iota\bar{u}_J]_{,J}u_\iota} \tag{3.50}$$

The left hand-side can be written as;

$$\overline{\rho[(\overline{U}_\iota + u_\iota)(\overline{U}_J + u_J) - \overline{U}_\iota\overline{U}_J]_{,J}u_\iota} = \overline{\rho[\overline{U}_\iota u_J + u_\iota\overline{U}_J + u_\iota u_J]_{,J}u_\iota} \tag{3.51}$$

Using the continuity equation,$(\rho u_j)_{,j} = 0$, the first term is re-written as;

$$\overline{\rho(\overline{U}_\iota u_J)_{,J}u_\iota} = \rho\overline{u_\iota u_J}\overline{U}_{i,j} \tag{3.52}$$

We obtain the second term $(\rho\overline{U}_j)_{,j} = 0$ from;

$$\overline{(\rho\overline{U}_J k)_{,j}} = \overline{U}_j\overline{\rho[\tfrac{1}{2}u_\iota u_J]_{,j}} = \tfrac{1}{2}\rho\overline{U}_j\overline{\{u_\iota u_{\iota,J} + u_\iota u_{\iota,J}\}_{,J}u_\iota} = \overline{u_\iota(\rho\overline{U}_\iota u_J)_{,J}} \tag{3.53}$$

Using the same technique as in equation (3.53) where $\overline{[\frac{1}{2}u_\iota u_J]_{,j}} = \frac{1}{2}\overline{\{u_\iota u_{\iota,J} + u_\iota u_{\iota,J}\}_{,J}u_\iota}$, the third term in equation (3.51) can be written as;

$$\tfrac{1}{2}\overline{(\rho u_J u_\iota u_\iota)_{,j}} \tag{3.54}$$

The first term of equation (3.51) on the right hand side has the form;

$$-\overline{P_{,i}u_i} = -(\overline{Pu_i})_{,j} \tag{3.55}$$

The second term on the right-hand side of equation (3.51) read;

$$\mu\overline{U_{i,JJ}u_i} = \mu\{\overline{(u_{i,J}u_i)_{,J} - u_{i,J}u_{i,J}}\} \tag{3.56}$$

Using the approach as in equation (3.53), where $\overline{[\frac{1}{2}u_iu_j]}_{,j} = \frac{1}{2}\overline{\{u_iu_{i,J} + u_iu_{i,J}\}_{,J}u_i}$ the first term becomes;

$$\mu\overline{(u_{i,J}u_i)_{,J}} = \mu\frac{1}{2}\overline{(u_iu_i)_{JJ}} = \mu k_{jj} \tag{3.57}$$

The last term on the right-hand side of equation (3.50) is zero.

Now we can assemble the transport equation for the turbulent kinetic energy. Equations (3.52), (3.53), (3.55), (3.56), (3.57) give;

$$\underbrace{(\rho\bar{U}_jk)_{,j}}_{\text{I}} = \underbrace{-\rho\overline{u_iu_J}\bar{U}_{i,j}}_{\text{II}} \underbrace{-[\overline{u_JP} + \frac{1}{2}\overline{\rho u_ju_iu_i} - \mu k_j]_{,j}}_{\text{III}} \underbrace{-\mu\overline{(u_{i,J}u_i)_{,J}}}_{\text{IV}} \tag{3.58}$$

The terms in equation (3.58) have the following meaning.

I. Convection: The rate of change of kinetic energy of turbulence i.e. the kinetic energy of the fluctuation motion that is convected by the mean motion.

II. Production: The large turbulent scales extract energy from the mean flow.

III. The first two terms represent turbulent diffusion by pressure-velocity fluctuations, and velocity fluctuations respectively. The last term is viscous diffusion.

IV. Dissipation: This term is responsible for transformation of kinetic energy at small scales to internal energy.

3.3.5 The Modeled k-Equation

In the exact kinetic energy equation (3.58), a number of terms are not known, namely the production term, the turbulent diffusion term and the dissipation term.

i) In the production term of equation (3.58), it is the stress tensor which is unknown. Since an expression for this is used in the Navier-Stokes equation, the same expression is used in the production term. equation (3.38) inserted in the production term (term II) in equation (3.58) gives;

$$P_k = -\rho\overline{u_i u_j}\overline{U}_{i,j} = \mu_t\left(\overline{U}_{i,j} + \overline{U}_{j,i}\right)\overline{U}_{i,j} + \frac{2}{3}\delta_{ij}\rho k\overline{U}_{i,i} \tag{3.59}$$

The last term in equation (3.59) is zero for incompressible flow due to continuity as per equation (3.31) above.

ii) The triple correlations in term III in equation (3.58) is modeled using a gradient law where we assume that k is diffused down the gradient, i.e. from region of high k to

regions of small k (cf. Fourier's law for heat flux: heat is diffused from hot to cold regions), which yields;

$$\frac{1}{2}\overline{\rho u_j u_i u_i} = \frac{\mu_t}{\sigma_k} k_{,j} \tag{3.60}$$

Where σ_k is the turbulent Prandtl number. There is no model for the pressure diffusion term in equation (3.58). It is small and therefore simply neglected.

iii) The dissipation term in equation (3.58) is basically estimated as in the equation;

$$\varepsilon = O\frac{u^2}{l/u} = O\frac{u^3}{l} \tag{3.61}$$

where O is the order of the function.

Which is a relation for the cascade process i.e. the energy dissipated at the small scales can be estimated using the large scales u (the velocity scale) and l(the boundary layer thickness or the order of the flow geometry) and $\varepsilon = (m^2/s^3)$ is the energy per unit time per unit mass [dissipation which is the rate at which kinetic energy is dissipated (transformed) into internal energy at the smallest scales since the frictional forces (viscous stresses) become too large].

Therefore, as per equation (3.61), the velocity scale is now;

$$u = \sqrt{k} \tag{3.62}$$

Therefore;

$$\varepsilon = \nu\overline{u_{\iota,j}u_{\iota,j}} = \frac{k^{\frac{3}{2}}}{l}\nu = \frac{\mu}{\rho} \tag{3.63}$$

Where $\nu = \frac{\mu}{\rho}$.

Hence;

$$\mu\overline{u_{\iota,j}u_{\iota,j}} = \rho\varepsilon = \rho\frac{k^{\frac{3}{2}}}{l} \tag{3.64}$$

The modeled k equation can now be assembled to give;

$$(\rho\overline{U}_j k)_{,j} = (\mu + \frac{\mu_t}{\sigma_k})k_{,j} + P_k - \rho\frac{k^{\frac{3}{2}}}{l} \tag{3.65}$$

An additional transport equation is required to compute l. In the $\kappa - \omega$ model, the length determining equation ω is used. This quantity is often called specific dissipation from its definition which is;

$$\omega = \frac{\varepsilon}{\kappa} \tag{3.66}$$

The modeled κ and ω equations are respectively;

$$(\rho U_j k)_{,j} = [(\mu + \frac{\mu_t}{\sigma_k})k_{,j}]_{,j} + P_k - \beta^*\omega k \tag{3.67}$$

$$(\rho\overline{U}_j\omega)_{,j} = [(\mu + \frac{\mu_t}{\sigma_\omega})\omega_{,j}]_{,j} + \frac{\omega}{k}(C_{w1}P_k - C_{w2}\rho k\omega) \tag{3.68}$$

Where;

$$\mu_t = \rho\frac{\kappa}{\omega} \tag{3.69}$$

$$\varepsilon = \beta^*\omega k \tag{3.70}$$

The constants are determined from experiments.

The wall boundary condition for the turbulent kinetic energy is $k_{\text{wall}} = 0$. Since the turbulent kinetic energy is zero at the wall, then the eddy viscosity is also zero at the wall. Hence from the definition of the specific dissipationω, ($\omega = \frac{\varepsilon}{C_\mu\kappa}$), it implies that ω should go to infinity at the wall since k tends to zero. Basing on asymptotic arguments, Wilcox (1998) suggested that it be given the value $\omega_{\text{wall}} = \frac{60\nu}{C_\mu(\Delta y^2)}$ at the wall where Δy is the normal distance to the first point off the wall. Free stream boundary conditions;

$$\frac{V_{t\infty}}{V_\infty} = 0.0001, \qquad \omega_\infty = 10\frac{U_\infty}{l} \qquad k_\infty = V_\infty\omega_\infty \tag{3.71}$$

3.4 Final Set of Equations

For simplicity, from this point onwards, the over-bar indicating time mean values of the variables and the prime indicating the fluctuating quantities will be replaced by the upper and lower case letters respectively. The final set of equations for turbulent natural convection flows is:

$$\frac{\partial \rho}{\partial t} + \frac{\partial}{\partial x_j}\left(\rho U_j + \overline{\rho u_\iota}\right) = 0 \tag{3.72}$$

$$\frac{\partial}{\partial t}\left(\rho U_i + \overline{\rho u_\iota}\right) + \frac{\partial}{\partial x_j}\left(\rho U_i U_j + U_i \overline{\rho u_\iota}\right)$$

$$= -\frac{\partial P}{\partial x_i} + p g_i + \frac{\partial}{\partial x_j}\left(\tau_{ij} - U_i \overline{\rho u_\iota} - \rho \overline{u_\iota u_j} - \overline{\rho u_\iota u_j}\right) \tag{3.73}$$

$$\frac{\partial}{\partial t}\left(C_P \rho T + C_P \overline{\rho T}\right) + \frac{\partial}{\partial x_j}\left(C_P \overline{\rho U_J T}\right)$$

$$= \frac{\partial p}{\partial t} + U_j \frac{\partial p}{\partial x_j} + \overline{u_J \frac{\partial p}{\partial x_J}} + \frac{\partial}{\partial x_j}\left(\lambda \frac{\partial T}{\partial x_j} - C_P \overline{u_t T} - C_P \overline{u_\iota T}\right) + \Phi \tag{3.74}$$

Where;

$$\tau_{ij} = \mu\left(\frac{\partial U_i}{\partial x_j} + \frac{\partial U_i}{\partial x_i}\right) + \mu_s \delta_{ij} \frac{\partial u_k}{\partial x_k} \tag{3.75}$$

$$\Phi = \tau_{ij} + \frac{\partial U_i}{\partial x_j} + \overline{\mu\left(\frac{\partial u_\iota}{\partial x_J} + \frac{\partial u_J}{\partial x_\iota}\right)\frac{\partial u_\iota}{\partial x_J}} \tag{3.75}$$

$$\frac{\partial}{\partial t}\rho k + \frac{\partial}{\partial x_j}\left(\rho U_i k\right)$$

$$= \overline{u_J \frac{\partial}{\partial x_J}\mu \frac{\partial u_\iota}{\partial x_J} + \frac{\partial u_J}{\partial x_\iota}} - \frac{1}{2}\frac{\partial}{\partial x_j}\overline{\rho u_\iota u_\iota u_J} - \rho \overline{u_\iota u_J}\frac{\partial u_i}{\partial x_j} + \overline{\rho u_\iota} g_i - \overline{u_J \frac{\partial p}{\partial x_\iota}} \tag{3.76}$$

$$\frac{\partial \omega}{\partial t} + U_i \frac{\partial \omega}{\partial x_j} = -\frac{\partial}{\partial x_i}\left[\left((\mu + \frac{\mu_t}{\sigma_\omega}\right)\frac{\partial \omega}{\partial x_j}\right] + \left[\beta - \frac{k^2}{\sigma_\omega \sqrt{c_u}}\right]\frac{\omega}{k} P_k - \beta \omega^2 \tag{3.77}$$

3.5 Non-Dimensionalisation

This implies the partial or full removal of units from an equation involving physical quantities by a suitable substitution of variables. This technique can simplify and parametize problems where measured units are involved. In fluid mechanics, the adoption of a suitable non-dimensional scheme is important, Jiyuan *et al.* (2012). An appropriate scheme does the following:-

i) It expresses experimental and analytic results in the most efficient form

ii) Makes the solution bounded for instance, temperature can be non-dimensionalized such that it varies from 0 to 1.

The non-dimensional form of the governing equations (and boundary conditions) can be achieved by dividing all the dependent and independent flow variables by relevant and meaningful constant quantities. For lengths the variable can be divided by a characteristic length L_o (which is the width of the enclosure), all velocities by a reference velocity U_*(which is the inlet velocity), pressure by $P_o = \rho U_*^2$ (which is twice the dynamic pressure for the channel) and temperature by a suitable temperature difference (which is $\{T - T_*\}/\Delta T_*$ for the enclosure). The mean variables and their corresponding fluctuating quantities have the scaling variables and so non-dimensionalization is based on the following set of general scaling variables;

$$\begin{aligned} &X_j = X_j' \qquad U_j = U_j' U_* \qquad P = P' P_o \qquad \Theta = \frac{T - T_*}{\Delta T_*} \\ &K = K' U_* \qquad \varepsilon = \varepsilon' \frac{U_*^3}{L_0} \qquad t = t' \frac{L_0}{U_*} \qquad \mu = \mu' \mu_0 \\ &\mu_s = \mu_s' \mu_0 \qquad V = V' \mu_0 \rho = \rho' \rho_0 = C_R C_{PP} \qquad \lambda = \lambda' \lambda_0 \end{aligned} \tag{3.78}$$

In which L_0 is the characterized length, ΔT_* is the characterized temperature difference and T_* is a convenient temperature that will result in Θ being bounded in the solution region. The prime denotes a no-dimensional quantities and the subscript $*$ denotes a variable that can be arbitrarily defined to specify a non-dimensional scheme. The main rationale behind non-dimensionalisation is to reduce the number of parameters, (Jiyuan *et al.*, 2012). To apply these variables in the continuity equation (3.72) gives the following equation;

$$\frac{\partial \rho}{\partial t} = \frac{\partial \rho}{\partial \rho'}\frac{\partial \rho'}{\partial t'}\frac{\partial t'}{\partial t} = \frac{P_o U_*}{L_0}\frac{\partial \rho'}{\partial t'},$$

$$\frac{\partial U_j}{\partial x_j} = \frac{\partial U_j}{\partial U_{j'}}\frac{\partial U_{j'}}{\partial x_j'}\frac{\partial x_j'}{\partial x_j} = \frac{U_* \partial U_{j'}}{L_o \partial x_j'}$$

$$\rho\frac{\partial U_j}{\partial x_j} = \frac{U_{*\rho'\rho_o}}{L_o}\frac{\partial U_{j'}}{\partial x_j'}$$

$$\frac{\partial \rho}{\partial x_j} = \frac{\partial \rho}{\partial \rho'}\frac{\partial \rho'}{\partial x_j'}\frac{\partial x_j'}{\partial x_j} = \frac{\rho_o}{L_o}\frac{\partial \rho'}{\partial x_j'}$$

$$U_j\frac{\partial \rho}{\partial x_j} = \frac{\rho_o U_j' U_*}{L_o}\frac{\partial \rho'}{\partial x_j'}$$

But;

$$\frac{\partial(\rho U_j)}{\partial x_j} = \rho \frac{\partial U_j}{\partial x_j} + U_j \frac{\partial \rho}{\partial x_j}$$

Therefore;

$$\frac{\partial(\rho U_j)}{\partial x_j} = \frac{U_{*\rho'\rho_o}}{L_o}\frac{\partial U_{j'}}{\partial x_j'} + \frac{\rho_o U_j' U_*}{L_o}\frac{\partial \rho'}{\partial x_j'} = \frac{\rho_o U_*}{L_o}\left(\rho' \frac{\partial U_{j'}}{\partial x_j'} + U_j' \frac{\partial \rho'}{\partial x_j'}\right) = \frac{\rho_o U_*}{L_o}\frac{\partial(\rho' U_j'')}{\partial x_j'}$$

Similarly;

$$\frac{\partial(\overline{\rho u_j})}{\partial x_j} = \frac{\overline{\partial(\rho u_j)}}{\partial x_j}$$

But;

$$\frac{\partial(\rho u_j)}{\partial x_j} = \frac{\rho_o U_*}{L_o}\frac{\partial(\rho' u_j')}{\partial x_j'}$$

Therefore;

$$\frac{\partial(\overline{\rho u_j})}{\partial x_j} = \frac{\rho_o U_*}{L_o}\frac{\partial(\overline{\rho' u_j'})}{\partial x_j'}$$

Adding all the non-dimensional form for continuity equation yields;

$$\frac{P_o U_*}{L_0}\frac{\partial \rho'}{\partial t'} + \frac{\rho_o U_*}{L_o}\frac{\partial(\rho' U_j')}{\partial x_j'} + \frac{\rho_o U_*}{L_o}\frac{\partial(\overline{\rho' u_j'})}{\partial x_j'} = 0$$

This simplifies to;

$$\frac{P_o U_*}{L_0}\frac{\partial \rho'}{\partial t'} + \frac{\rho_o U_*}{L_o}\frac{\partial}{\partial x_j'}\left(\rho' U_j' + \overline{\rho' u_j'}\right) = 0$$

Dividing through by $\frac{P_o U_*}{L_0}$ yields;

$$\frac{\partial \rho'}{\partial t'} + \frac{\partial}{\partial x_j'}\left(\rho' U_j' + \overline{\rho' u_j'}\right) = 0 \tag{3.78}$$

The same procedure is applied to the mean momentum equation (3.73), the mean energy equation (3.74), the turbulent kinetic equation (3.76) and the specific dissipation equation (3.77) yielding the following equations respectively;

$$\frac{\partial}{\partial t}(\rho' U_i' + \overline{\rho' u_i'}) + \frac{\partial}{\partial x_j}\left(\rho' U_i' U_j' + U_i' \overline{\rho' u_i'}\right)$$

$$= -\left\{\frac{P_o}{P_o U_*^2}\right\}\frac{\partial P'}{\partial x_i'} + \left\{\frac{g L_o}{U_*^2}\right\}\rho g_i'$$

$$+ \frac{\partial}{\partial x_j}\left(\left\{\frac{\mu_o}{P_o U_* L_o}\right\}\tau_{ij} - U_j' \overline{\rho' u_i'} - \rho' \overline{u_i' u_j'} - \overline{\rho' u_i' u_j'}\right) \tag{3.79}$$

$$\frac{\partial}{\partial t'}(c_P' \rho' \Theta + c_P' \overline{\rho' \theta}) + \frac{\partial}{\partial x_j'}\left(c_P \overline{\rho' U_j' \Theta}\right)$$

$$= \left\{\frac{P_o}{c_{Po} \rho_o \Delta T_*}\right\}\left[\frac{\partial P'}{\partial t'} + U_j' \frac{\partial P'}{\partial x_j'} + \overline{u_j' \frac{\partial p'}{\partial x_j}}\right]$$

$$+ \frac{\partial}{\partial x_j'}\left(\left\{\frac{\lambda_o}{c_{Po} \rho_o U_* L_o}\right\}\lambda \frac{\partial \Theta}{\partial x_j'} - c_P \rho' \overline{U_j' \theta} - c_P \overline{\rho' U_j' \theta}\right) + \left\{\frac{\mu_o U_*}{c_{Po} \rho_o \Delta T_* L_o}\right\}\emptyset \tag{3.80}$$

$$\frac{\partial}{\partial t'}\rho' k' + \frac{\partial}{\partial x_j}\rho' U_j' k'$$

$$= \left\{\frac{\mu_o}{\rho_o U_* L_o}\right\}\overline{u_j' \frac{\partial}{\partial x_j'} u_j' \left(\frac{\partial u_i'}{\partial x_j'} + \frac{\partial u_j'}{\partial x_i'}\right)} - \rho'\overline{u_i' u_j'}\frac{\partial U_i'}{\partial x_j'} - \frac{1}{2}\frac{\partial}{\partial x_j}\overline{\rho' u_i' u_j'} + \left\{\frac{gL_o}{U_*^2}\right\}p' U_i'$$

$$- \left\{\frac{P_o}{P_o U_*^2}\right\}\overline{u_j' \frac{\partial P'}{\partial x_j'}} \tag{3.81}$$

$$\frac{\partial}{\partial t'}\rho'\omega' + \frac{\partial}{\partial x_j}P' U_j'\omega'$$

$$= -\left\{\frac{\mu_o}{\rho_o U_* L_o}\right\}\frac{\partial}{\partial x_k'}\overline{(\mu'\mu_k' \frac{\partial u_i'}{\partial x_j'}\frac{\partial u_j'}{\partial x_j'}} + 2\left\{\frac{P_o}{P_o U_*^2}\right\}\nu'\overline{\frac{\partial u_k'}{\partial x_i'}\frac{\partial P'}{\partial x_i'} - \mu'\frac{\partial \varepsilon'}{\partial x_k'}}) - 2\left\{\frac{\mu_o}{\rho_o U_* L_o}\right\}\mu'\overline{\frac{\partial u_j'}{\partial x_k'}\frac{\partial u_i'}{\partial x_j'}\frac{\partial u_k}{\partial x_j'}}$$

$$- 2\left\{\frac{\mu_o^2}{P_o^2 U_*^2 L_o^2}\right\}\overline{P'}\left(\upsilon'\frac{\partial^2 u_i}{\partial x_k' \partial x_j'}\right) + 2\left\{\frac{\mu_o}{\rho_o U_* L_o}\right\}\mu'\frac{\partial u_j'}{\partial x_k'}\left(\overline{\frac{\partial u_i'}{\partial x_j'}\frac{\partial u_k'}{\partial x_j'}} + \overline{\frac{\partial u_i'}{\partial x_i'}\frac{\partial u_j'}{\partial x_k'}}\right)$$

$$- 2\left\{\frac{\mu_o}{\rho_o U_* L_o}\right\}\mu'\frac{\partial^2 u_i'}{\partial x_j' \partial x_k'}\overline{\mu_k'\frac{\partial u_i'}{\partial x_j'}} \tag{3.82}$$

From this point, all equations and variables referred will be non-dimensional. To avoid ambiguity, the primes that indicate non-dimensionality have been avoided for the remainder of this work. Using a non-dimensional scheme presented above, equations (3.78), (3.79), (3.80), (3.81) and (3.82) in general form become;

$$\frac{\partial \rho}{\partial t} + \frac{\partial}{\partial x_j}\left(\rho U_i + \overline{\rho u_j}\right) \tag{3.83}$$

$$\frac{\partial}{\partial t}(\rho U_i + \overline{\rho u_\iota}) + \frac{\partial}{\partial x_j}\left(\rho U_i U_j + U_i \overline{\rho u_J}\right)$$

$$= -N_1 \frac{\partial P}{\partial x_i} + N_2 p g_i + \frac{\partial}{\partial x_j}\left(N_3 \tau_{ij} - U_i \overline{\rho u_\iota} - \rho \overline{u_\iota u_J} - \overline{\rho u_\iota u_J}\right) = 0 \qquad (3.84)$$

$$\frac{\partial}{\partial t}(c_P \rho \Theta + c_P \overline{\rho \Theta}) + \frac{\partial}{\partial x_j}\left(c_P \overline{\rho U_J \Theta}\right)$$

$$= L_1 \left[\frac{\partial p}{\partial t} + U_j \frac{\partial p}{\partial x_j} + \overline{u_J \frac{\partial p}{\partial x_J}}\right] + \frac{\partial}{\partial x_j}\left(L_2 \lambda \frac{\partial \Theta}{\partial x_j} - c_P \overline{\rho \Theta} + c_P \rho \Theta\right)$$

$$+ L_3 \emptyset \qquad (3.85)$$

$$\frac{\partial}{\partial t}\rho k + \frac{\partial}{\partial x_j}(\rho U_i k) = A_1 \overline{u_J \frac{\partial \mu}{\partial x_J}}\left(\frac{\partial u_i}{\partial x_j} + \frac{\partial u_j}{\partial x_i}\right) - \frac{1}{2}\frac{\partial}{\partial x_j}\overline{\rho u_\iota u_J}\frac{\partial U_i}{\partial U_j} + B_2 \overline{\rho u_\iota} g_i - B_3 \overline{u_J \frac{\partial p}{\partial x_\iota}} \qquad (3.86)$$

$$\frac{\partial}{\partial t}\rho \omega + \frac{\partial}{\partial x_j}\left(\rho U_j \omega\right)$$

$$= -\frac{\partial}{\partial x_k}\left(B_1 \overline{\mu u_k \frac{\partial u_\iota}{\partial x_J}\frac{\partial u_\iota}{\partial x_J}} + 2B_2 \nu \frac{\partial u_k}{\partial x_i}\frac{\partial u_\rho}{\partial x_i} - B_1 \mu \frac{\partial \omega}{\partial x_k}\right)$$

$$- 2B_1 \mu \frac{\partial U_i}{\partial x_j}\left(\frac{\partial u_i}{\partial x_j}\frac{\partial u_k}{\partial x_j} + \frac{\partial u_j}{\partial x_j}\frac{\partial u_j}{\partial x_k}\right) - 2B_1 \mu \frac{\partial^2 U_i}{\partial x_j \partial x_k}\overline{\mu_k \frac{\partial u_\iota}{\partial x_J}} \qquad (3.87)$$

Where the coefficients;

N_1, N_2, N_3, L_1, L_2, L_3 , A_1, A_2, A_3, B_1, B_2, B_3 and B_4 are indicated in table 3.1 below.

Symbol	Coefficient	Scheme
U_*		$\sqrt{g\beta\Delta T L_o}$

N_1	$-\frac{P_o}{P_o U_*^2}$	$\frac{EU_*F_o}{\zeta\eta}$
N_2	$\frac{gL_o}{U_*^2}$	$\frac{1}{\zeta\eta}$
N_3	$\frac{\mu_o}{P_o U_* L_o}$	$\frac{1}{\sqrt{G_o}}$
L_1	$\frac{P_o}{c_{Po}\rho_o \Delta T_*}$	$E_\mu E_C$
L_2	$\frac{\lambda_o}{c_{Po}\rho_o U_* L_o}$	$\frac{1}{P_r\sqrt{G_o}}$
L_3	$\frac{\mu_o U_*}{c_{Po}\rho_o \Delta T_* L_o}$	$E_c R_e^{-1}$
A_1	$\frac{\mu_o}{\rho_o U_* L_o}$	$\frac{1}{\sqrt{G_o}}$
A_2	$\frac{gL_o}{U_*^2}$	$\frac{1}{\zeta\eta}$
A_3	$\frac{p_o}{\rho_o U_*^2}$	$\frac{E_\mu F_o}{\zeta\eta}$
B_1	$\frac{\mu_o}{\rho_o U_* L_o}$	$\frac{1}{\sqrt{G_o}}$
B_2	$\frac{\mu_o P_o}{U_*^2 L_o U_*^2}$	$\frac{E_\mu}{\sqrt{G_o}}$
B_3	$(\frac{\mu_o}{P_o U_* L_o})^2$	$\frac{1}{\sqrt{G_o}}$
B_4	$\frac{g\mu_o}{P_o U_*^3}$	$\frac{F_o}{\sqrt{G_o}}$

Table 3.1 Coefficients for Non-dimensional Governing Equations (3.84) – (3.87)

By grouping the non-dimensional parameters, originally eight, the non-dimensionalized problem will now involve only just three parameters (Re, Ra and Pr) hence a significant reduction. However In the chapter four, we describe the model, give the assumptions made and use them to simplify the governing equations, formulate the model and give the PISO and SIMPLEC boundary conditions.

3.6 Model Description

In this thesis, a numerical investigation of turbulent natural convection within a 3-D is conducted. The geometry is illustrated in figure 3.1. It consists of a hot surface, located on the left side of the rectangular cavity wall, and a cold surface on the right side. The enclosure is heated on the hot wall (Red color) and cooled on the cold wall (blue color).

The measurement of Ampofo and Karyiannis (2003) were used. The reason being that experiments by Ampofo and Karayianinis were conducted under very high accuracy and as such the results form experimental benchmark data that will be used to validate this computational fluid dynamics code. Therefore walls measures 0.75m by 0.75m wide by 1.5m. The hot and cold walls of the cavity were isothermal at 323 ± 0.15K and 283 ± 0.15K respectively, giving a Reyleigh number of 1.58×10^9. Each of the remaining walls are adiabatic.

All boundaries of the enclosure are stationary, non-slip, rigid and impermeable. The fluid to be used is air. Aspect ratio A=H/L=0.5, Where H is the height and L is the Length of the enclosure. The characteristic length is taken to be the size of the enclosure in the $x-$ direction.

Initially, air is motionless the temperature of which is equal to the average temperature of the vertical walls. Then temperature of the heater and that of the window are varied such that $T_h > T_w$ where T_h is the temperature of the heater and T_w the temperature of the window. This implies that the density gradient of the internal air is normal to the gravity and the buoyancy–driven natural convection starts immediately the heat is applied. Due to the buoyancy, a fluid motion is induced in the enclosure depending on the enclosure geometry (i.e. aspect ratio A=H/L), the working fluid (which in this study is air) and temperature difference $\Delta T = T_h - T_w$

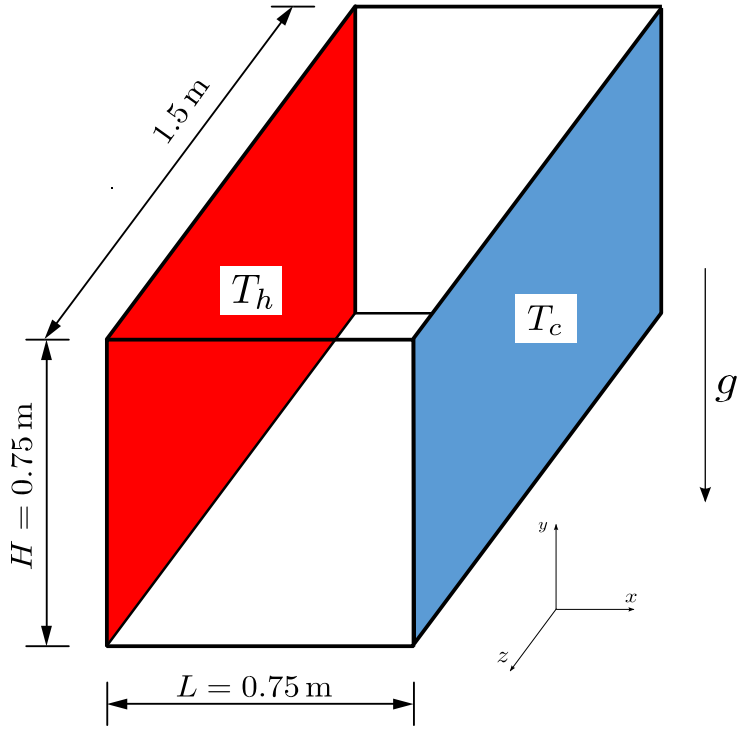

Fig. 3.3 Geometry of the 3-D numerical model

Furthermore, the Boussinesq Approximation (1903), as presented in section 3.7 below, is assumed. In this research, we will zero in on the standard $\kappa - \omega\, SST$ turbulence models as

documented by Awuor (2012) and study the variables as used by Ampofo and Karyiannis (2003). Besides this, we use the PISO algorithm, the SIMPLEC algorithm and the Finite Volume Method to numerically investigate the velocity, thermal and pressure profiles of air in this 3-D enclosure, any change in terms of accuracy and convergence time and any additional profiles.

3.7 Boussinesq Approximation

Boussinesq approximation applies if the Mach number of the flow is small and therefore the propagation of sound or shock waves is not considered, the vertical scale of the flow is not too large, and the temperature differences in the fluid are small, Boussinesq (1903). The following Boussinesq assumptions are made in this study.

i) All physical properties of the fluid are constant except the density in the buoyancy term.

ii) The fluid is Newtonian (i.e. exhibits a linear relationship between the shear stress and the velocity gradient) and that there is no internal heat source.

iii) The variations of density are small hence negligible, however even weak density variations are important in Buoyancy and so we shall retain variations in density due to buoyancy forces in the vertical equation of motion. We define buoyancy as;

$$b = g\frac{(\rho - \rho_o)}{\rho_o} \tag{3.88}$$

Where$(\rho - \rho_o)$ is the density variation due to buoyancy force, ρ_o the constant fluid density and g the gravitational force.

iv) The variation of density ρ, due buoyancy forces is proportional to the temperature difference ΔT.

v) The viscous dissipation effect may be neglected.

Since the density in the buoyancy term varies only with temperature and this variation is small, it follows that;

$$\rho = \rho_o + (T - T_o)(\frac{\partial \rho}{\partial T})_{T_o} \quad (3.89)$$

The coefficient of thermal expansion at constant pressure is defined as;

$$\beta_o = \frac{1}{\rho_o}(\frac{\partial \rho}{\partial T})_{T_o} \quad (3.90)$$

Re-arranging Eq. (3.90) yields;

$$\rho_o \beta_o = (\frac{\partial \rho}{\partial T})_{T_o} \quad (3.91)$$

Substitution of Eq. (3.91) into Eq. (3.89) gives;

$$\rho = \rho_o + \rho_o \beta_o (T - T_o) \quad (3.92)$$

Further re-arrangement of Eq. (3.92) using equation (3.91) yields;

$$\rho = \rho_o [1 + \beta_o (T - T_o)] \quad (3.93)$$

3.8 Simplifying Governing Equations

Using the Boussinesq approximation and making use of figure (3.93) into the governing equations, the equations governing natural convention of air in the enclosure are presented in non-dimensional form for an incompressible turbulent flow as follows:

The continuity equation (3.83) becomes;

$$\frac{\partial U_j}{\partial x_j} = 0 \tag{3.94}$$

The momentum equation (3.84) becomes;

$$\frac{\partial \rho U_i}{\partial t} + \frac{\partial}{\partial x_j}\rho U_i U_j = -\frac{\partial P}{\partial x_i} + \rho_o[1 + \beta_o(T - T_o)]g_i + \frac{\partial}{\partial x_j}\left[\mu\left(\frac{\partial U_i}{\partial x_j} + \frac{\partial U_i}{\partial x_i}\right) - \overline{u_i u_j}\right] \tag{3.95}$$

The energy equation (3.85) becomes;

$$\frac{\partial T}{\partial t} + \frac{\partial}{\partial x_j}U_j T = \frac{\partial}{\partial x_j}\left(\frac{\lambda_o}{C_P \rho_o U_* L_o}\frac{\partial T}{\partial x_j} - \overline{u_j T}\right) \tag{3.96}$$

The Turbulent kinetic energy equation (3.86) simplifies to;

$$\frac{\partial k}{\partial t}+\frac{\partial}{\partial x_j}U_i k=\frac{\mu_o}{\rho_o U_* L_o}\overline{u_j\frac{\partial}{\partial x_j}\upsilon\left(\frac{\partial u_\iota}{\partial x_j}+\frac{\partial u_j}{\partial x_\iota}\right)}-\frac{\partial}{\partial x_j}\overline{u_j\left(\frac{u_\iota u_\iota}{2}+\frac{P}{\rho}\right)}-\overline{u_\iota u_j}\frac{\partial U_i}{\partial x_j}$$

$$+\frac{gL_o}{U_*^2}\frac{\overline{\rho u_\iota}g_i}{\rho} \tag{3.97}$$

Or;

$$\frac{\partial k}{\partial t}+\frac{\partial}{\partial x_j}U_i k=\overline{u_j\frac{\partial}{\partial x_j}\upsilon\left(\frac{\partial u_\iota}{\partial x_j}+\frac{\partial u_j}{\partial x_\iota}\right)}-\frac{\partial}{\partial x_j}\overline{u_j\left(\frac{u_\iota u_\iota}{2}+\frac{P}{\rho}\right)}+P_k+G_k \tag{3.98}$$

where;

$$P_k=\overline{u_\iota u_j}\frac{\partial U_i}{\partial x_j},\text{and }\ G_k=\frac{\overline{\rho u_\iota}g_i}{\rho} \tag{3.99}$$

Specific dissipation equation (3.87) becomes;

$$\frac{\partial}{\partial t}(\rho\omega)+\frac{\partial}{\partial x_i}(\rho\omega u_i)=\frac{\partial}{\partial x_j}\left[\left(\mu+\frac{\mu_t}{\sigma_\omega}\right)\frac{\partial\omega}{\partial x_j}\right]+G_\omega-Y_\omega+D_\omega \tag{3.100}$$

Where $\tilde{G}_k$ represents the generation of turbulent kinetic energy that arises due to mean velocity gradients and G_ω is the generation of ω which are defined in the exact manor as the K-epsilon model. Y_k and Y_ω represent the dissipation of κ and ω due to turbulence. α_κ and α_ω are turbulent Prandtl numbers for κ and ω respectively. Although the density variations are neglected everywhere in our case we note that where they cause buoyancy forces, like in the G_k term of equation (3.99) they are not neglected. These terms contribute to the generation of motion and thus cannot be neglected (Launder, 1988;Gatheri, 1994).

3.9 $\kappa - \omega$ *SST* Model

The SST model is a combination of the $\kappa - \varepsilon$ and $\kappa - \omega$ models. A blending function, which is dependent on the local turbulent variables, is used to switch between the models. The shear Stress transport $\kappa - \omega$ model is the only variation of the standard k-omega model available in FLUENT. It was developed by Menter (1994) using the standard k-omega model and a transformed $\kappa - \varepsilon$ model. The main difference is the way in which the model represents the turbulent viscosity to account for the transport of the principal turbulent shear stress.

This model also incorporates a cross-diffusion term in the ω equation and a blending function triggers the standard k- ω model in near wall regions, and triggers the $\kappa - \varepsilon$ -like model in the areas away from the surface. This is because, the $\kappa - \varepsilon$ model is generally accurate in shear type flows and is well behaved in the far field, while the $\kappa - \omega$ model is more accurate and more numerically stable in the near wall region. These differences make the SST model more precise for a larger variety of flows than the standard model.

Similar to the $\kappa - \omega$ model, the transport equations for κ and ω are slightly modified and are given by;

$$\frac{\partial}{\partial t}(\rho\kappa) + \frac{\partial}{\partial x_i}(\rho\kappa u_i) = \frac{\partial}{\partial x_j}\left[\left(\mu + \frac{\mu_t}{\sigma_k}\right)\frac{\partial k}{\partial x_j}\right] + \tilde{G}_k - Y_\kappa + S_K \tag{3.101}$$

$$\frac{\partial}{\partial t}(\rho\omega) + \frac{\partial}{\partial x_i}(\rho\omega u_i) = \frac{\partial}{\partial x_j}\left[\left(\mu + \frac{\mu_t}{\sigma_\omega}\right)\frac{\partial \omega}{\partial x_j}\right] + G_\omega - Y_\omega + D_\omega + S_\omega \tag{3.102}$$

Where $\tilde{G}_k$ represents the generation of turbulent kinetic energy that arises due to mean velocity gradients and G_ω is the generation of ω which are defined in the exact manner as the K-epsilon model. Y_k and Y_ω represent the dissipation of κ and ω due to turbulence. α_κ and α_ω are turbulent Prandtl numbers for κ and ω respectively and S_ω and S_κ are source terms defined by the user (i.e., user defined source terms). The D_ω is the cross-section diffusion and it blends the standard k-epsilon model and the standard k-omega model and is defined as;

$$D_\omega = 2(1 - F_1)\rho\sigma_{\omega,2}\frac{1}{\omega}\frac{\partial\kappa}{\partial x_j}\frac{\partial\omega}{\partial x_j} \tag{3.103}$$

Where F_1 is the blending function constant. The term $\tilde{G}_k$ represents the production of turbulence kinetic energy and is defined as;

$$\tilde{G}_k = \min\left(G_{k,}10\rho\beta^*\kappa\omega\right) \tag{3.104}$$

Where G_k is defined in the same manner as in the $\kappa - \omega$ model. The term G_k represents the production of turbulent kinetic energy. From the exact equation for the transport of k, may be defined as;

$$G_k = -\overline{\rho u_i' u_i'}\frac{\partial u_j}{\partial x_i} \tag{3.105}$$

To evaluate G_k in a manner consistent with the Boussinesq hypothesis,

$$G_k = \mu_t S^2 \tag{3.106}$$

Where S in the equation represents the modulus of mean rate-of-strain tensor, defined as;

$$S = \sqrt{2S_{ij}S_{ij}} \tag{3.107}$$

The term G_ω represents the production of ω and is given is given by;

$$G_\omega = \frac{\alpha}{v_t} G_\kappa \tag{3.108}$$

This differs from that of the standard $\kappa - \omega$ model. The Turbulent viscosity is computed in a different way from that used in the standard model and is given by;

$$\mu_t = \frac{\rho\kappa}{\omega} \frac{1}{\max\left[\frac{1}{\alpha^*}, \frac{SF_2}{a_1\omega}\right]} \tag{3.109}$$

Where S is the strain rate magnitude and $\alpha^*$is the damping coefficient calculated using;

$$\mu_t = \alpha^* \frac{\rho\kappa}{\omega} \tag{3.110}$$

The turbulent Prandtl numbers which were constant in the standard model are equated below and incorporate the blending functions F_1 and F_2. Blending functions have been added to the $\kappa - \omega$ SST model to ensure that the model equations behave appropriately in both near wall and far field zones.

$$\sigma_\kappa = \frac{1}{F_1/\sigma_{\kappa,1} + (1 - F_1)/\sigma_{\kappa,2}} \tag{3.111}$$

$$\sigma_\omega = \frac{1}{F_1/\sigma_{\omega,1} + (1-F_1)/\sigma_{\omega,2}} \tag{3.112}$$

Where the blending functions, F_1 and F_2, are given by;

$$F_1 = \tanh(\Phi_1^4) \;\; F_2 = \tanh(\Phi_2^2)$$

$$\Phi_1 = \min\left[\max\frac{\sqrt{\kappa}}{0.09\omega y}, \frac{500\mu}{\rho y^2 \omega}\right)\frac{4\rho\kappa}{\sigma_{\omega,2} D_\omega^+ y^2}]$$

$$D_\omega^+ = \max\left[2\rho\frac{1}{\sigma_{\omega,2}}\frac{1}{\omega}\frac{\partial\kappa}{\partial x_j}\frac{\partial\omega}{\partial x_j}10^{-10}\right]$$

$$\Phi_2 = \max\left[2\frac{\sqrt{\kappa}}{0.09\omega y}, \frac{500\mu}{\rho y^2\omega}\right] \tag{3.113}$$

Where y the distance to the next is surface and D_ω^+ is the positive portion of the cross-diffusion term. The other constants specific to the SST $\kappa-$omega model are given as;

$\sigma_{\omega,1} = 2.0,\ \sigma_{\omega,2} = 1.168,\ \sigma_{k,1} = 1.176,\ \sigma_{k,2} = 1.0,\ a_1 = 0.31,\ \beta_{i,2} = 0.0828,\ \beta_{i,1} = 0.075.$

The transport equations for the SST $\kappa - \omega$ model can also be written in terms of effective diffusivity of κ and ω, as;

$$\frac{\partial}{\partial t}(\rho\kappa) + \frac{\partial}{\partial x_i}(\rho\kappa u_i) = \frac{\partial}{\partial x_j}\left[\Gamma_\kappa \frac{\partial k}{\partial x_j}\right] + \tilde{G}_k - Y_\kappa + S_K \tag{3.114}$$

$$\frac{\partial}{\partial t}(\rho\omega) + \frac{\partial}{\partial x_i}(\rho\omega u_i) = \frac{\partial}{\partial x_j}\left[\Gamma_\omega \frac{\partial \omega}{\partial x_j}\right] + G_\omega - Y_\omega + D_\omega + S_\omega \tag{3.115}$$

Where Γ_κ and Γ_ω represent the effective diffusivity of κ and ω, respectively, which are given as;

$$\left.\begin{aligned} \Gamma_\kappa &= \mu + \frac{\mu_t}{\sigma_k} \\ \Gamma_\omega &= \mu + \frac{\mu_t}{\sigma_\omega} \end{aligned}\right\} \tag{3.116}$$

3.9.1 Dissipation of κ

The term Y_κ represents the dissipation of turbulence kinetic energy, and is defined in a similar manner as in the standard $\kappa - \omega$ model. The difference is as follows:-

- In the standard $\kappa - \omega$ model, f_{β^*} is defined as a piecewise function. For the SST $\kappa - \omega$ model, f_{β^*} is a constant equal to 1. Thus;

$$Y_\kappa = \rho\beta^*\kappa\omega \tag{3.117}$$

3.9.2 Dissipation of ω

The term Y_ω represents the dissipation of ω and is defined in a similar manner as in the standard model $\kappa - \omega$ model. The difference is as follows;

- In the standard $\kappa - \omega$ model, $\beta_i = 0.072$ and f_β is defined in the equation (3.117) as;

$$\left.\begin{aligned} f_\beta &= \frac{1 + 70x_\omega}{1 + 80x_\omega} \\ x_\omega &= \left|\frac{\Omega_{ij}\Omega_{ij}\Omega_{ij}}{(\beta^*_\infty)^3}\right| \\ \Omega_{ij} &= \frac{1}{2}\left(\frac{\partial\, u_i}{\partial\, x_j} - \frac{\partial\, u_j}{\partial\, x_i}\right) \end{aligned}\right\} \tag{3.118}$$

For the SST $\kappa - \omega$ model, f_β is a constant equal to 1. Thus, $Y_\omega = \rho\beta^*\omega^2$ becomes;

$$Y_\omega = \rho\beta f_{\beta^*}\kappa\omega^2 \tag{3.119}$$

Instead of having a constant value, β_i is given by;

$$\beta_i = F_1\beta_{i,1} + (1 - F_1)\beta_{i,2} \tag{3.120}$$

And F_1 is as expressed in equation (3.113).

3.10 Boundary conditions

The following boundary conditions will apply for both PISO and SIMPLEC algorithms.

3.10.1 Temperature Boundary conditions

The choice of the non-dimensional Θ temperature will be such that $0 \leq \Theta \leq 1$; where $\Theta = (T - T_*)/\Delta T_*$, so Θ is set at 1 on the heater and Θ is zero at the window. ΔT_* is the characteristic temperature difference between the hot and the cold surfaces, i.e., $\Delta T_* = T_h - T_w$ in which T_h is the temperature of the heater and T_w is the temperature of the window.

3.10.2 Thermal Boundary conditions

The problem at hand involves heating the left part of one wall and cooling on the right part of the same wall, the two thermal conditions that were used are:-

- Isothermal – for the vertical walls, represented by the equation $\Theta =$ Constant. On the heater and the window, the Dirchlet boundary conditions apply in which $\Theta_{hot} = 1$ and $\Theta_{cold} = 0$.
- Adiabatic – for the floor and the roof. The Neumann boundary condition applies in which $\frac{\partial \Theta}{\partial n} = 0$ for the floor and roof (n refers to the direction normal to a wall). For Instance, on the floor or $x - y$ plane; $\frac{\partial \Theta}{\partial z} = 0$.
- Let the temperature of the heater be T_h and that of the window be T_w. The temperature of the heater and that of the window are varied such that $T_h > T_w$.

3.10.3 Velocity Boundary conditions

No slip boundary condition is used. This implies, at the solid boundary, the viscous fluid will have zero velocity relative to the wall. This is because, the particles of air close to the surface will not move along with the flow, given that the adhesive force is greater than the cohesive force. Consequently, the outermost molecules of the fluid are stuck to the surface upon which it flows. Hence $u = v = w = 0$ at the surface.

Free slip boundary condition is used. In this rectangular enclosure, each boundary is assumed impermeable. This implies the component of velocity normal to the surface/boundary is zero. Justifiably, mass cannot penetrate an impermeable solid surface. For instance, in the $x - y$ plane, $w = 0$ if the plane is stationary.

3.10.4 Pressure Boundary conditions for the Pressure-Correction Equation

Let the guessed pressure field $p^* = 760mmHg$. Then the value of p' at the boundary will be zero. It is useful to start from $p' = 0$ as the guess for all points, so that the solution for p' does not acquire a large absolute value.

Chapter four discusses the numerical method that assists us discretize the differential equations governing the dependent variable in order to get a set of algebraic equations that connects the values of the dependent variables for a group of grid points within a control volume. Thus discretized equation expresses the same physical information as the differential equation. The chapter also discusses the PISO and SIMPLEC algorithms used to solve the discretized differential equations.

CHAPTER FOUR

THE NUMERICAL METHOD

4.1 Introduction

After the conservation laws governing heat transfer, fluid flow and other related processes are expressed in differential form and modeled inform of temperature and velocity, they can be solved using numerical methods, rather than analytical methods as discussed in section 3.1.4, to determine pressure, temperature, mass flux, etc. for various situations and boundary conditions.

A discretization equation is an algebraic relationship that connects the values of the dependent variable to a group of grid points within a control volume. Due to computational limitations, the number of locations had to be finite. This type of equation was derived from the differential

equation governing the dependent variable and thus expresses the same physical information as the differential equation.

Our method for deriving the discretization was control volume formulation. To ensure that the discretization equation results are not dependent on the profile assumptions, the solution was checked for mesh independence. In the iterative process for solving a discretization equation, it was desirable to use over-relaxation and under-relaxation factors in order to speed up and slow down the changes, from iteration to iteration, in the values of the dependent variable. This was to avoid divergence improve convergence ability.

4.2 Discretization of the Solution Domain

The process of space discretization involves dividing the computational domain into a finite number of contagious control volumes, where the resulting statements express the exact conservation of relevant properties for each control volumes. At the centroid of each control volumes, the variable values are calculated. Interpolation is used to express variable values at the control volume surface in terms of the center values and suitable quadrature formulae are applied to approximate the surface and volume integrals.

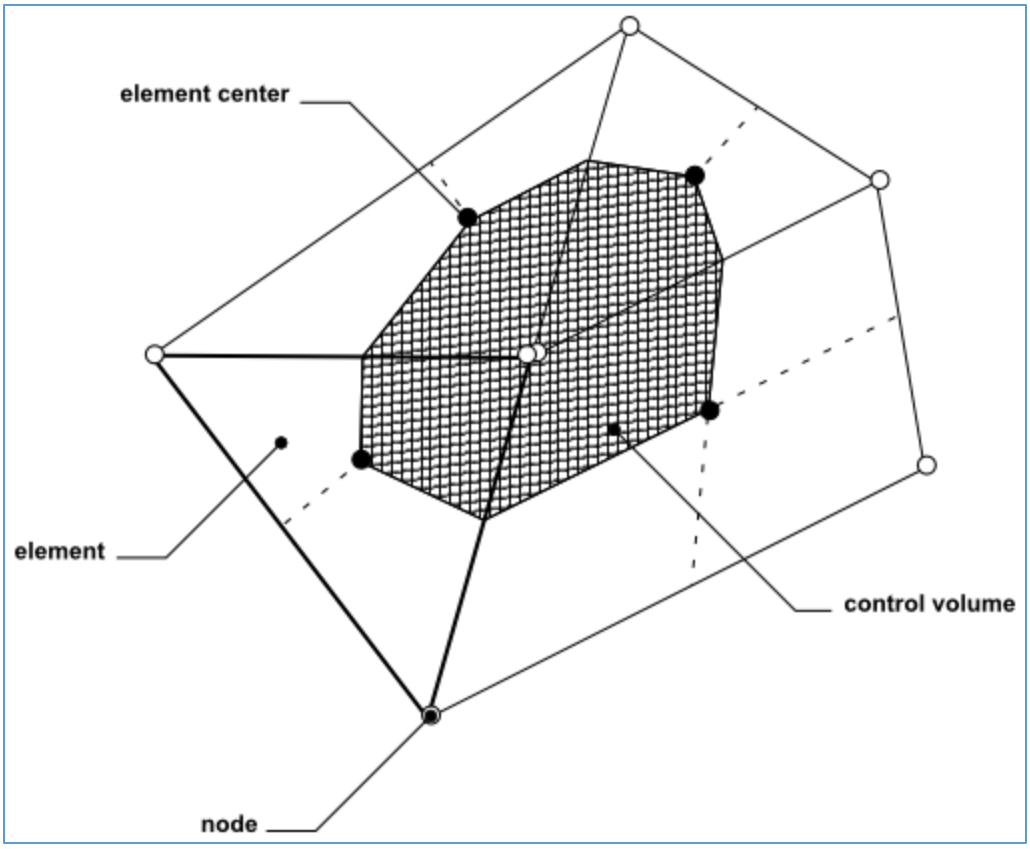

Fig. 4.1 Control-volume element

The figure 4.1, above shows a typical two-dimensional mesh. Finite Volume Method was preferred to Finite Difference Method for the following reasons:

i) Spatial discretization is totally flexible. Any type of cell shape can be employed that allow a large number of options for the definition of the shape and location of the control volumes tetrahedral in the case of 2-D and hexahedra in the 3-D. This type of unstructured mesh offers greater flexibility in order to accommodate irregularly shaped boundaries. Hence you can handle complex geometries, reduce geometric errors and give more resolutions in regions of interest.

ii) FVM naturally conserves variables when applied to PDEs expressing conservation laws since, as two neighboring cells share a common interface, the total flow of a conserved quantity out of one cell will be the same as that entering the other cell. As a result, mass, momentum and energy are conserved even on coarse grids.

iii) This method requires no transformation of equations in terms of body-fitted coordinate system as is required in Finite-Difference Method.

iv) FVM enjoys an advantage in memory use and speed for higher speed flows and turbulent flows.

4.3 Variable Arrangement on the Grid

Before describing the discretization scheme, choice of arrangement on the grid requires some consideration. Instead of a collocated grid, we used a staggered grid arrangement for this thesis computation in order to evaluate the velocity components at the control volume faces while the rest of the variables governing the flow field, such as the pressure, temperature, and turbulent quantities, are stored at the central node of the control volumes. A typical arrangement is depicted in figure 4.2, which is in 2-D, for convenience.

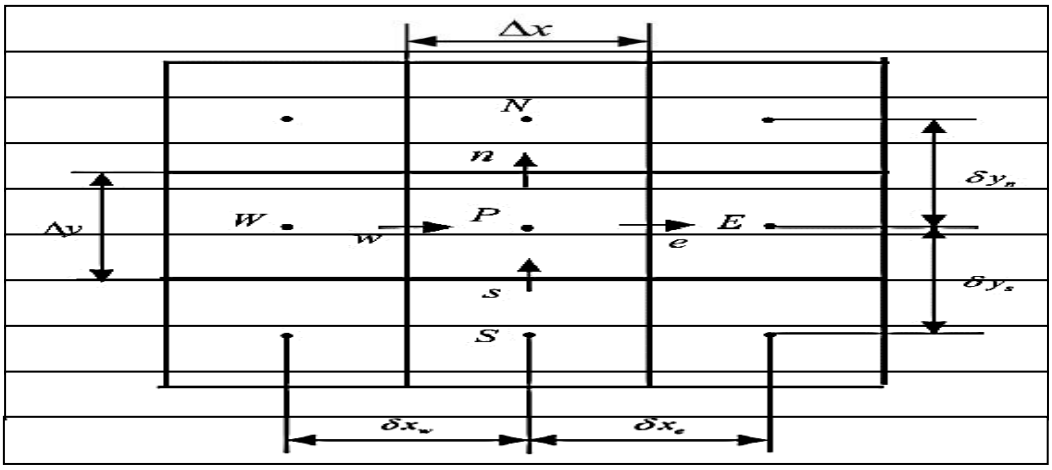

Fig. 4.2 control volumes in 2D.

It can be demonstrated that the discrete values of the velocity components, u, from the $x-$momentum equation are evaluated and stored at the east, e, and the west, w, faces of the control volume. By evaluating the other velocity components using the $y-$momentum and $z-$momentum equations on the rest of the control volume faces, these velocities allow a straightforward evaluation of the mass fluxes that are used in the pressure correction equation. This arrangement therefore provides a strong coupling between the velocities and pressure, which helps to avoid some types of convergence problems and oscillations in the pressure and velocity fields.

4.4 Discretization of the Governing Equations Using FVM

The process of discretization of the governing equations involved developing a set of algebraic equations (based on discrete points in the flow domain) to be used in the place of the partial differential equations. Basing on the advantages cited in section 4.1 above, we used FVM to discretize the governing equation.

For the finite-volume method, the computational domain is subdivided into a finite number of contagious control volumes, where the resulting statements express the exact conservation of relevant properties for each of the control volumes.

At the centroid of each of the control volumes, the variable values are calculated. Interpolation is used to express variable values at the control volume surface in terms of the centre values and suitable quadrature formulae are applied to approximate the surface and volume integrals. An algebraic equation for each of the control volumes can be obtained, in which a number of the neighboring nodal values appear.

4.5 Discretization of the Continuity Equation by FVM

Consider the continuity equation (3.94) in two dimensional form of figure 4.2. Integrating over the cell P and applying Gauss' divergence theorem to the volume integral, we get;

$$\frac{1}{\Delta V}\int_V \nabla . UdV = \frac{1}{\Delta V}\int_A UdA \tag{4.1}$$

Assuming that the velocity variable on the face is represented by its centroid value, we may write;

$$\frac{1}{\Delta V}\int_A UdA = \frac{1}{\Delta V}\sum_i U_i A_i \tag{4.2}$$

For a first-order derivative of U in two dimensions, the term along the x direction represented in equation (3.94), can be approximated by;

$$\left(\frac{\partial u}{\partial x}\right) = \frac{1}{\Delta V}\int_V \frac{\partial u}{\partial x} dV = \frac{1}{\Delta V}\int_A u dA^x \approx \frac{1}{\Delta V}\sum_{i=1}^{N} u_i A_i^x \tag{4.3}$$

Where u_i the velocity variable values at the elemental surfaces and N denotes the number of bounding surfaces on the elemental volume. For a quadrilateral element in 2-D for the structured mesh as seen in figure 4.2, N has the value of four since there are four bounding surfaces of the element. In 3-D, for a hexagonal element, N becomes six. Similarly, the first-order derivative for U in the y direction is obtained in the same fashion, which can be written as;

$$\left(\frac{\partial v}{\partial y}\right) = \frac{1}{\Delta V}\int_{\Delta V} \frac{\partial v}{\partial y} dV = \frac{1}{\Delta V}\int_A v dA^y \approx \frac{1}{\Delta V}\sum_{i=1}^{N} v_i A_i^y \tag{4.4}$$

It follows from equation (4.2) that the first order derivative for U in the z direction can be written as;

$$\left(\frac{\partial w}{\partial y}\right) = \frac{1}{\Delta V}\int_{\Delta V} \frac{\partial w}{\partial y} dV = \frac{1}{\Delta V}\int_A w dA^z \approx \frac{1}{\Delta V}\sum_{i=1}^{N} w_i A_i^z \tag{4.5}$$

For our considered mesh (orthogonal) in figure 4.2, using equations (4.2), (4.3) and (4.4), we get;

$$(u_e - u_w)\Delta y + (v_n - v_s)\Delta x = 0 \tag{4.6}$$

In 3-D, equation (4.6) becomes;

$$[(\rho u)_e - (\rho u)_w]\Delta y\Delta z + [(\rho v)_n - (\rho v)_s]\Delta z\Delta x + [(\rho w)_t - (\rho w)_b]\Delta x\Delta y = 0 \quad (4.7)$$

4.6 Discretization of the Momentum Equation by FVM

Consider the 2-D rectangular domain shown in figure 4.2. Assume that;

(i) the velocity vector U and the pressure P are stored at the cell centroids

(ii) a steady state

The momentum equation in equation (3.95) in x and y may be written as;

$$\nabla.(\rho V u) = \nabla.(\mu\nabla u) - \nabla P.i + S_u \quad (4.8)$$

$$\nabla.(\rho V v) = \nabla.(\mu\nabla u) - \nabla P.i + S_v \quad (4.9)$$

Each of the momentum equations contains a pressure gradient term, a source term (S_u and S_v) which contains the force term, as well as remnants of the stress tensor term.

Let us consider the pressure gradient term in the x-direction. In deriving discrete equations, we integrate the governing equations (4.8) over the cell volume. To integrate the pressure gradient over the control volume, we apply the gradient theorem, which yields;

$$\int_{\Delta V} \nabla P d\vartheta = \int_A P dA = (P_e - P_p)A_e \quad (4.10)$$

Assuming that pressure at the face centroid represents the mean value on the face, where $P_P - P_E$ represents the pressure difference and A_e is the area where the pressure difference acts. A second-order derivative along the x direction, for the diffusion terms represented in the momentum equation (4.8) can be evaluated as follows: - Consider the steady-state diffusion of the generic variable $\emptyset$ in one dimensional domain. The equation that governs such a process is given by;

$$\frac{\partial}{\partial x}\left(\Gamma\frac{\partial \emptyset}{\partial x}\right) + S_{\emptyset} = 0 \tag{4.11}$$

Where Γ is the diffusion coefficient and $S_{\emptyset}$ is the source term. In order to discretize equation (4.11) using FVM, we have to consider the physical domain as being divided into finite-control volumes surrounding the nodal points W, P and E as in figure 4.2. The distances between the nodes W and P, and between P and E, are identified by the respective notations δx_W and δx_E. For this one-dimensional case, the control volume width surrounding the nodal point P is Δx since Δy and Δz have dimensions of unit length. To apply the finite-volume discretization to the gradient term in equation (4.11) can be approximated by use of equation (4.3). This gives;

$$\frac{\partial}{\partial x}\left(\Gamma\frac{\partial u}{\partial x}\right)+S_u$$

$$=\frac{1}{\Delta V}\int_{\Delta V}\left[\frac{\partial}{\partial x}\left(\Gamma\frac{\partial u}{\partial x}\right)+S_u\right]dV$$

$$=\frac{1}{\Delta V}\int_{A}\left(\Gamma\frac{\partial u}{\partial x}\right)dA^x+\frac{1}{\Delta V}\int_{\Delta V}S_u dV\approx\frac{1}{\Delta V}\sum_{i=1}^{2}\left(\Gamma\frac{\partial u}{\partial x}\right)_i A_i^x$$

$$+\frac{1}{\Delta V}\int_{\Delta V}S_u dV \tag{4.12}$$

Here the projected areas A_i^x for the one-dimensional case are given by $A_1^x=-A_W$ and $A_2^x=A_E$, and the source term S_u is assumed to be constant within ΔV, which is the finite-control volume. The final form of the discretized equation becomes;

$$\frac{1}{\Delta V}\left(\Gamma\frac{\partial u}{\partial x}\right)_e A_E-\frac{1}{\Delta V}\left(\Gamma\frac{\partial u}{\partial x}\right)_w A_W+S_u=0 \tag{4.13}$$

To express an algebraic form for equation (4.13) with nodal points W, E and P, approximations to the gradients $\partial u/\partial x$ at the west (w) and east (e) faces of the control volume are required. We will assume the piecewise-linear gradient profiles spanning the nodal points between W and P and between P and E to sufficiently approximate the first-order derivatives at w and e; the diffusive fluxes are evaluated and equation (4.13) becomes;

$$\frac{\Gamma_e A_E}{\Delta V}\left(\frac{u_E-u_P}{\delta x_E}\right)-\frac{\Gamma_W A_W}{\Delta V}\left(\frac{u_P-u_W}{\delta x_W}\right)+S_u=0 \tag{4.14}$$

Equation (4.14) presents a very attractive feature of the finite –volume method. This discretized equation possess a clear physical interpretation. It states that the difference between the diffusive fluxes of ϕ at the east and west faces of the control volume equal to the generation of ϕ and constitutes a balance equation ϕ over the control volume. Equation (4.14) can be rearranged as;

$$\frac{1}{\Delta V}\left(\frac{\Gamma_e A_E}{\delta x_E}+\frac{\Gamma_w A_W}{\delta x_W}\right)u_P=\frac{1}{\Delta V}\left(\frac{\Gamma_e A_E}{\delta x_E}\right)u_E+\frac{1}{\Delta V}\left(\frac{\Gamma_w A_W}{\delta x_W}\right)u_W+S_u \tag{4.15}$$

As above, by identifying the coefficients of u_E and u_W in equation (4.15) as a_E and a_W and the coefficient of u_p as a_p, the algebraic form can be written as;

$$a_p u_p = a_E u_E + a_W u_W + b \tag{4.16}$$

Where;

$$a_E=\frac{\Gamma_e A_E}{\Delta V \delta x_E} \qquad a_W=\frac{\Gamma_w A_W}{\Delta V \delta x_W} \qquad a_P=a_E+a_W \qquad \text{and} \qquad b=S_u$$

equation (4.16) represents the discretized form through the finite-volume method for equation (4.11). For the one-dimensional problem considered here, the face areas A_E and A_W are unity since Δy and Δz have dimensions of unit length; the finite-control volume ΔV is therefore the width Δx.

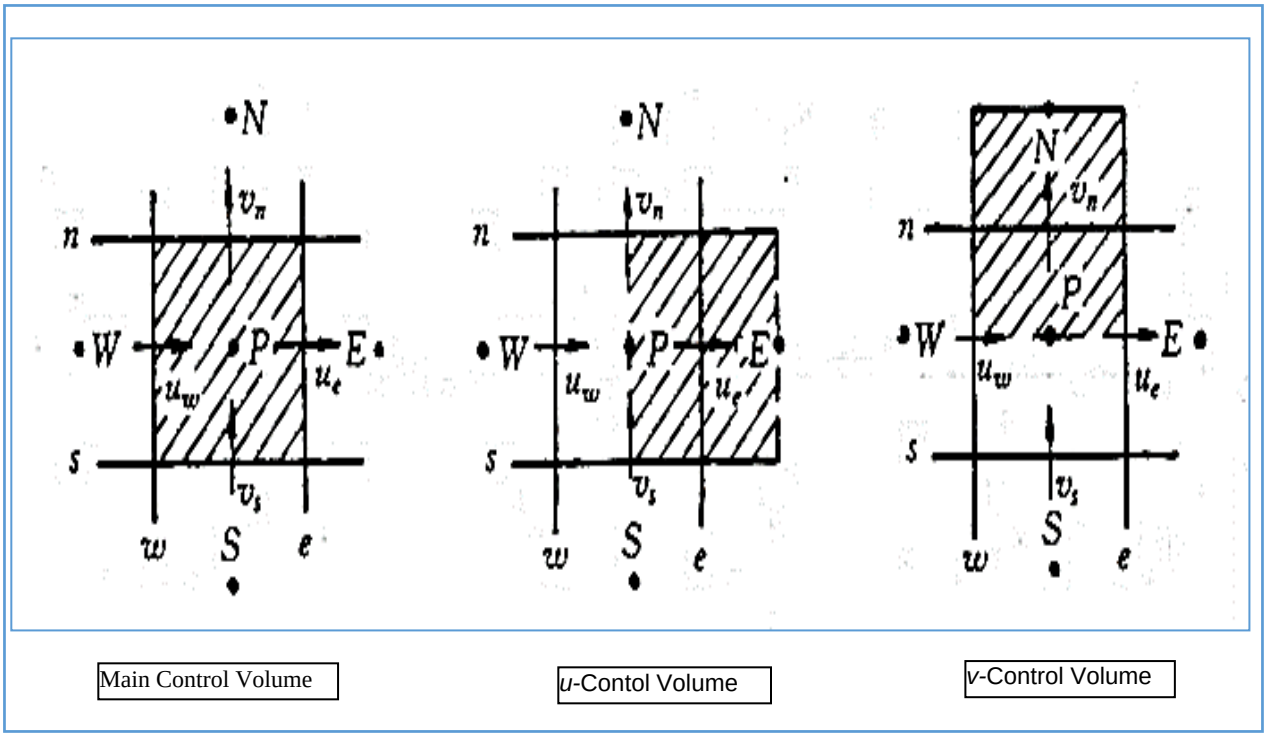

Fig. 4.3 The Staggered Grid $\frac{\partial p}{\partial x} = \frac{P_E - P_P}{(\partial x)_e} \frac{\partial p}{\partial y} = \frac{P_N - P_P}{(\partial y)_n}$

Let $a_E u_E + a_W u_W = a_{nb} u_{nb}$, using equations (4.8), (4.10) and (4.16), and a displaced or staggered grid for the velocity components as in figure 4.3, as used by Harlow and Welch (1965) in their MAC method, the resulting discretized momentum equation, in the x −direction, can be written

$$a_e u_e = \sum a_{nb} u_{nb} + b + (P_P - P_E) A_e \qquad (4.17)$$

Here the number of neighbor terms will depend on the dimensionality of the problem. For this three dimensional case, six neighbor u's would be included; where a_e is the coefficient for the main grid point, a_{nb} are the neighbor coefficients that account for the combined convection-diffusion at the control-volume faces. Here P is the main grid point. Its faces lie between the point e and the corresponding locations for the neighbor u's. The staggering is in the x direction

only, such that the faces normal to that direction pass through the main grid points P and E. Advantage− the difference $P_P - P_E$ can be used to calculate the pressure force acting on the control volume for the velocity u; $b = S_c\Delta x\Delta y + a_P^o\emptyset_P^o$ in which S_c is the source term quantity; $a_P^o = \frac{\rho_P^o\Delta x\Delta y\Delta z}{\Delta t}$. $\emptyset_P^o$ is the known value of the unsteady term at the time t i.e., at the beginning of the time step. The pressure term gives rise to the last term in equation (4.13). Since the pressure field will also be ultimately calculated, it is convenient to bury the pressures in the source term. The term $(P_P - P_E)A_e$ is the pressure force acting on the u control volume, A_e being the area which the pressure difference acts. For three-dimensional case, A_e will stand for $\Delta y\Delta z$.

The momentum equation for the other directions are handled in a similar manner. For instance, the y −direction momentum equation is staggered in the y −direction. Hence the discretization equation for v_n is given as;

$$a_n v_n = \sum a_{nb} v_{nb} + b + (P_P - P_N)A_n \tag{4.18}$$

where $(P_P - P_N)A_n$ is the pressure force acting on the v control volume, where A_n is the area which the pressure difference acts. (For 3-D case, A_n stands for $\Delta x\Delta z$. Similarly, the z −direction momentum equation is staggered in the z −direction and given as;

$$a_n w_t = \sum a_{nb} w_{nb} + b + (P_P - P_t)A_t \tag{4.19}$$

Where $(P_P - P_T)A_t$ is the appropriate pressure force. Where the location t, lies on the z −direction grid line between grid points P and T, Pantakar *et al* (1980). Where;

$(P_P - P_t)A_t$ is the pressure force acting on the w control volume, where A_n is the area which the pressure difference acts. (For 3-D case, A_t stands for $\Delta x \Delta y$). The momentum equations can be solved only when the pressure field is given or is somehow estimated.

Unless the correct pressure field is employed, the resulting velocity field will not satisfy the continuity equation. Such an imperfect velocity field based on the guessed pressure field p^* will be denoted by u^*, v^* and w^*. This starred velocity field will result from the Solution of the following discretization equations;

$$a_e u_e^* = \sum a_{nb} u_{nb}^* + b + (p_P^* - p_E^*)A_e \tag{4.20}$$

$$a_n v_n^* = \sum a_{nb} u_{nb}^* + b + (p_P^* - p_N^*)A_n \tag{4.21}$$

$$a_t w_t^* = \sum a_{nb} w_{nb}^* + b + (p_P^* - p_T^*)A_t \tag{4.22}$$

Where the location t lies on the $z-$direction grid line between grid points P and T.

4.7 The Pressure and Velocity Corrections

Our aim is to find a way of improving the guessed pressure p^* such that the resulting starred velocity field will progressively get closer to satisfying the continuity equation. Let the correct pressure p be obtained from;

$$p = p^* + p' \tag{4.23}$$

Where p' is the pressure correction.Next, we need to know how the velocity components respond to this change in pressure. The corresponding velocity corrections u^*, v^*, w^* can be introduced in a similar manner;

$$u = u^* + u', \quad v = v^* + v', \quad w = w^* + w' \tag{4.24}$$

When we subtract equations (4.20) from (4.17) we have;

$$a_e u_e - a_e u_e^* = \left\{\sum a_{nb} u_{nb} + b + (P_P - P_E)A_e\right\} - \left\{\sum a_{nb} u_{nb}^* + b + (p_P^* - p_E^*)A_e\right\} \tag{4.25}$$

Which results to;

$$a_e u_e' = \sum a_{nb} u_{nb}' + (p_P' - p_E')A_e \tag{4.26}$$

The PISO scheme we shall use approximates equation (4.26) by dropping of the term $\sum a_{nb}u'_{nb}$ from the equation for the following reasons;

i) PISO algorithm is an improvement on SIMPLE, which uses semi-implicit approach by dropping any term that would have an indirect influence of pressure correction on velocities

ii) on convergence, all the corrections tend to zero and there is no error induced on dropping $\sum a_{nb}u'_{nb}$ for obtaining the pressure equation.

iii) For computational convenience.

iv) PISO is an iterative approach and there is no reason why the formula designed to predict p' needs to be physically correct.

v) To expedite the convergence of the velocity field to a solution that satisfies the continuity equation, we are allowed to construct a formula for p' that is simply a numerical artifice.

The omission on equation (4.26) results to;

$$a_e u'_e = (p'_P - p'_E)A_e \tag{4.27}$$

Dividing equation (4.27) through by a_e yields;

$$u'_e = d_e(p'_P - p'_E) \tag{4.28}$$

In which case;

$$d_e \equiv \frac{A_e}{a_e} \tag{4.29}$$

Equation (4.28) will be called the velocity-correction formula. Using equation (4.24) we have;

$$u_e = u_e^* + u_e' \tag{4.30}$$

Replacing u_e' in equation (4.30), from equation (4.28) results to;

$$u_e = u_e^* + d_e(p_P' - p_E') \tag{4.31}$$

This shows how the starred velocity u_e^* is to be corrected in response to the pressure corrections to produce u_e. The correction formulas for the velocity components in other directions can be written similarly:

$$v_n = v_n^* + d_n(p_P' - \ p_N') \tag{4.32}$$

$$w_t = w_t^* + d_t(p_P' - p_T') \tag{4.33}$$

4.8 The Pressure Corrections Equation

We shall now turn the continuity equation into an equation for pressure correction. We shall assume that the density ρ does not directly depend on pressure, for the purpose of this three dimensional derivation.

The continuity equation (3.1) can be written as;

$$\frac{\partial \rho}{\partial t} + \frac{\partial (\rho u)}{\partial x} + \frac{\partial (\rho v)}{\partial y} + \frac{\partial (\rho w)}{\partial z} = 0 \tag{4.34}$$

We shall integrate equation (4.34) over the shaded control volume in figure 4.2, with the following assumptions;

(i) For the integration of the term $\frac{\partial \rho}{\partial t}$ we shall assume that the density ρ_P prevails over the control volume.

(ii) Velocity components such as u_e located on a control volume face will be supposed to govern the mass flow rate for the whole face.

With these assumptions, the integrated form of equation (4.34) becomes;

$$\frac{\rho_{P-}\rho_P^0)\Delta x\Delta y\Delta z}{\Delta t} + [(\rho u)_e - (\rho u)_w]\Delta y\Delta z + [(\rho v)_n - (\rho v)_s]\Delta z\Delta x + [(\rho w)_t - (\rho w)_b]\Delta x\Delta y = 0 \tag{4.35}$$

Substituting for all the velocity components the expressions given by the velocity-correction formulas, such as in equations (4.30) – (4.32) yields;

$$\frac{\rho_{P-}\rho_P^0)\Delta x\Delta y\Delta z}{\Delta t} + [\rho_e\{u_e^* + d_e(p_P' - p_E')\} - \rho_w\{u_w^* + d_w(p_W' - p_P')]\Delta y\Delta z + [\rho_n\{v_n^* + d_n(p_P' - p_N')\} - \rho_s\{v_s^* + d_s(p_S' - p_P')]\Delta z\Delta x + [\rho_t\{w_t^* + d_t(p_P' - p_T') - \rho_b\{w_b^* + d_b(p_B' - p_P')]\Delta x\Delta y = 0 \tag{4.36}$$

Re-arranging equation (4.36) results to;

$$\frac{\rho_{P-}\rho_P^0)\Delta x\Delta y\Delta z}{\Delta t} + [(\rho u^*)_e - (\rho u^*)_w]\Delta y\Delta z + [(\rho u^*)_n - (\rho u^*)_s]\Delta z\Delta x + [(\rho u^*)_t - (\rho u^*)_b]$$

$$- \rho_e d_e p'_E \Delta y\Delta z - \rho_w d_w p'_E \Delta y\Delta z - \rho_n d_n p'_N \Delta z\Delta x - \rho_s d_s p'_S \Delta z\Delta x - \rho_t d_t p'_T \Delta x\Delta y - \rho_b d_b p'_B \Delta x\Delta$$

$$= -(\rho_e d_e \Delta y\Delta z + \rho_w d_w \Delta y\Delta z + \rho_n d_n \Delta z\Delta x + \rho_s d_s \Delta z\Delta x + \rho_t d_t \Delta x\Delta y$$

$$+ \rho_b d_b \Delta x\Delta y) \qquad (4.37)$$

Multiplying equation (4.37) by a negative one yields;

$$\frac{(\rho_P^0 - \rho_P)\Delta x\Delta y\Delta z}{\Delta t} + [(\rho u^*)_w - (\rho u^*)_e]\Delta y\Delta z + [(\rho u^*)_s - (\rho u^*)_n]\Delta z\Delta x + [(\rho u^*)_b - (\rho u^*)_t]$$

$$+ \rho_e d_e p'_E \Delta y\Delta z + \rho_w d_w p'_E \Delta y\Delta z + \rho_n d_n p'_N \Delta z\Delta x + \rho_s d_s p'_S \Delta z\Delta x + \rho_t d_t p'_T \Delta x\Delta y$$

$$+ \rho_b d_b p'_B \Delta x\Delta y$$

$$= (\rho_e d_e \Delta y\Delta z + \rho_w d_w \Delta y\Delta z + \rho_n d_n \Delta z\Delta x + \rho_s d_s \Delta z\Delta x + \rho_t d_t \Delta x\Delta y$$

$$+ \rho_b d_b \Delta x\Delta y)p'_P \qquad (4.38)$$

Re-arranging equation (4.38), we obtain the following discretization; equation for p';

$$a_P p'_P = a_E p'_E + a_W p'_W + a_N p'_N + a_S p'_S + a_T p'_T + a_B p'_B + b \qquad (4.39)$$

Where;

$$
\begin{aligned}
a_E &= \rho_e d_e \Delta y \Delta z \\
a_W &= \rho_w d_w \Delta y \Delta z \\
a_N &= \rho_n d_n \Delta z \Delta x \\
a_S &= \rho_s d_s \Delta z \Delta x \\
a_T &= \rho_t d_t \Delta x \Delta y \\
a_B &= \rho_b d_b \Delta x \Delta y \\
a_P &= a_E + a_w + a_N + a_S + a_T + a_S \\
b &= \frac{(\rho_P^0 - \rho_P)\Delta x \Delta y \Delta z}{\Delta t} + [(\rho u^*)_w - (\rho u^*)_e]\Delta y \Delta z + [(\rho v^*)_s - \\
&\quad (\rho v^*)_n]\Delta z \Delta x + [(\rho w^*)_b \\
&\quad - (\rho w)_t]\Delta x \Delta y
\end{aligned}
\qquad (4.40)
$$

Since the values of the density ρ will normally be available only at main grid points, the interface densities such as ρ_e may be calculated by any convenient interpolation. It can be seen from equation (4.40) that the term b in the pressure-correction equation is essentially (the negative of) the left-hand side of the discretized continuity equation (4.35) evaluated in terms of the starred velocities. We have hence formulated all the equations needed for obtaining the velocity

components and pressure. The application of PISO algorithm, to solve equations (4.17), (4.18) and (4.19) is discussed in section (4.9).

4.9 The PISO Solution Algorithm

4.9.1 Predictor Step

The momentum equations can be solved only when the pressure field is given or is somehow estimated to initiate the PISO calculation process. The pressure field is estimated as p^* and the discretized momentum equations (4.17), (4.18) and (4.19) solved to yield an approximate velocity field component denoted by u^*, v^* and w^* as follows;

$$a_{i,j,k}u^*_{i,j,k} = \sum a_{nb}u^*_{nb} + (p^*_{i-1,j,k} - p^*_{i,j,k})A_{i,j,k} + b_{i,j,k} \tag{4.41}$$

$$a_{i,j,k}v^*_{i,j,k} = \sum a_{nb}v^*_{nb} + (p^*_{i,j-1,k} - p^*_{i,j,k})A_{i,j,k} + b_{i,j,k} \tag{4.42}$$

$$a_{i,j,k}w^*_{i,j,k} = \sum a_{nb}w^*_{nb} + (p^*_{i,j,k-1} - p^*_{i,j,k})A_{i,j,k} + b_{i,j,k} \tag{4.43}$$

The initial guess for the pressure may be correct or not.

4.9.2 Corrector Step 1

Velocity component obtained from predictor step may not satisfy the continuity equation, so we define correction factor p', w', v' and u' for pressure field and velocity field. Subtract the

guessed pressure field p^* from the correct pressure field p^{**} to get the pressure correction factor p' as in equation (4.44);

$$p'_{i,j,k} = p^{**}_{i,j,k} - p^{*}_{i,j,k} \tag{4.44}$$

Using equations (4.28), (4.43), and applying the pressure correction factor to solve the momentum equation (4.17), the corresponding correct velocity components u^{**},$v^{**}$and w^{**} are found as follows;

$$u^{**}_{i,j,k} = u^{*}_{i,j,k} + d_{i,j,k}\left(p'_{i-1,j,k} - p'_{i,j,k}\right) \tag{4.45}$$

$$v^{**}_{i,j,k} = v^{*}_{i,j,k} + d_{i,j,k}\left(p'_{i,j-1,k} - p'_{i,j,k}\right) \tag{4.46}$$

$$w^{**}_{i,j,k} = w^{*}_{i,j,k} + d_{i,j,k}\left(p'_{i,j,k-1} - p'_{i,j,k}\right) \tag{4.47}$$

Where $p^{**}_{i,j,k}{}^{**}, u^{**}_{i,j,k}{}^{**}, v^{**}_{i,j,k}{}^{**}, w^{**}_{i,j,k}{}^{**}$: Correct pressure field and velocity components in the x, y and z directions respectively. The first discretized pressure correction equation is deduced from the momentum equations and the continuity equation and can be expressed as, Pantaker (1980);

$$a_P p_P = \sum a_{nb} p_{nb} + b_P \tag{4.48}$$

In this particular case then, basing on equation (4.48), the first pressure correction equation into which mass fluxes as found at equations (4.45), (4.46), (4.47) are to be substituted to give the pressure correction factor, will be;

$$a_{i,j,k}p'_{i.j,k} = a_{i+1,j,k}p'_{i+1,j,k} + a_{i-1,j,k}p'_{i-1,j,k} + a_{i,j+1,k}p'_{i,j+1,k} + a_{i,j-1,k}p'_{i,j-1,k} + a_{i.j,k+1}p'_{i.j,k+1} + a_{i.j,k-1}p'_{i.j,k-1} + b'_{i,j,k} \quad (4.49)$$

With coefficients as given in equation (4.70).

4.9.3 Corrector Step 2

Using Operator splitting technique, the second velocity correction field can be found as follows;

$$a_{i,j,k}u^{**}_{i,j,k} = \sum a_{nb}u^{*}_{nb} + \left(p^{**}_{i-1,j,k} - p^{**}_{i,j,k}\right)A_{i,j,k} + b_{i,j,k} \quad (4.50)$$

$$a_{i,j.k}v^{**}_{i,j,k} = \sum a_{nb}v^{*}_{nb} + (p^{**}_{i,j-1,k} - p^{**}_{i,j,k})A_{i,j,k} + b_{i,j,k} \quad (4.51)$$

$$a_{i,j.k}w^{**}_{i,j,k} = \sum a_{nb}v^{*}_{nb} + (p^{**}_{i,j,k-1} - p^{**}_{i,j,k})A_{i,j,k} + b_{i,j,k} \quad (4.52)$$

$$a_{i,j,k}u^{***}_{i,j,k} = \sum a_{nb}u^{**}_{nb} + (p^{***}_{i-1,j,k} - p^{***}_{i,j,k})A_{i,j,k} + b_{i,j,k} \quad (4.53)$$

$$a_{i,j}v^{***}_{i,j,k} = \sum a_{nb}v^{**}_{nb} + (p^{***}_{i,j-1,k} - p^{***}_{i,j,k})A_{i,j,k} + b_{i,j,k} \quad (4.54)$$

$$a_{i,j.k}w^{***}_{i,j,k} = \sum a_{nb}v^{**}_{nb} + (p^{***}_{i,j,k-1} - p^{***}_{i,j,k})A_{i,j,k} + b_{i,j,k} \quad (4.55)$$

Note that the velocity in the term on the right hand side and in the term on the left-hand side are evaluated at different iteration levels, hence the algorithm is called ‘’ Operator splitting PISO algorithm’’. Subtracting equations (4.50), (4.51) and (4.52) from equation (4.53), (4.54) and (4.55) respectively yields;

$$a_{i,j,k}u^{***}_{i,j,k} - a_{i,j,k}u^{**}_{i,j,k} = \sum(a_{nb}u^{**}_{nb} - a_{nb}u^{*}_{nb}) + \left(p^{***}_{i-1,j,k} - p^{***}_{i,j,k}\right)A_{i,j,k} - (p^{**}_{i-1,j,k} - p^{**}_{i,j,k})A_{i,j,k} + b_{i,j,k} - b_{i,j,k} \quad (4.56)$$

$$a_{i,j,k}v^{***}_{i,j,k} - a_{i,j,k}v^{**}_{i,j,k} = \sum(a_{nb}v^{**}_{nb} - a_{nb}v^{*}_{nb}) + \left(p^{***}_{i,j-1,k} - p^{***}_{i,j,k}\right)A_{i,j,k} - (p^{**}_{i-1,j,k} - p^{**}_{i,j,k})A_{i,j,k} + b_{i,j,k} - b_{i,j,k} \quad (4.57)$$

$$a_{i,j,k}w^{***}_{i,j,k} - a_{i,j,k}w^{**}_{i,j,k} = \sum(a_{nb}w^{**}_{nb} - a_{nb}w^{*}_{nb}) + \left(p^{***}_{i,j,k-1} - p^{***}_{i,j,k}\right)A_{i,j,k} - (p^{**}_{i,j,k-1} - p^{**}_{i,j,k})A_{i,j,k} + b_{i,j,k} - b_{i,j,k} \quad (4.58)$$

Equations (4.56), (4.57) and (4.58) simplifies to;

$$a_{i,j,k}u^{***}_{i,j,k} = a_{i,j,k}u^{**}_{i,j,k} + \sum a_{nb}(u^{**}_{nb} - u^{*}_{nb}) + \left(p^{***}_{i-1,j,k} - p^{***}_{i,j,k}\right)A_{i,j,k} - \left(p^{**}_{i-1,j,k} - p^{**}_{i,j,k}\right)A_{i,j,k} + \left(p^{**}_{i-1,j,k} - p^{**}_{i,j,k}\right)A_{i,j,k} + b_{i,j,k} - b_{i,j,k} \quad (4.59)$$

$$a_{i,j,k}v_{i,j,k}^{***} = a_{i,j,k}v_{i,j,k}^{**} + \sum a_{nb}(v_{nb}^{**} - v_{nb}^{*}) + \left(p_{i,j-1,k}^{***} - p_{i,j,k}^{***}\right)A_{i,j,k} - \left(p_{i\,j-1,k}^{**} - p_{i,j,k}^{**}\right)A_{i,j,k} + b_{i,j,k} - b_{i,j,k} \quad (4.60)$$

$$a_{i,j,k}w_{i,j,k}^{***} = a_{i,j,k}w_{i,j,k}^{**} + \sum a_{nb}(w_{nb}^{**} - w_{nb}^{*}) + \left(p_{i,j,k-1}^{***} - p_{i,j,k}^{***}\right)A_{i,j,k} - \left(p_{i\,j,k-1}^{**} - p_{i,j,k}^{**}\right)A_{i,j,k} + b_{i,j,k} - b_{i,j,k} \quad (4.61)$$

Further simplification of equations (4.59), (4.60) and (4.61) results to;

$$u_{i,j,k}^{***} = u_{i,j,k}^{**} + \frac{\sum a_{nb}(u_{nb}^{**} - u_{nb}^{*})}{a_{i,j,k}} + d_{i,j,k}\left(p_{i-1,j,k}'' - p_{i,j,k}''\right) \quad (4.62)$$

$$v_{i,j,k}^{***} = v_{i,j,k}^{**} + \frac{\sum a_{nb}(v_{nb}^{**} - v_{nb}^{*})}{a_{i,j,k}} + d_{i,j,k}\left(p_{i,j-1,k}'' - p_{i,j,k}''\right) \quad (4.63)$$

$$w_{i,j,k}^{***} = w_{i,j,k}^{**} + \frac{\sum a_{nb}(w_{nb}^{**} - w_{nb}^{*})}{a_{i,j,k}} + d_{i,j,k}\left(p_{i,j,k-1}'' - p_{i,j,k}''\right) \quad (4.64)$$

where $d_{i,j,k} = \frac{A_{i,j,k}}{a_{i,j,k}}$; $p^{***}, v^{***}, u^{***}$ are correct pressure field and correct velocity components respectively and p'', v'', u'' are second correction pressure and velocity field respectively.

Therefore using equations (4.44), (4.45), (4.46)) and (4.47), pressure and velocities are corrected as follows;

$$p^{***}_{i,j,k} = p^{*}_{i,j,k} + p'_{i,j,k} + p''_{i,j,k} \tag{4.65}$$

$$u^{***}_{i,j,k} = u^{*}_{i,j,k} + d_{i,j,k}\left(p'_{i-1,j,k} - p'_{i,j,k}\right) + \frac{\sum a_{nb}(u^{**}_{nb} - u^{*}_{nb})}{a_{i,j,k}} + d_{i,j,k}\left(p''_{i-1,j,k} - p''_{i,j,k}\right) \tag{4.66}$$

$$v^{***}_{i,j.k} = v^{*}_{i,j,k} + d_{i,j,k}\left(p'_{i,j-1,k} - p'_{i,j,k}\right) + \frac{\sum a_{nb}(v^{**}_{nb} - v^{*}_{nb})}{a_{i,j,k}} + d_{i,j,k}\left(p''_{i,j-1,k} - p''_{i,j,k}\right) \tag{4.67}$$

$$w^{***}_{i,j,k} = w^{*}_{i,j,k} + d_{i,j,k}\left(p'_{i,j,k-1} - p'_{i,j,k}\right) + \frac{\sum a_{nb}(w^{**}_{nb} - w^{*}_{nb})}{a_{i,j,k}} + d_{i,j,k}\left(p''_{i,j,k-1} - p''_{i,j,k}\right) \tag{4.68}$$

The discretized second pressure correction equation is deduced from the momentum equations and the continuity equation and can be expressed as, Pantaker, (1980). In this particular case then, basing on equation (4.48), the second pressure correction equation into which mass fluxes as found at equations (4.66), (4.67), (4.68) are to be substituted to give the pressure correction factor, will be;

$$a_{i,j,k}p''_{i.j,k} =$$

$$a_{i+1,j,k}p''_{i+1,j,k} + a_{i-1,j,k}p''_{i-1,j,k} + a_{i,j+1,k}p''_{i,j+1,k} + a_{i,j-1,k}p''_{i,j-1,k} + a_{i.j,k+1}p''_{i.j,k+1} +$$

$$a_{i.j,k-1}p''_{i.j,k-1} + b''_{i,j,k} \qquad (4.69)$$

Where;

$$a_{i+1,j,k} = (\rho dA)_{i+1,j,k}$$

$$a_{i-1,j,k} = (\rho dA)_{i-1,j,k}$$

$$a_{i,j+1,k} = (\rho dA)_{i,j+1,k}$$

$$a_{i,j-1,k} = (\rho dA)_{i,j-1,k}$$

$$a_{i,j,k+1} = (\rho dA)_{i,j,k+1}$$

$$a_{i,j,k-1} = (\rho dA)_{i,j,k-1}$$

$$a_{i,j,k}$$

$$= a_{i+1,j,k}+a_{i-1,j,k}+a_{i,j+1,k}+a_{i,j-1,k}+a_{i,j,k+1}+a_{i,j,k-1} \qquad (4.70)$$

$$b = (\frac{\rho A}{a})_{i,j,k} \sum a_{nb}(u^{**}_{nb} - u^{*}_{nb}) - (\frac{\rho A}{a})_{i+1,j,k} \sum a_{nb}(u^{**}_{nb} - u^{*}_{nb}) +$$

$$(\frac{\rho A}{a})_{i,j,k} \sum a_{nb}(v^{**}_{nb} - v^{*}_{nb}) - (\frac{\rho A}{a})_{i,j+1,k} \sum a_{nb}(v^{**}_{nb} - v^{*}_{nb}) +$$

$$(\frac{\rho A}{a})_{i,j,k} \sum a_{nb}(w^{**}_{nb} - w^{*}_{nb})$$

$$- (\frac{\rho A}{a})_{i,j,k+1} \sum a_{nb}(w^{**}_{nb} - w^{*}_{nb})$$

This solution algorithm can be summarized in a flow chart as illustrated in the next section.

4.10 PISO Flow Chart

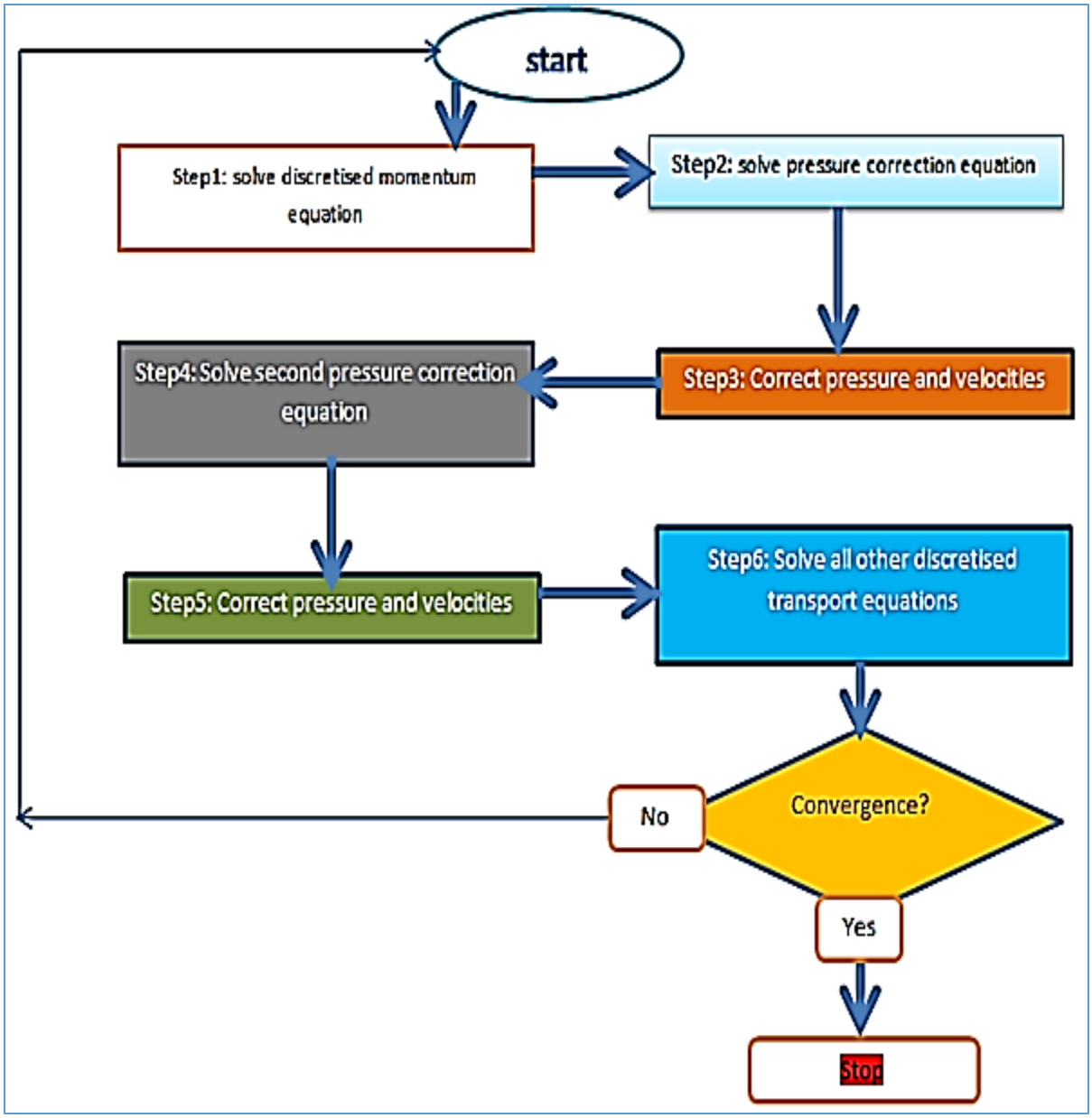

Fig 4.4 PISO Algorithm flow chart

4.11 The SIMPLEC Solution Algorithm

The SIMPLEC Algorithm follows the same steps as SIMPLE algorithm, with the difference being, the momentum equations are manipulated so that the SIMPLEC velocity correction equations omit terms that are less significant than those omitted in SIMPLE. Using equations (4.17), (4.18) and (4.19), the discretized momentum equations in 3-D are given as;

$$a_{i,j,k}u^{**}_{i,j,k} = \sum a_{nb}u^{**}_{nb} + (p^{**}_{i-1,j,k} - p^{**}_{i,j,k})A_{i,j,k} + b_{i,j,k} \tag{4.71}$$

$$a_{i,j,k}v^{**}_{i,j,k} = \sum a_{nb}v^{**}_{nb} + (p^{**}_{i,j-1,k} - p^{**}_{i,j,k})A_{i,j,k} + b_{i,j,k} \tag{4.72}$$

$$a_{i,j,k}w^{**}_{i,j,k} = \sum a_{nb}w^{**}_{nb} + (p^{**}_{i,j,k-1} - p^{**}_{i,j,k})A_{i,j,k} + b_{i,j,k} \tag{4.73}$$

The momentum equations will be solved by estimating the pressure field to initiate the SIMPLEC calculation process. The pressure field is estimated as p^* and the discretized momentum equations (4.71), (4.72) and (4.73) solved to yield approximate velocity field components denoted by u^*, v^* and w^* as follows:

$$a_{i,j,k}u^{*}_{i,j,k} = \sum a_{nb}u^{*}_{nb} + (p^{*}_{i-1,j,k} - p^{*}_{i,j,k})A_{i,j,k} + b_{i,j,k} \tag{4.74}$$

$$a_{i,j,k}v^{*}_{i,j,k} = \sum a_{nb}v^{*}_{nb} + (p^{*}_{i,j-1,k} - p^{*}_{i,j,k})A_{i,j,k} + b_{i,j,k} \tag{4.75}$$

$$a_{i,j,k}w^*_{i,j,k} = \sum a_{nb}w^*_{nb} + (p^*_{i,j,k-1} - p^*_{i,j,k})A_{i,j,k} + b_{i,j,k} \tag{4.76}$$

Velocity component obtained from predictor step may not satisfy the continuity equation, so we define correction factor p', w', v' and u' for pressure field and velocity fields. Hence $p' = p^{**} - p^*$, where p^* the guessed pressure is field and p^{**} is the correct pressure field. Using equations (4.71), (4.72), (4.73) and applying the pressure correction factor to solve the momentum equation (4.30) with equations (4.74), (4.75), (4.76) respectively, we get the corresponding correct velocity component u^{**}, v^{**} and w^{**}, as follows;

$$\begin{aligned} &a_{i,j,k}u^{**}_{i,j,k} - a_{i,j,k}u^*_{i,j,k} \\ &\quad = \sum a_{nb}u^{**}_{nb} + \left(p^{**}_{i-1,j,k} - p^{**}_{i,j,k}\right)A_{i,j,k} + b_{i,j,k} \\ &\quad - \left[\sum a_{nb}u^*_{nb} + \left(p^*_{i-1,j,k} - p^*_{i,j,k}\right)A_{i,j,k} + b_{i,j,k}\right] \end{aligned} \tag{4.77}$$

$$\begin{aligned} &a_{i,j,k}v^{**}_{i,j,k} - a_{i,j,k}v^*_{i,j,k} \\ &\quad = \sum a_{nb}v^{**}_{nb} + \left(p^{**}_{i,j-1,k} - p^{**}_{i,j,k}\right)A_{i,j,k} + b_{i,j,k} \\ &\quad - \left[\sum a_{nb}v^*_{nb} + \left(p^*_{i,j-1,k} - p^*_{i,j,k}\right)A_{i,j,k} + b_{i,j,k}\right] \end{aligned} \tag{4.78}$$

$$a_{i,j,k}w^{**}_{i,j,k} - a_{i,j,k}w^{*}_{i,j,k}$$

$$= \sum a_{nb}w^{**}_{nb} + \left(p^{**}_{i,j,k-1} - p^{**}_{i,j,k}\right)A_{i,j,k} + b_{i,j,k}$$

$$- \left[\sum a_{nb}v^{*}_{nb} + \left(p^{*}_{i,j-1,k} - p^{*}_{i,j,k}\right)A_{i,j,k} + b_{i,j,k}\right] \quad (4.79)$$

Which on simplification and re-arrangement yield;

$$a_{i,j,k}u'_{i,j,k} = \sum a_{nb}u'_{nb} + \left(p'_{i-1,j,k} - p'_{i,j,k}\right)A_{i,j,k} \quad (4.80)$$

$$a_{i,j,k}v'_{i,j,k} = \sum a_{nb}v'_{nb} + \left(p'_{i,j-1,k} - p'_{i,j,k}\right)A_{i,j,k} \quad (4.81)$$

$$a_{i,j,k}w'_{i,j,k} = \sum a_{nb}w'_{nb} + \left(p'_{i,j,k-1} - p'_{i,j,k}\right)A_{i,j,k} \quad (4.82)$$

SIMPLEC-Corrected (SIMPLEC) algorithm seeks to mitigate the effects of dropping velocity neighbor correction term $\sum a_{nb}u'_{nb}$ as in equation (4.27). SIMPLEC retains velocity correction terms, but makes an approximation as follows;

$$\sum a_{nb}u'_{nb} \approx u'_{i,j,k}\sum a_{nb}$$

$$\sum a_{nb}v'_{nb} \approx v'_{i,j,k}\sum a_{nb}$$

$$\sum a_{nb}w'_{nb} \approx w'_{i,j,k}\sum a_{nb}$$

Using the approximations above, equations (4.80), (4.81) and (4.82) become;

$$\left(a_{i,j,k} - \sum a_{nb}\right) u'_{i,j,k} = \left(p'_{i-1,j,k} - p'_{i,j,k}\right) A_{i,j,k} \tag{4.83}$$

$$\left(a_{i,j,k} - \sum a_{nb}\right) v'_{i,j,k} = \left(p'_{i,j-1,k} - p'_{i,j,k}\right) A_{i,j,k} \tag{4.84}$$

$$\left(a_{i,j,k} - \sum a_{nb}\right) w'_{i,j,k} = \left(p'_{i,j,k-1} - p'_{i,j,k}\right) A_{i,j,k} \tag{4.85}$$

From equations (4.83), (4.84) and (4.85), the correction factor $u'_{i,j,k}, v'_{i,j,k}$ and $w'_{i,j,k}$ for velocity fields can be written as;

$$u'_{i,j,k} = d_{i,j,k}\left(p'_{i-1,j,k} - p'_{i,j,k}\right) \tag{4.86}$$

$$v'_{i,j,k} = d_{i,j,k}\left(p'_{i,j-1,k} - p'_{i,j,k}\right) \tag{4.87}$$

$$w'_{i,j,k} = d_{i,j,k}\left(p'_{i,j,k-1} - p'_{i,j,k}\right) \tag{4.88}$$

where $d_{i,j,k} = A_{i,j,k} / \left(a_{i,j,k} - \sum a_{nb}\right)$

The initial guess for the pressure may be correct or not. Using the pressure-correction and velocity-correction equations (4.23) and (4.30) respectively, and equations (4.86), (4.87) and (4.88), we get the corresponding correct velocity component $u^{**}_{i,j,k}, v^{**}_{i,j,k}$ and $w^{**}_{i,j,k}$ and pressure correction written as;

$$u^{**}_{i,j,k} = u^{*}_{i,j,k} + d_{i,j,k}\left(p'_{i-1,j,k} - p'_{i,j,k}\right) \tag{4.89}$$

$$v^{**}_{i,j,k} = v^{*}_{i,j,k} + d_{i,j,k}\left(p'_{i,j-1,k} - p'_{i,j,k}\right) \tag{4.90}$$

$$w^{**}_{i,j,k} = w^{*}_{i,j,k} + d_{i,j,k}\left(p'_{i,j,k-1} - p'_{i,j,k}\right) \tag{4.91}$$

$$p^{**}_{i,j,k} = p^{*}_{i,j,k} + p'_{i,j,k} \tag{4.92}$$

We therefore then turn the continuity, as in equation (4.34) and solve for the pressure correction factor as in equation (4.39), which is to be used for pressure and velocities correction as summarized in figure 4.5 overleaf;

4.12 SIMPLEC Flow Chart

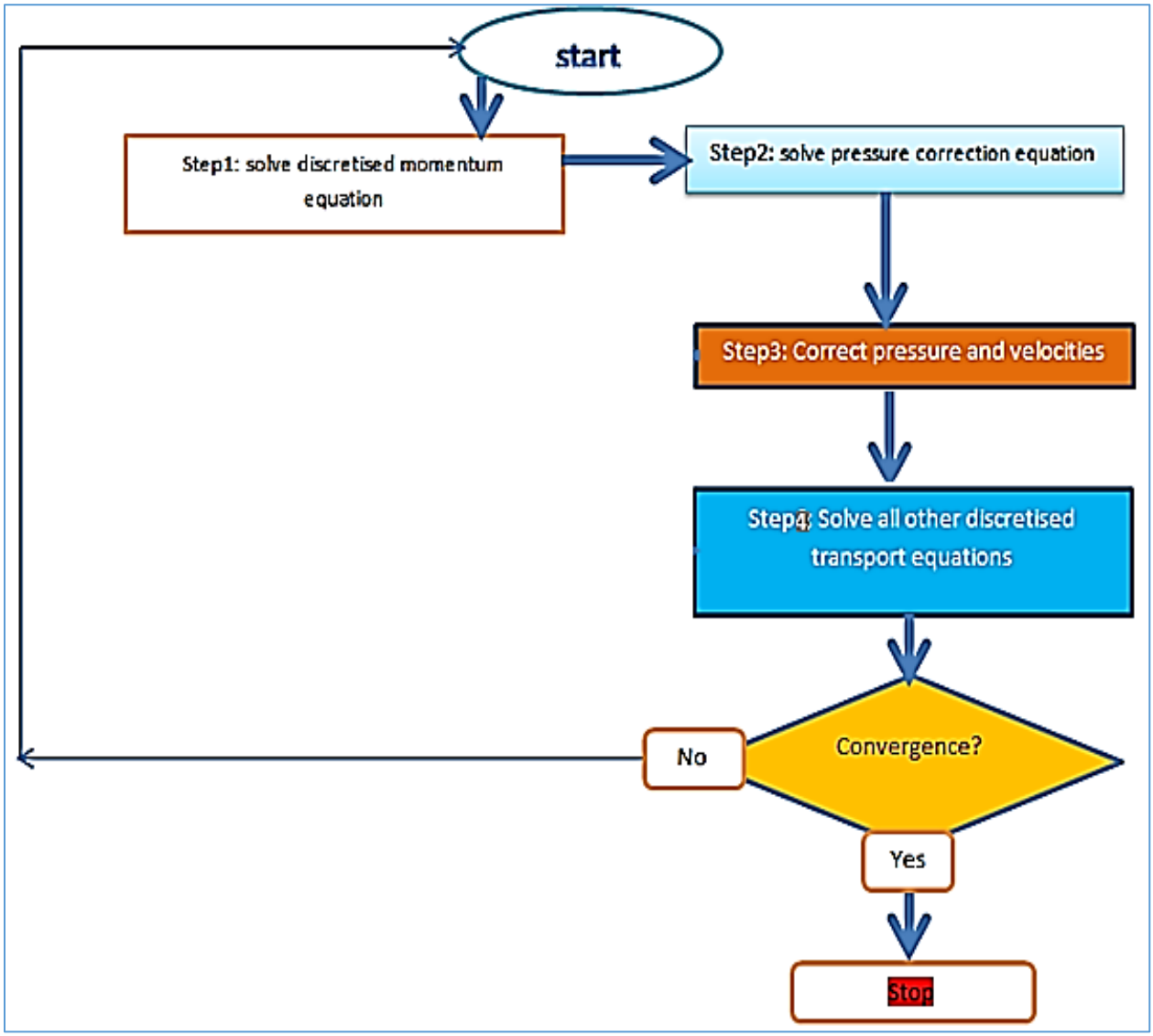

Fig 4.5 SIMPLEC Algorithm flow chart

4.13 Solver Settings and Validation

The numerical results for turbulent natural convection in a 3-D enclosure using the *k-ω SST* model and the PISO method will be validated against the experimental data provided by Ampofo and Karayiannis (2003). These authors conducted an experimental study of low-level turbulence in an air-filled vertical square cavity identical to the one in figure 3.3. This benchmark is at a Rayleigh number of 1.58×10^9. The local velocity and temperature were simultaneously measured at different locations in the cavity and the mean quantities were presented. In the present study, a computed turbulent buoyant flow with the low-Reynolds number, $k - w\ SST$ is carried out using Fluent 6.3.2 code. Unless otherwise noted, all temperature and velocity profiles are taken at half of the cavity height or Aspect ratio A=H/L= 0.5.

The case is set in Fluent 6.3.26 3-D model with a pressure based, segregated, unsteady implicit crank-Nickolson formulation with Green-Gauss Cell gradient treatment. PISO algorithm is selected for pressure-velocity coupling with relaxation factors of 0.3 for pressure, 0.7 for momentum, 1 for density and 1 for energy. The pressure was discretized with prestto. Second order upwind was set for momentum and energy discretization equation. The residuals criteria of convergence will be such as to reduce the absolute residuals by three orders of magnitude for all the variables in all cases. Turbulence was modelled using the *k-ω SST* model. The relaxation factors have been have been adjusted for each simulation in order to accelerate convergence. The Fluent 6.3.2 code we have applied, uses finite volume technique to discretize the Navier-Stokes equations.

In the next chapter, numerical results based on a PISO and SIMPLEC algorithm, will be validated and discussed.

CHAPTER FIVE

RESULTS AND DISCUSSION

The results presented here were obtained by solving equations (4.65), (4.66), (4.67), and (4.68) by PISO and equations (4.89), (4.90), (4.91) and (4.92) by SIMPLEC for turbulent natural convention of air in a 3-D enclosure of dimensions $0.75\text{m} \times 0.75\text{m} \times 1.5\text{m}$ and together with the following the boundary conditions; `

I. The choice of the non-dimensional Θ temperature was such that $0 \leq \Theta \leq 1$.

II. The Dirchlet boundary conditions apply on the heater and the window, while the Neumann boundary condition applies on the adiabatic walls.

III. No slip boundary condition is used at the solid wall boundary of the 3-D enclosure.

IV. Free slip boundary holds for the component of velocity normal to the impermeable wall surfaces.

V. The initial pressure correction value p' at the rigid and stationary wall boundary is zero.

The numerical results we have found with these boundary conditions are numerical solutions for variables in $k-\omega\, SST$ model, which will be validated against the experimental data provided by Ampofo and Karayiannis (2003). This benchmark is at a Rayleigh number of 1.58×10^9.

5.1 Grid Convergence

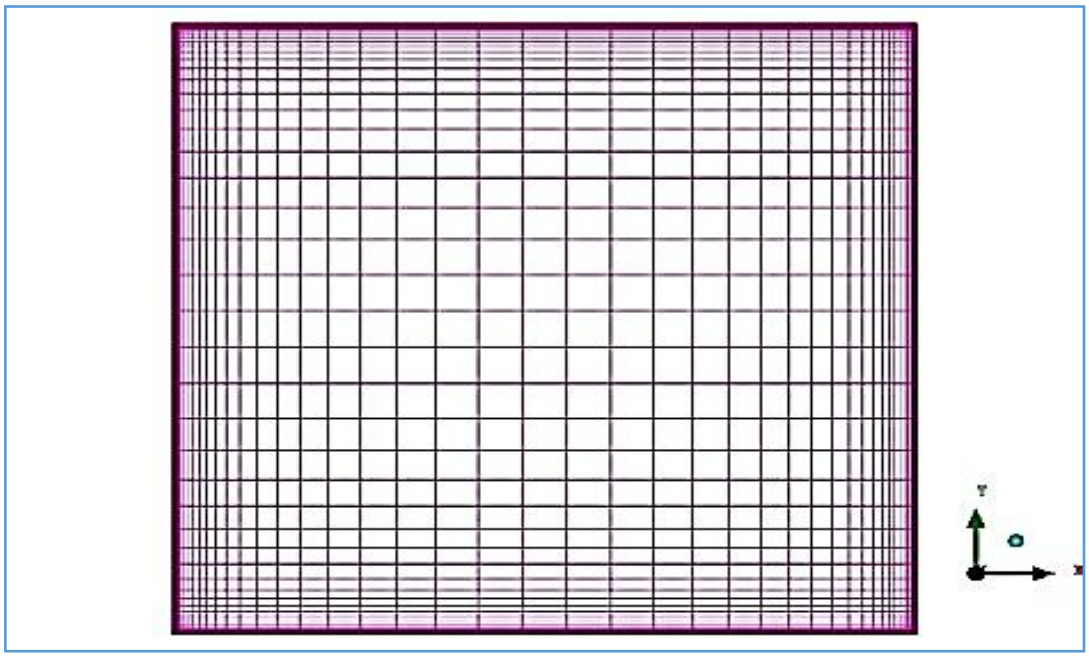

Fig 5.1 grid 80x80

The grid shown in figure 5.1 above is the standard grid used in these validations. The computational grids are staggered and clustered towards the walls. Grids are staggered so that the scalar variables like pressure, temperature, density and turbulent quantities are stored in the cell centres of the control volume whereas vector variables like velocity and momentum are located in the cell faces. This would provide a strong coupling between velocities and pressure. Hence the odd-even decoupling, a discretization error that would lead to checker-board patterns in the solution, leading to convergence issues is sorted out. Grids are clustered towards the wall because, the flow in turbulent natural convection in an enclosure is characterized by a thin boundary layer along the walls while the core is thermally stratified. The flow gradient are very large in the boundary layer and require a large number of computational grids, in which the values of dependent variables should be determined in order to capture the flow physics, hence

the adaptive refinement towards the isothermal walls which is our region of interest. All variables are calculated right up to the walls without using any wall function since the $k-\omega\ SST$ model would use its blending function to switch the model to the $k-\omega$ model which is more accurate and more numerically stable in the near wall regions. On the wall surface, the boundary values for the velocity components and the turbulent kinetic energy are set to zero in conformity with no slip boundary condition.

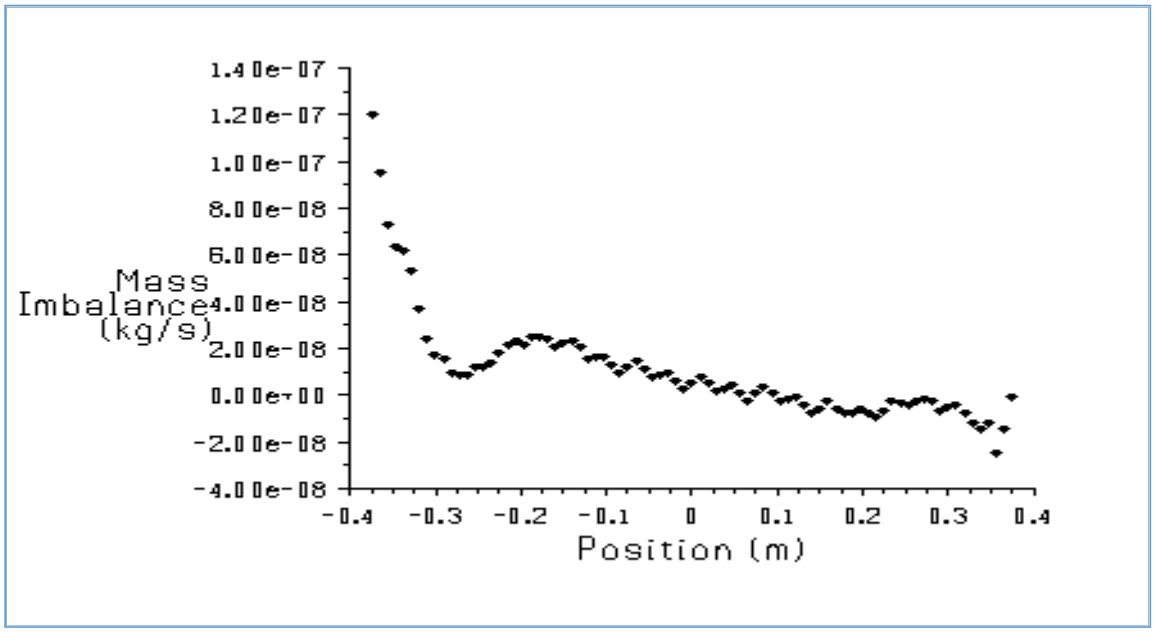

Fig 5.2 Mass imbalance profiles on an 80x80 grid

The dimensionless temperature of the cold and hot walls are 0 and 1 respectively.

For a numerical method to bear a stable discretization equation solution / a grid independent solution

i) The solved variables at all discrete cell locations should not change significantly with further grid refinement/ as the grid density increases.

ii) The computational domain should be devoid of distorted cells (long thin cells) because grid cell distortion leads to a poorly converged solution.

This outlines the importance of carrying out a mesh convergence test using a grid checker. This we did by carrying out a grid independence test. This was done by computing the numerical solution on successively finer grids. The difference in numerical solution between the coarse (80x80) and finer (160x160) grid, was to be taken as the accuracy measure of the coarse grid.

In this case, the 80x80 grid was refined by increasing the number of grid points to 160x160 for confirmation of grid independence. Figures 5.2 and 5.3 show a comparison of the residual mass imbalance profiles for the flow generated on each of the grids. The numerical implication is that as the mesh spacing or control volume size approached zero, the discretized equation solution matches the exact solution.

Initially we did a test run using a coarse mesh. This had the following advantages

i) It gave us the opportunity to evaluate the computers storage and running time.

ii) By this way, it was possible to assess the convergence and divergence behavior of the solutions

iii) The test run provided us with means of rectifying possible sources of solution errors such as physical modelling or human errors.

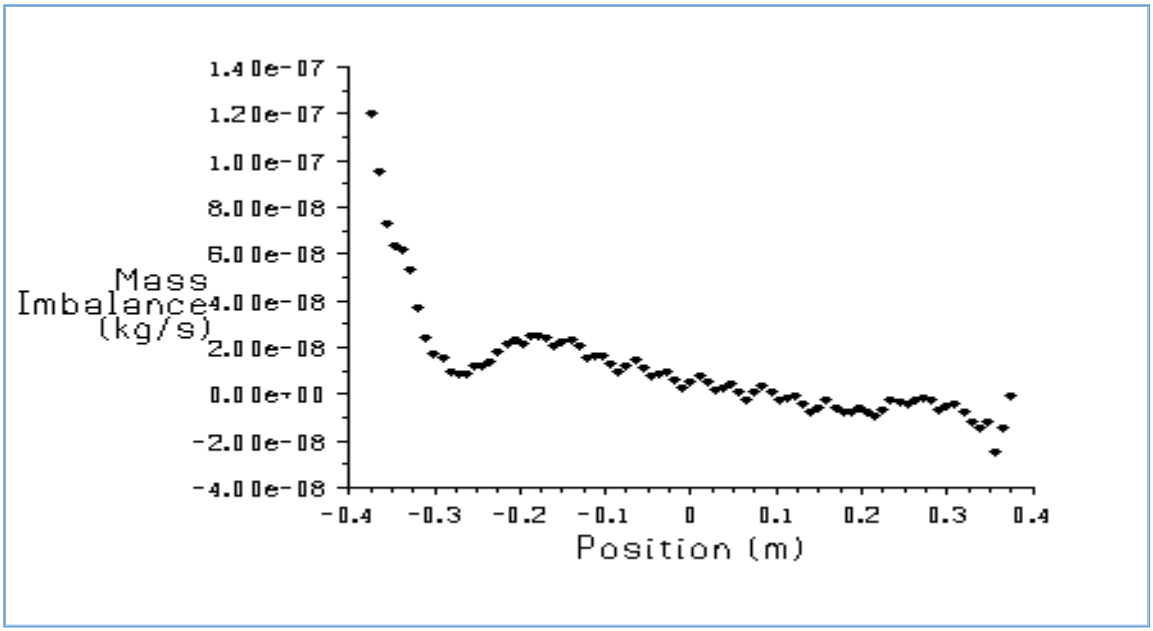

Fig 5.3 Mass imbalance grid on a 160x160 grid

Evidently, the results obtained on the 80x80 grid do not differ from those obtained on the 160x160 grid layout. Therefore, we can conclude the discretization error has diminished to zero and the grid independence has been reached.

Through the grid independence test we established that

i. the discretization equation results do not depend on profile assumption.

ii. we have reduced computational cost by finding an optimum grid size of the control volume, without compromising with the accuracy of the solution

5.2 Solution Convergence by PISO Method

It was necessary to check whether the numerical code produced a discretization equation solution that approached the exact solution of the differential equation as the grid spacing diminished to zero. This was meant to assist us know when to stop the simulation being run.

There were two indicators that convergence had been reached,

i) Solver residuals imbalance (history). Solver residual represent the absolute error in the solution of a particular variable. They represent the imbalances caused by the guesses made at each iteration. A reduction in residuals by three orders of magnitude was to indicate at least qualitative convergence. In this case residual plots would show when the residual values have reached the specified tolerance. At the point of convergence, all flow features would show.

The discretized equation for a general variable ∅ was deduced from the momentum equations and the continuity equation by Pantaker, (1980) and expressed in simple form as;

$$a_P \emptyset_P = \sum a_{nb} \emptyset_{nb} + b_P \qquad (5.1)$$

In equation (5.1), a_p is the coefficient for the main grid is point P and a_{nb} are the neighbor coefficients that account for the combined convection-diffusion terms at the control-volume faces. At the start of the simulation, the above equality would not hold.

The imbalance is called the residual, R_P, where;

$$R_P = a_P \emptyset_P - (\sum a_{nb} \emptyset_{nb} + b_P) \quad (5.2)$$

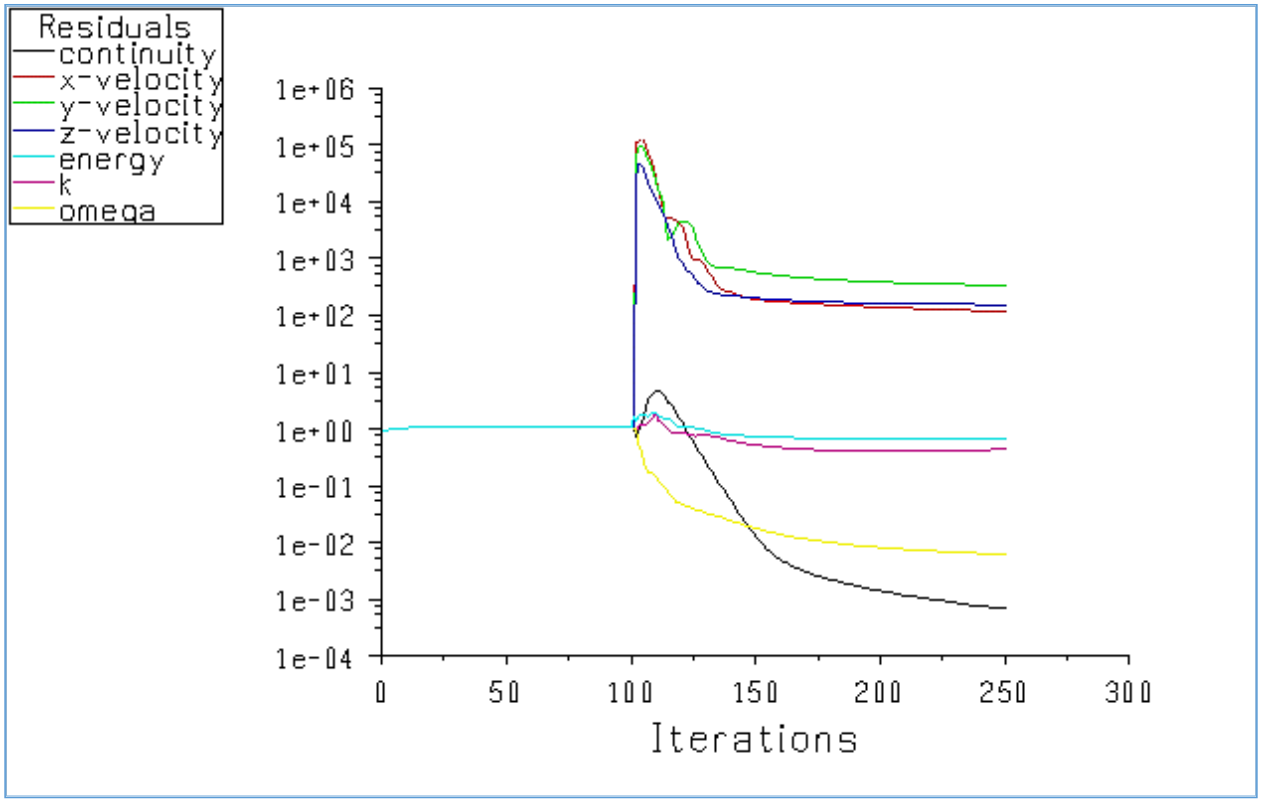

Fig 5.4 Scaled Residuals by PISO

ii) The choice of convergence criterion is problem and code-dependent.

a) Residual convergence criterion of 1e-03 was chosen for turbulent kinetic energy, specific dissipation rate and $x-, y-$and z – momentum equations and continuity equation, was applied because after reaching this specified tolerance, the solution had negligible mass imbalance (figure 5.2) and no longer changed with subsequent iterations. But the solution for energy was still changing at this point, so its convergence criterion had to be further reduced as in (b) overleaf.

b) Residual convergence criterion of 1e-06 was chosen for energy because it is at this point that all major flow features for energy were established and the solution no longer changed with subsequent iterations as the residuals stagnated.

In order to accelerate convergence, the following techniques were used

i) We ensured the problem under investigation was well posed/balanced by using a good physical model, realistic guesses and working boundary conditions.

ii) We supplied good initial conditions by computing an initial solution using a first-order discretization scheme such as first order-upwind

Actual problem	Initial condition
Heat Transfer	Isothermal
Natural convection	Low Reyleigh number
Turbulence	Inviscid

Table 5.1 Good Initial Conditions

iii) We gradually increased the under-relaxation factors. The process of slowing down the rate of change between iterations is called under-relaxation. To avoid divergence in the iterative solution of strongly nonlinear equations, under-relaxation is a very useful tool. Excessively high values could have led to instabilities and convergent issues. When running the simulation, under-relaxation was used to enable convergence whereby relaxation factors of 0.3 for pressure, 0.7 for momentum, 1 for density and 1 for energy were set.

At convergence, R_P was found to become negligible as iterations increased. The solution no longer changed after 250 iterations. Monitoring the representative flow variables through iterations showed that the residuals had stagnated and did not change with further iterations.

For PISO, the residual convergence criterion for each variable was achieved and the residual imbalance became negligible (i.e. the residuals had stagnated and did not change with further iterations) after 250 iterations in a duration of 45 minutes.

5.3 Solution Convergence by SIMPLEC Method

Just like for the case with the PISO method, Convergence was monitored with residuals, whereby a decrease in residuals imbalance by three orders of magnitude was to indicate qualitative convergence whereby case residual plots would show when the residual values have reached the specified tolerance.

A convergence of the root mean square residual of 1e-06 for energy and 1e-03 for turbulent kinetic energy, specific dissipation rate and $x-, y-$and z – momentum equations, was sufficient for significant physical results, as shown in figure 5.5. The residues had reduced to a sufficient degree.

The solution was to be deemed to have converged when the convergence criterion for each variable was reached. The default criterion was that each residual was to be reduced to a value of less than 10^{-3}, except the energy residual, for which the default criterion was 10^{-6}.

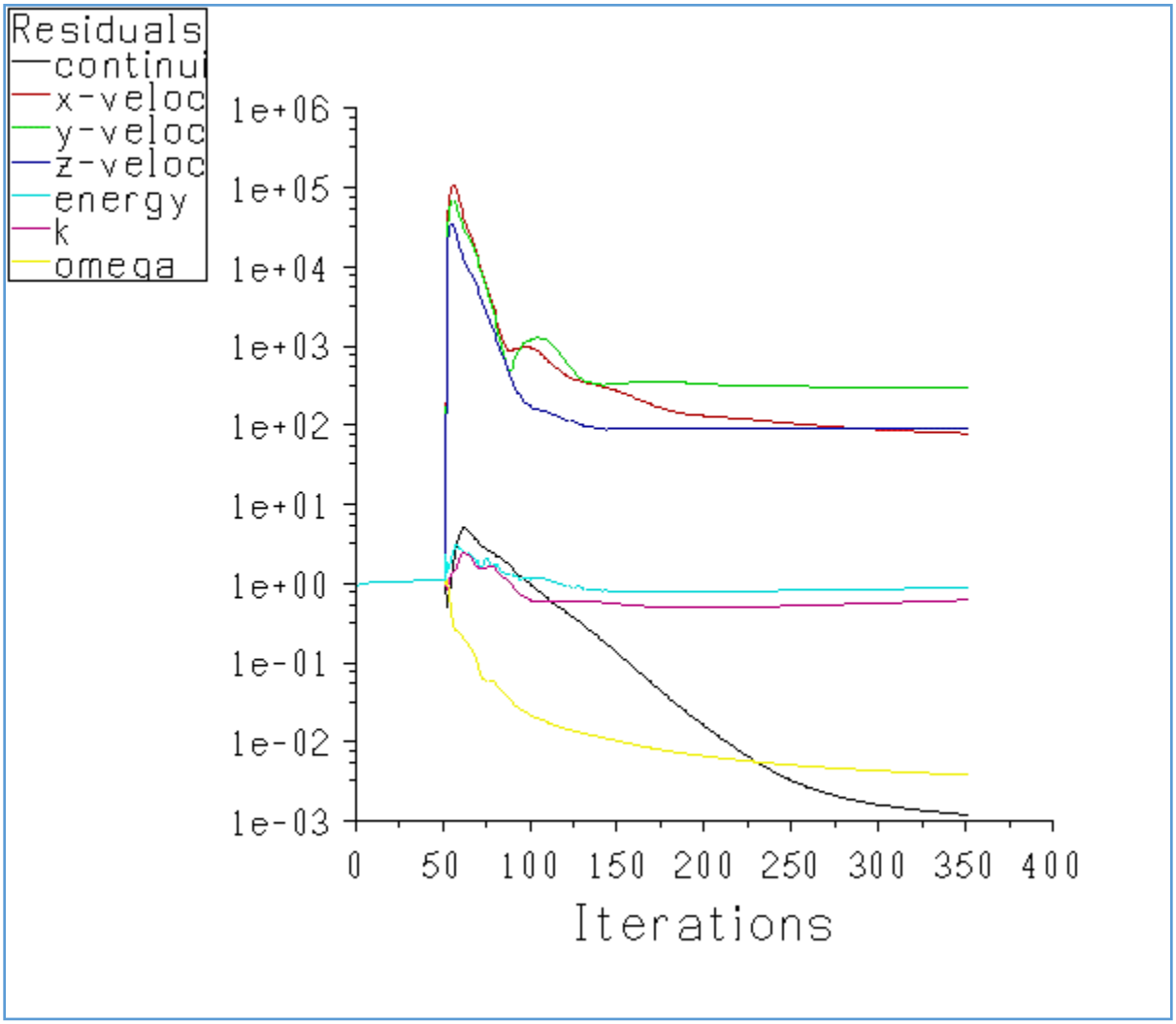

Fig 5.5 Scaled Residuals by SIMPLEC

In this case too, under-relaxation was used to enable convergence except for density, energy and body forces. The values used ranged from 0.3 to 0.9.

For SIMPLEC, the residual convergence criterion for each variable was achieved and the residual imbalance became negligible after 350 iterations in a duration of 1hr, 15min. This is because;

i) All discrete conservation equations of continuity, momentum and energy are obeyed in all control volume cells

ii) The imbalances caused by guesses made at each iteration have diminished to zero.

5.4 Validation of Results

Verification and Validation to assess the accuracy and reliability of results in this numerical code was done against the experimental solutions obtained from Ampofo and Karayiannis (2003).

5.4.1 Temperature Profiles

Figure 5.6 shows the predicted results at the mid x-y plane of the enclosure. The time-averaged temperature profile is estimated between the thermally active walls at the XY-mid-plane.

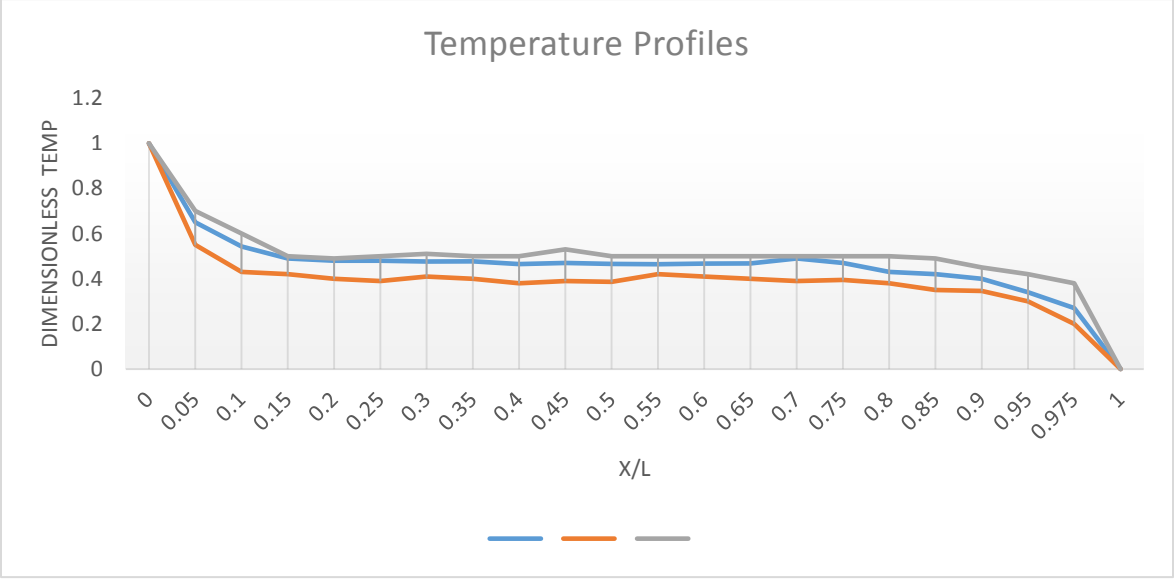

Figure 5.6 Comparison of the Mean Temperature at y/H=0.5

From figure 5.6, the mean temperature profiles at the mid-width length show an almost uniform distribution in the enclosure core. This shows that in the enclosure core region, there is very little activity as the mean temperature gradient is nearly uniform. Therefore, buoyancy force is minimal, so the fluid velocity is very small. This implies the kinetic energy needed for particle movement is little and by implication, the turbulence level, turbulent stresses and heat flux are less so there is very little activity.

In the core of the cavity, the predicted temperatures by both by PISO and SIMPLEC show a minimum value which is lower than the experimental temperature values. This is due to a trace of the cold draft emanating from the opposite wall, which according to measurements, should have had time to totally mix while crossing over along the floor. Again this shows insufficient mixing with the laminar core.

The PISO simulation yielded a temperature of 0.5 both at the center of the enclosure, and on the near wall profiles. The SIMPLEC simulation yielded a temperature of 0.4 both at the center of the enclosure, and on the near wall profiles. In the enclosure core region, there is very little activity; the mean temperature is nearly uniform. From x=0.7 to x=0.98, the temperature holds approximately constant, indicating that the fluid in the core area is nearly stagnant. The Steep temperature gradients appear, before they reach their minimum at Non-dimensional distance 0.15 m afar from the hot wall, where the bulk region begins. Here, the temperature is almost stationary and almost equal to the mean temperature.

All in all, temperature profiles change steeply near the isothermal hot and cold walls. Near to the vertical walls therefore, the temperature can be described by a linear law where temperatures drop linearly with distance. This region is called the inner layer of the boundary layer.

5.4.2 Turbulent Kinetic Energy profiles

These are profiles of the mean kinetic energy per unit mass, associated with root mean square fluctuating velocities (or eddies) in a turbulent flow. In this study, the turbulent kinetic energy is produced by shear, friction and buoyancy, transferred by turbulence energy cascade and dissipated by viscous forces (or molecular viscosity) at the Kolmogorov scales in the confluence. Figure 5.7 displays the measured turbulent kinetic energy on the mid-width plane and the corresponding profiles obtained with PISO and SIMPLEC numerical simulations.

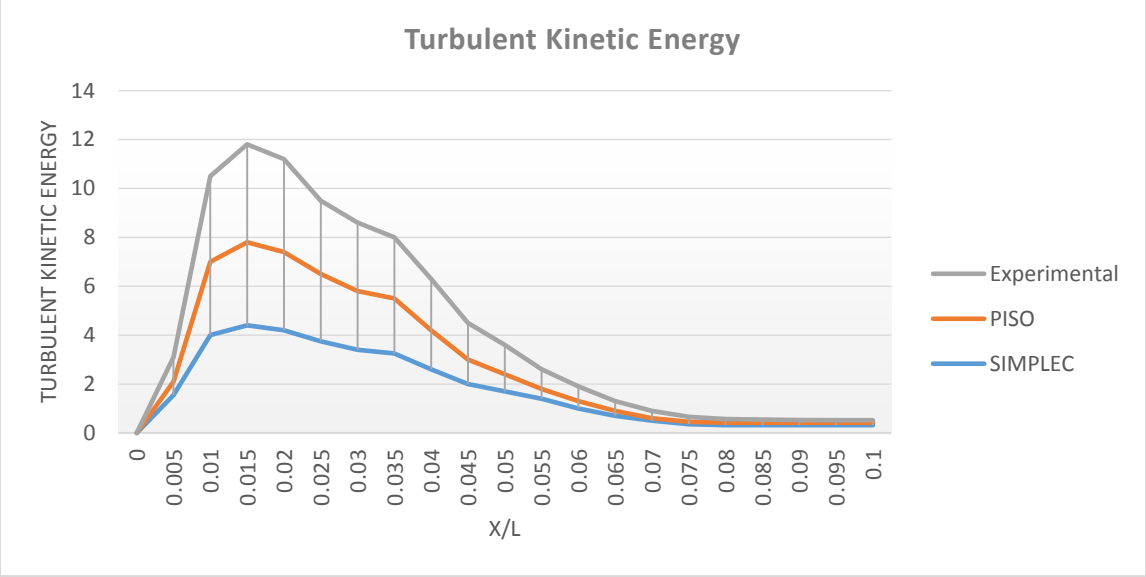

Fig. 5.7 Comparison of the Turbulent Kinetic Energy at y/H=0.5

Both the predicted and experimental profiles are asymmetrically distributed between the hot and cold walls and reach their maximum close to the hot wall given that turbulent kinetic energy varies with temperature gradients. The reason being shear stress, friction and buoyancy produces turbulence that causes an increase in fluctuating velocities near the hot surface. A comparison shows that the numerical prediction by both PISO and SIMPLEC induced lower turbulence kinetic energy than the experimental results. In the core, at the middle section, there is very little activity and the turbulence level is very small. The reason being there is low temperature gradient hence low buoyancy, less friction and shear stress that is why the turbulent kinetic energy falls to zero.

5.4.3 Local Nusselt Number

Figure 5.8 shows the heat transfer rate along the hot wall expressed in terms of the ratio of the convective to the conductive heat transfer across the boundary layer (local Nusselt number distribution). Using MADP by averaging the absolute values of the forecast errors, the SIMPLEC method over predicts Nusselt Number with a difference of 18 %,

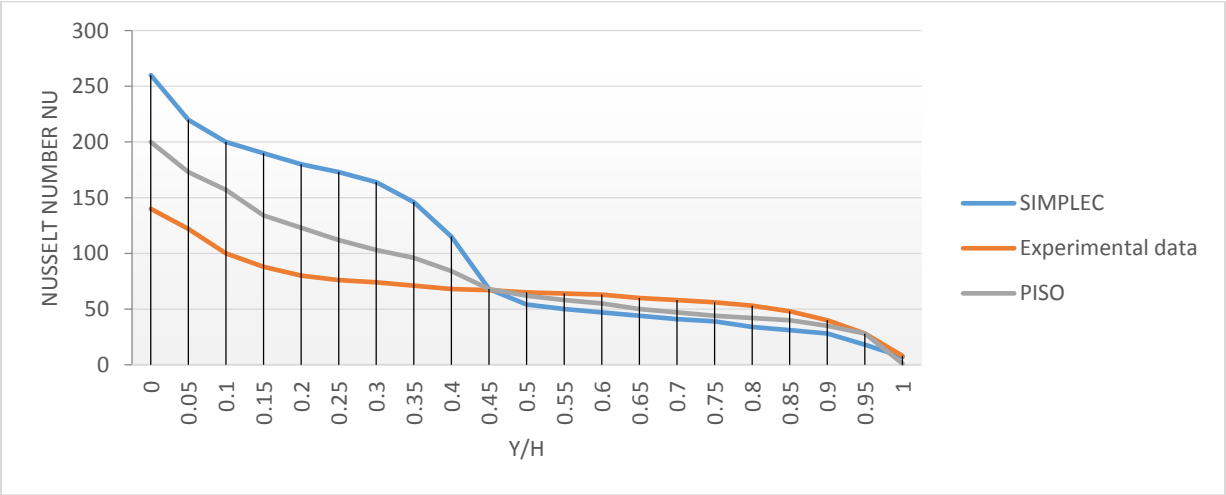

Fig. 5.8 Comparison of Local Nusselt Number along the Hot wall

on the lower half of the hot wall, then under-predicts it but weakly compared with the measured data on the upper part of the wall.

The PISO method over predicts Nusselt Number with a difference of 9 %, on the lower half of the wall, then under-predicts it but somewhat less strongly compared with the experimental data on the upper part of the wall. The over prediction of the Nusselt number in the initial parts of the hot surface may be related to the local minimum of temperature and residual cold draft coming over from the cold surface hence insufficient mixing between the laminar and turbulent core, which induces the sharper temperature gradient as seen and increases the convective heat transfer coefficient as seen in figure 5.6.

5.4.4 Mean Vertical Velocity

Figure 5.9 shows the profiles for rate of change of vertical displacement of the fluid particles with time. The profiles are asymmetrical and with a peak near the heated surface.

The rise is caused by the fluid gaining kinetic energy due to higher temperature gradient at the heated surface. The fall is due to (a) local minimum temperature (b) the cold drift coming over from cold wall. The two factors diminish the temperature gradient and make the kinetic energy in the fluid to dissipate.

As seen in figure 5.9, there is good agreement between the experimental data and the predicted data in terms of the mean velocity. The peak value of velocity is particularly well captured by

both PISO and SIMPLEC methods. In the enclosure core region, there is very little activity and hence the fluid velocity is very small.

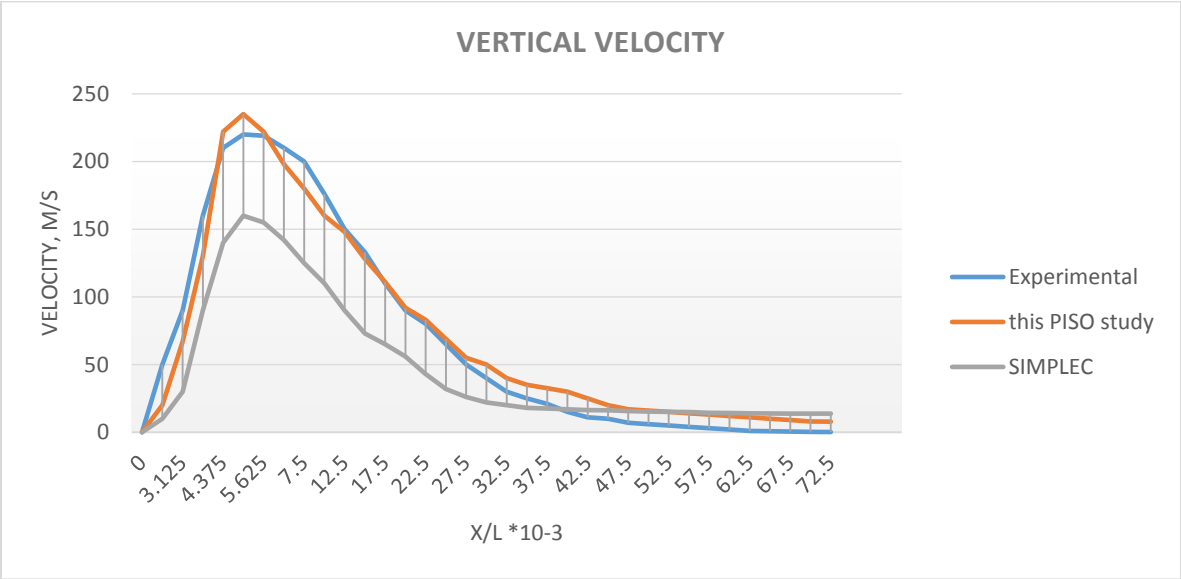

Fig. 5.9 Comparison of the vertical velocity

5.4.5 Mean Horizontal Velocity

Figure 5.10 shows the profiles of the rate of change of horizontal displacement of the fluid with time.

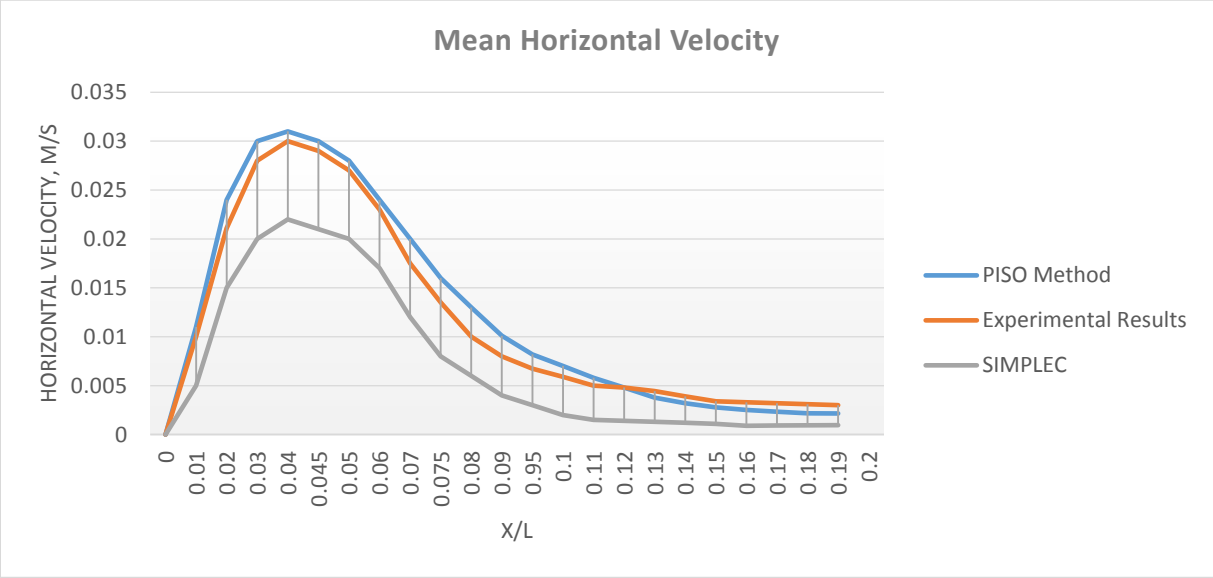

Fig. 5.10 Comparison of the Horizontal velocity

The rise of velocities near the heated surface of the cavity is as a result of fluid gaining kinetic energy from the heated wall causes an increased convective heat transfer coefficient, while the drop of velocities after 0.04 from the hot wall is as a result of;

(a) Local minimum temperature

(b) The cold drift coming over from the opposite cold wall.

Resultantly, factors (a) and (b) above make the energy in the fluid dissipate.

All in all, there is good agreement between the experimental data and the predicted data in terms of the mean horizontal velocity, as shown in figure 5.10.

5.5 Velocity Vectors by PISO algorithm

Figure 5.11 below shows the predicted velocity vectors at X=0 i.e., on the hot wall at a Rayleigh number of 1.58×10^9. The figure shows the typical patterns observed in natural convection flows, on the thermally active walls.

At the hot wall as seen from the velocity vectors in figure 5.11, air motion is driven by buoyancy resulting from density gradients produced by internal body forces. The density gradients can arise from mass concentration and/or temperature gradients in air where a heated surface is submerged in cooler air.

The cooler air will absorb kinetic energy in the form of the intense heat generated from the heated surface and become less dense. Buoyancy effects due to body forces which are thermally generated will cause the heated air to rise. At this point, the surrounding, cooler air will move in to take its place.

The cooler air is then heated and the process continues resulting to a clockwise convection current that continuously transfers away energy from the heated surface. A current of cold denser air from the cold surface flows in to take up its place. Therefore the direction of velocity vectors are an evidence of upward convectional currents at the isothermal hot wall.

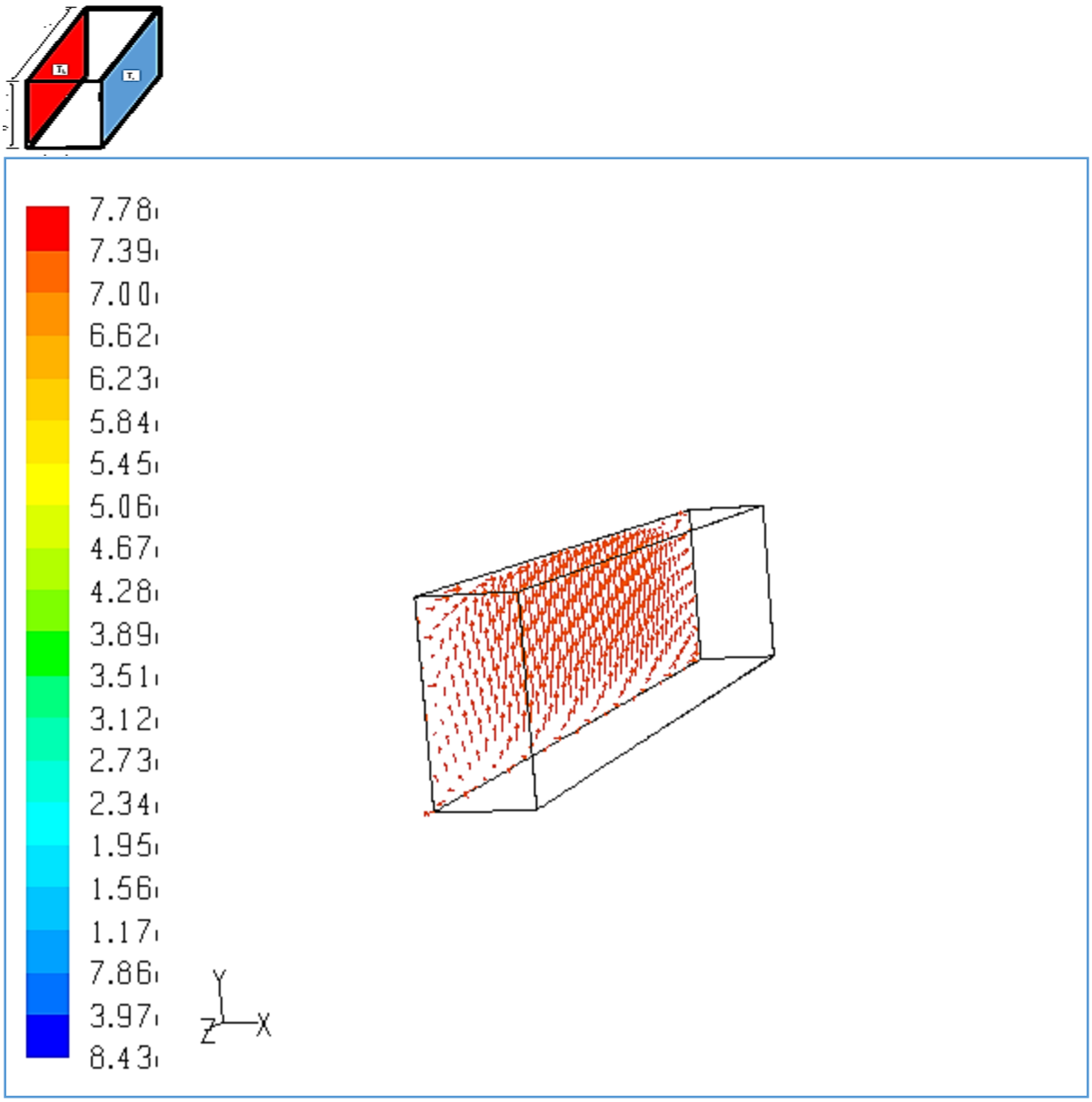

Fig. 5.11 Velocity vectors at X=0

Figure 5.12, shows velocity vectors at X=0.1, near the hot surface. The cold denser air, next to the rising hot air, flows in to take up the space created out of the heated air rising. The air next to the hot wall is always exposed to shear stress, friction and buoyancy, which cause fluctuating mean velocities, turbulent kinetic energy and consequently turbulence.

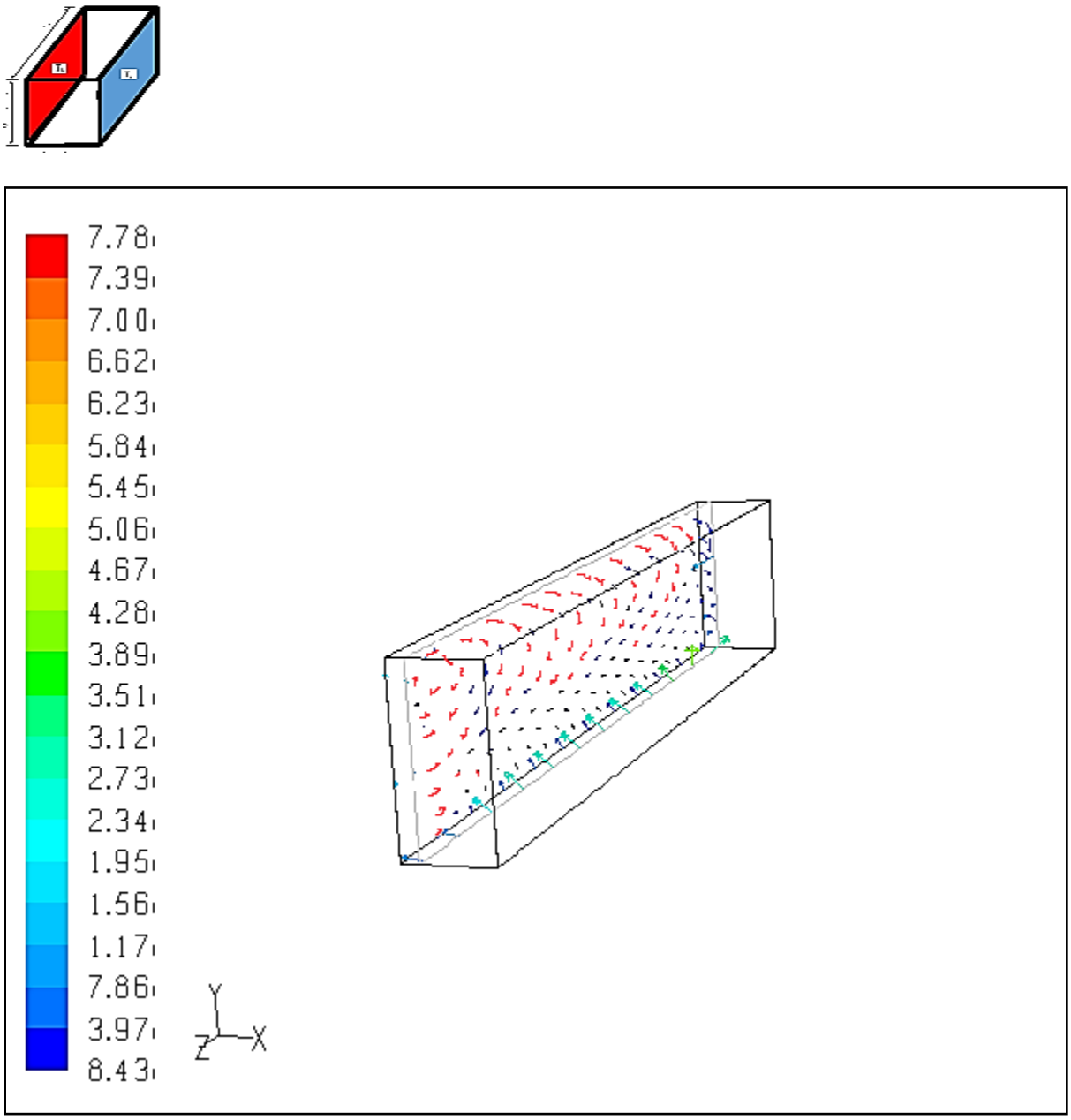

Fig. 5.12 Velocity vectors at X= 0.1

In summary, the shaper temperature gradients near the heated surface, as in figures 5.11 and 5.12, create buoyancy force and surface forces, as a result of shear stresses and friction drag, to be exerted on air which cause a turbulence, as shown in figure 5.7, that make flow velocity to increase yielding a stronger convective heat transfer across the boundary layer. For this reason Nusselt number is high and cold denser air from the cold surface flows in to take up created

space. This creates a clockwise convectional currents near the hot surface. Resultantly, as shown in figure 5.13, there will be a strong incoming cold convectional current of air from the cold isothermal wall via the horizontal adiabatic floor of the enclosure.

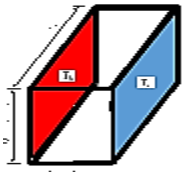

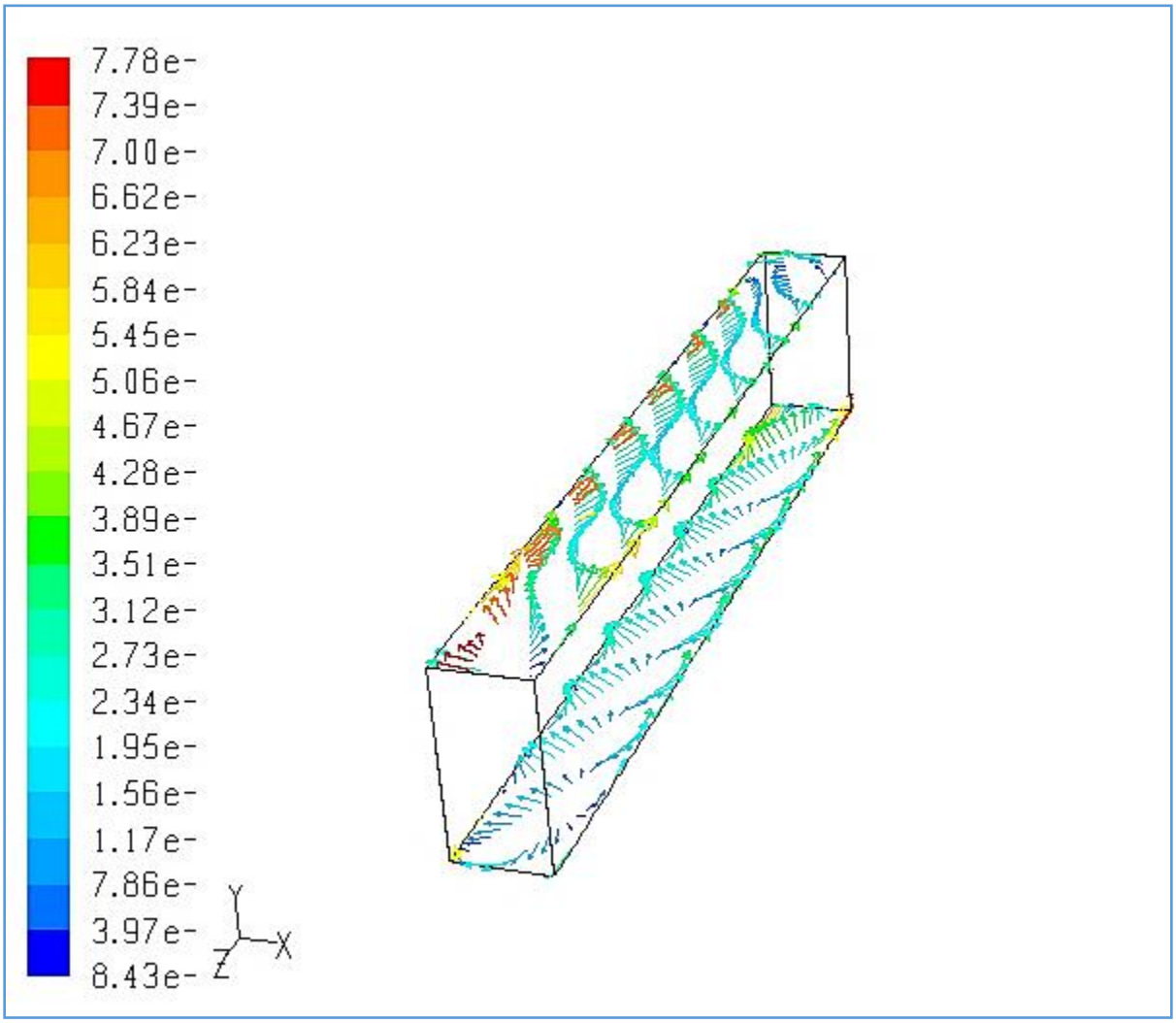

Fig. 5.13 Vector plots at Y=0 and Y=1

The flow predictions from the velocity vector on floor and roof of the enclosure, as shown in Figure 5.13, reveal that the flow tends to form 3-D small rolls along these horizontal adiabatic walls. This verifies the presence of a strong 3-D vortex generation mechanism called vortex stretching that transfers energy and vorticity to increasingly smaller scales.

The rolls are a product diffusivity due to thermally-generated counter-rotating cells and are a sign of nonlinearity, rotationality and 3-D turbulence:- The competition between the surface tension and gravity given that the denser colder air far from the heater is accelerated by light hot air near the heater due to buoyancy generated convection currents. This causes small pertubations in the flow which results to angular momentum. As a result the small perturbations grow in time and instability is triggered.

This implies that that the presence of non-linear turbulent correlations, like the Reynolds stress and the heat flux, in the flow causes the Reynolds, Reyleigh number and the inverse Richardson’s number to exceed their critical value, make the flow to exceeds stability criteria, becomes spontaneously unstable and then reach chaotic state which results to formation of eddies in the motion of fluid particles that have non-zero vorticity and which occur in all directions and depict turbulence.

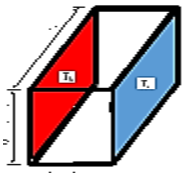

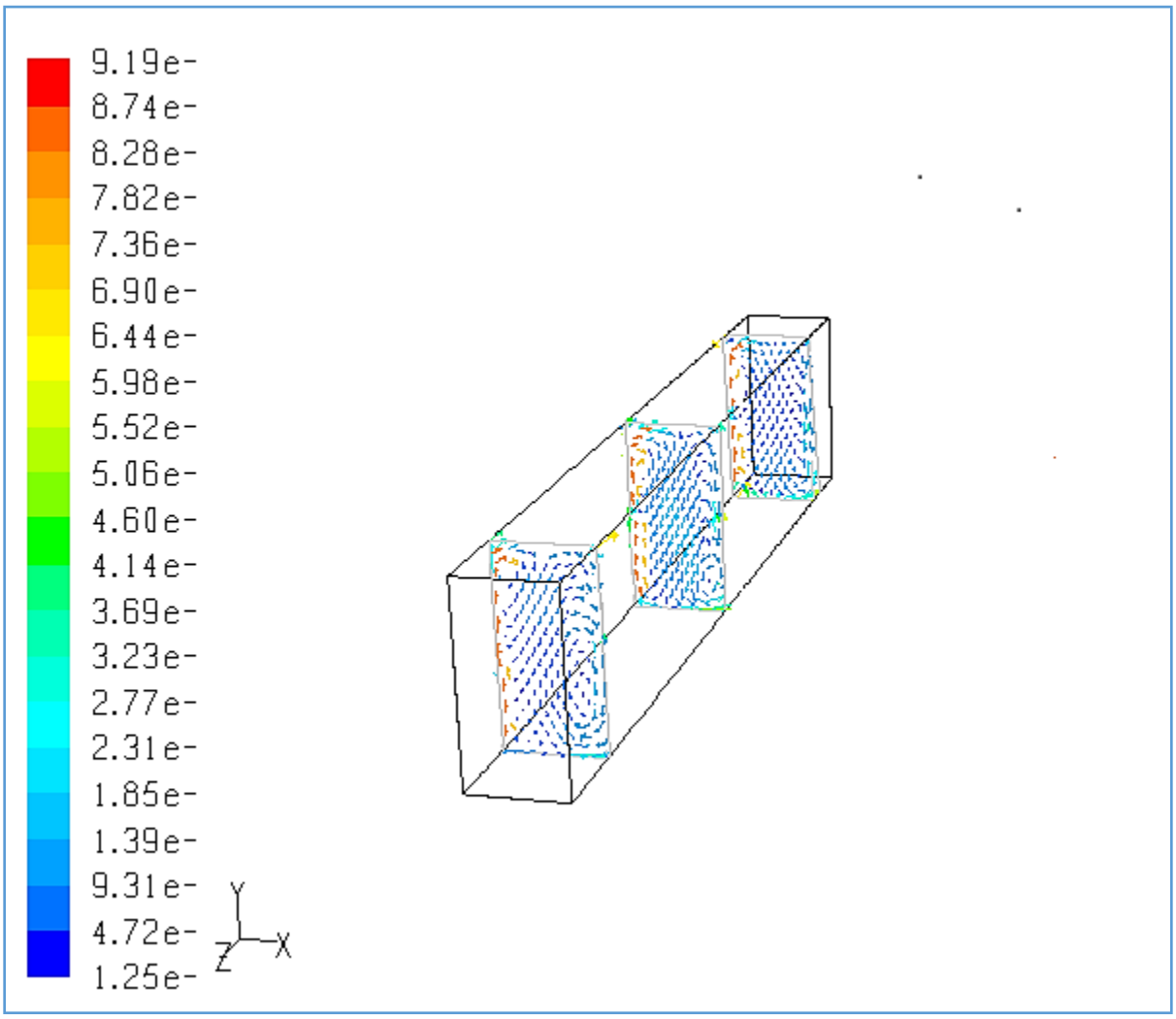

Fig. 5.14 Velocity vectors at Z=0.1, Z=0.5 and Z=0.9

The reason for these eddies is best explained using figure 5.14 and figure 5.15. The strong downwards flow at the cold surface and strong upward flow at the hot surface (figure 5.14)

forms two rotating streams at the thermally active walls. The two developed boundary layers move towards each other and collide at the confluence of the cavity.

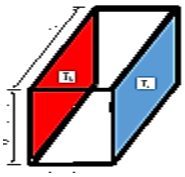

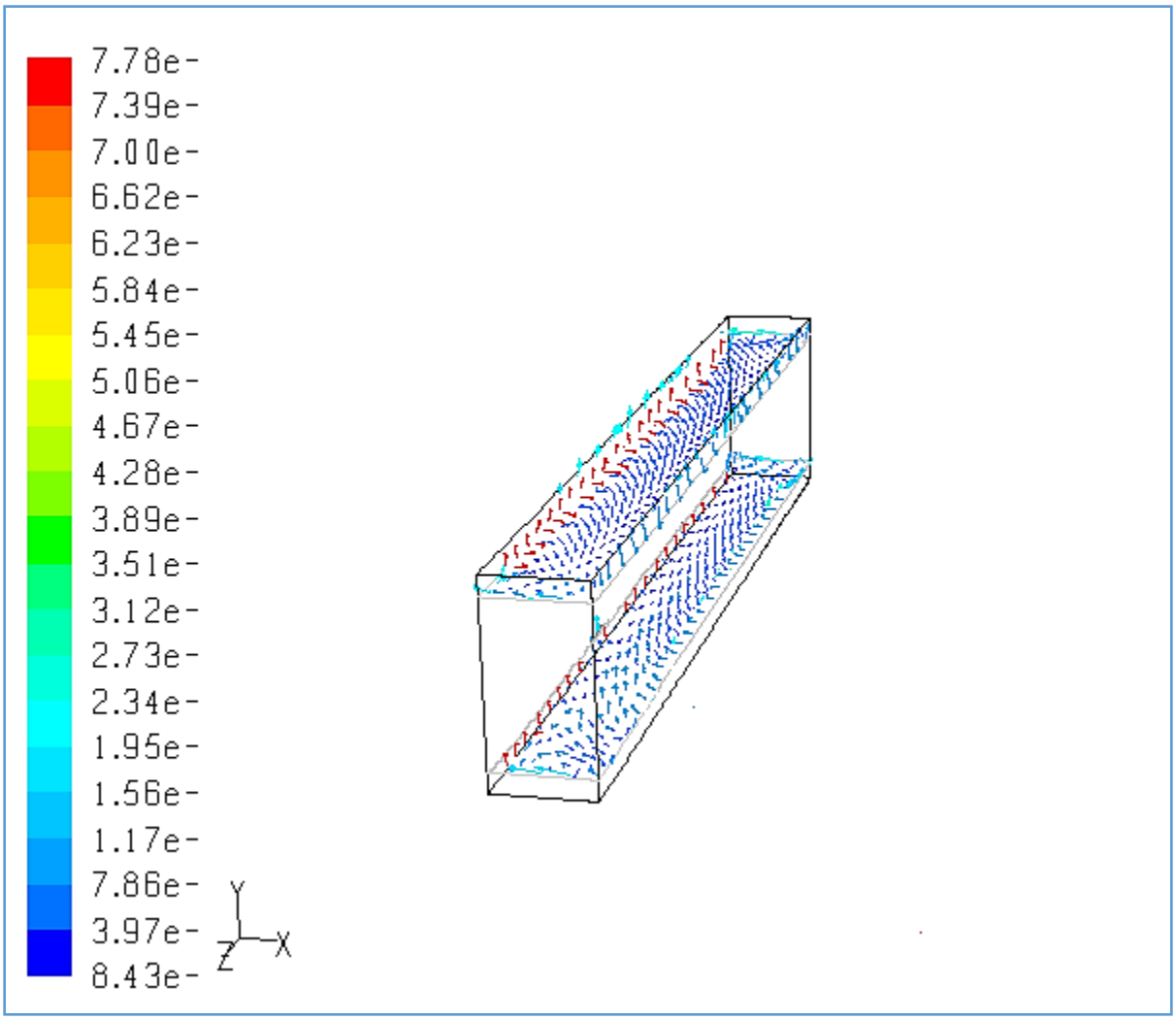

Fig. 5.15 Velocity vectors at Y=0.1 and Y=0.9

Mixing process takes place in the region of confluence leading to the exchange of mass, momentum and heat between the two fluid layers. This process transfers heat energy from the

hot to the cold regions of the enclosure and causes increased rates of mass and momentum transfer in the flow and enhanced homogenization of the air particles.

Given also that the roof and the floor are the platforms of collision, the collision of the two opposing convectional currents causes randomness of air motion which results to turbulence manifested inform of eddies that are prominent at the roof of the enclosure as in figure 5.13.

A horizontal view of the velocity vector plots in the x – z plane, perpendicular to the hot and cold surface, as in figure 5.15, depict a very strong flow from the hot surface towards the cold surface of the enclosure. An equally strong stream appears to be flowing from the window towards the heater.

The two streams collide at the confluence region of the heater and the window as shown in the Figure 5.15. After collision

(i) Diffusivity occurs

(ii) Ricocheting of the two streams occur whereby the hot buoyant stream is deflected back horizontally and the cold stream is deflected back too towards the cold surface after collision.

At high Reynolds number, a strong convective motion develops and heat is transferred from the hot surface to other regions. The area where friction slows down the air flow is called the boundary layer. Air flowing in the boundary layer travels in the state of turbulent flow as is the case with the roof of the enclosure in figure 5.13.

This boundary layer is important because it is the source of skin friction drag, and can actually decreases pressure drag, a force that would pull kinetic energy out of the air.

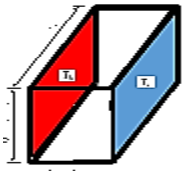

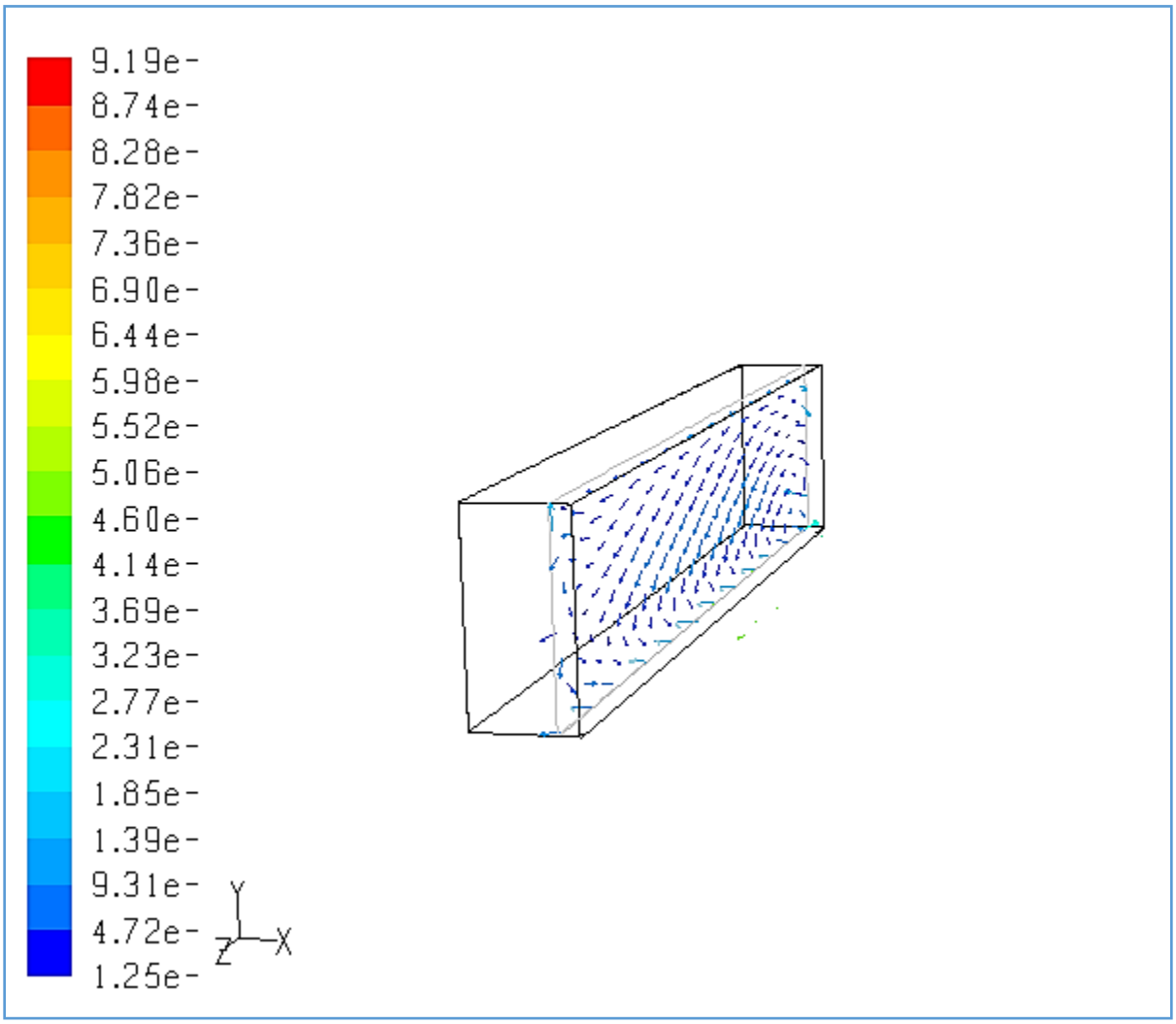

Fig. 5.16 Velocity vectors at X=0.9

Figure 5.16 shows velocity vectors at X=0.9. The velocity of the descending air is strongest near the window given the length of the vectors.

Buoyancy effects that are thermally generated will cause the cooled air to flow downwards due to density gradients arising from temperature gradients in the air due to the cold surface. The conventional currents near the cold surface are downwards and clockwise.

Consider the velocity vectors at the confluence of the two thermally active surfaces as shown in figure 5.17 overleaf.

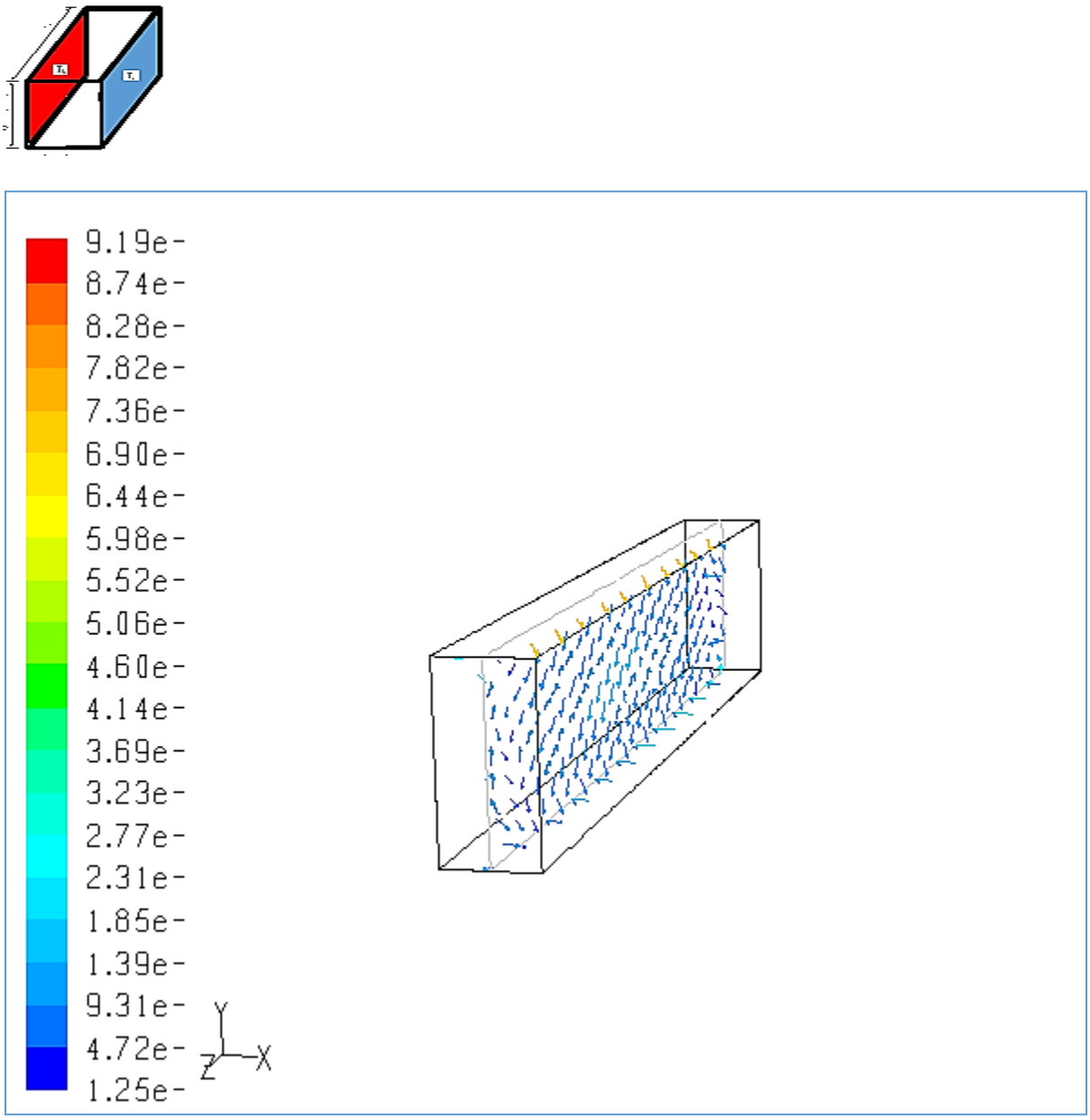

Fig. 5.17 Velocity vectors at X=0.5

The structure of the flow in the plane at X = 0.5 shows the confluence where two circular motions in different directions are set up –one in upward direction while the other in a downward direction.

Firstly, there is diffusivity of two streams that results to enhanced homogenization and increased rates of mass, momentum and energy transfer of heat from the hot to the cold stream as shown by the upward and downward motion of vectors in figure 5.17. This is due to readily available supply of energy through energy cascade mechanism that tends to accelerate homogenization of fluid mixtures.

Secondly, the collision causes randomness of flow (or mass transfer) due to fluctuating mean velocities resulting to turbulent kinetic energy given that;

i. Eddies on the roof of cavity
ii. Increased rates of mass, velocity and momentum transfer.

This makes the flow to become spontaneously unstable and reach chaotic state which results to fluctuations in fluid particles to have non-zero vorticity which depicts turbulence.

Thirdly, the profiles coupled with those of figure 5.7, depict dissipation in the flow whereby vortex stretching mechanism transfers energy and vorticity to increasingly smaller scales until the gradients become so large that they are smeared out by molecular viscosity at the confluence region. This explains why in figure 5.9, the profiles are asymmetrical and with zero value of velocity at the enclosure core.

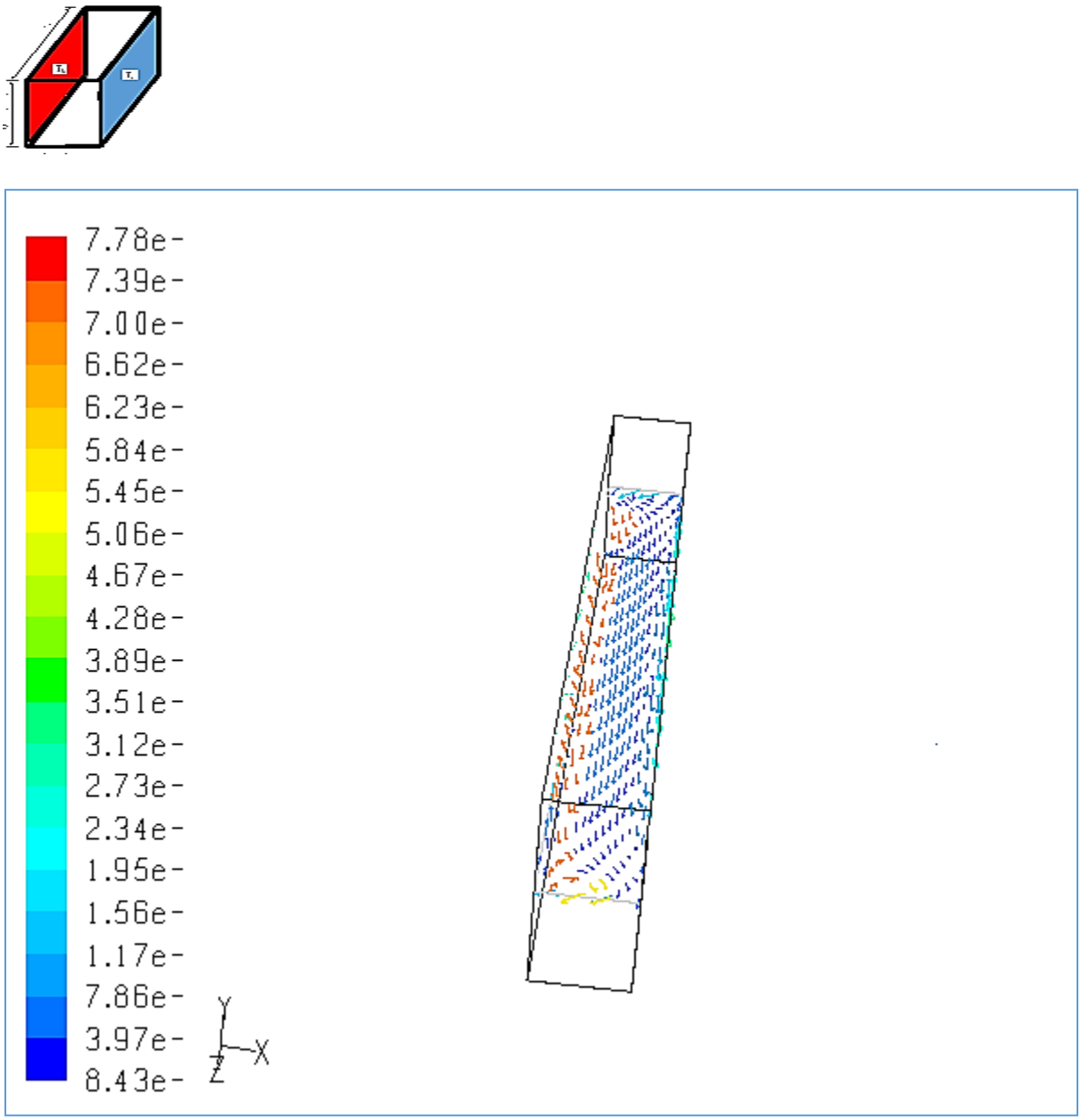

Fig. 5.18 Velocity vectors at Y=0.5

Figure 5.18, showing the velocity vectors at Y=0.5, depicts that at the mid-horizontal plane, the particles along the hot surface are upward moving due to thermally generated buoyancy effects. There is also evidence of mixing and exchange of heat energy between hot and cold particles through the presence of both red-colored and blue colored vector plots at the confluence, a process that transfers heat energy from the hot to the cold regions of the enclosure.

The mixing of the two streams during their collision results to making the confluence warm. Different temperature conditions at the thermally active walls resulted in colliding boundary condition whereby two formed boundary layers collide at the confluence of the cavity. After collision

i) Mixing process takes place in this region leading to the exchange of heat between the two fluid layers. This process transfers heat energy from the hot to the cold regions of the enclosure.

ii) The two layers curve to form two streams. One stream moves towards the hot surface via the floor while the other stream flows towards the cold surface of the enclosure via the roof.

iii) The right cell is driven by the cold window whereas the left cell is driven by the heater. Both the cold right cell and the hot left cell rotate in a clockwise direction.

iv) The turbulent natural convection does play an important role in the variation of temperature in an enclosure. At the center of the room, there is relatively warm region. This comes as a result of the hot air rising up from the heater mixing up the cold fluid from the window.

v) The collision of the cold and hot stream at the confluence causes the, Reynolds, Reyleigh number and the inverse Richardson’s number to exceed their critical value, becoming spontaneously unstable and then reaching chaotic state which results to fluctuations in fluid particles to have non-zero vorticity as shown in figure 5.13 which depicts turbulence.

5.6 Velocity Vector Profiles by SIMPLEC

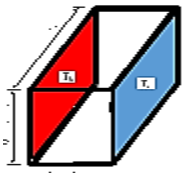

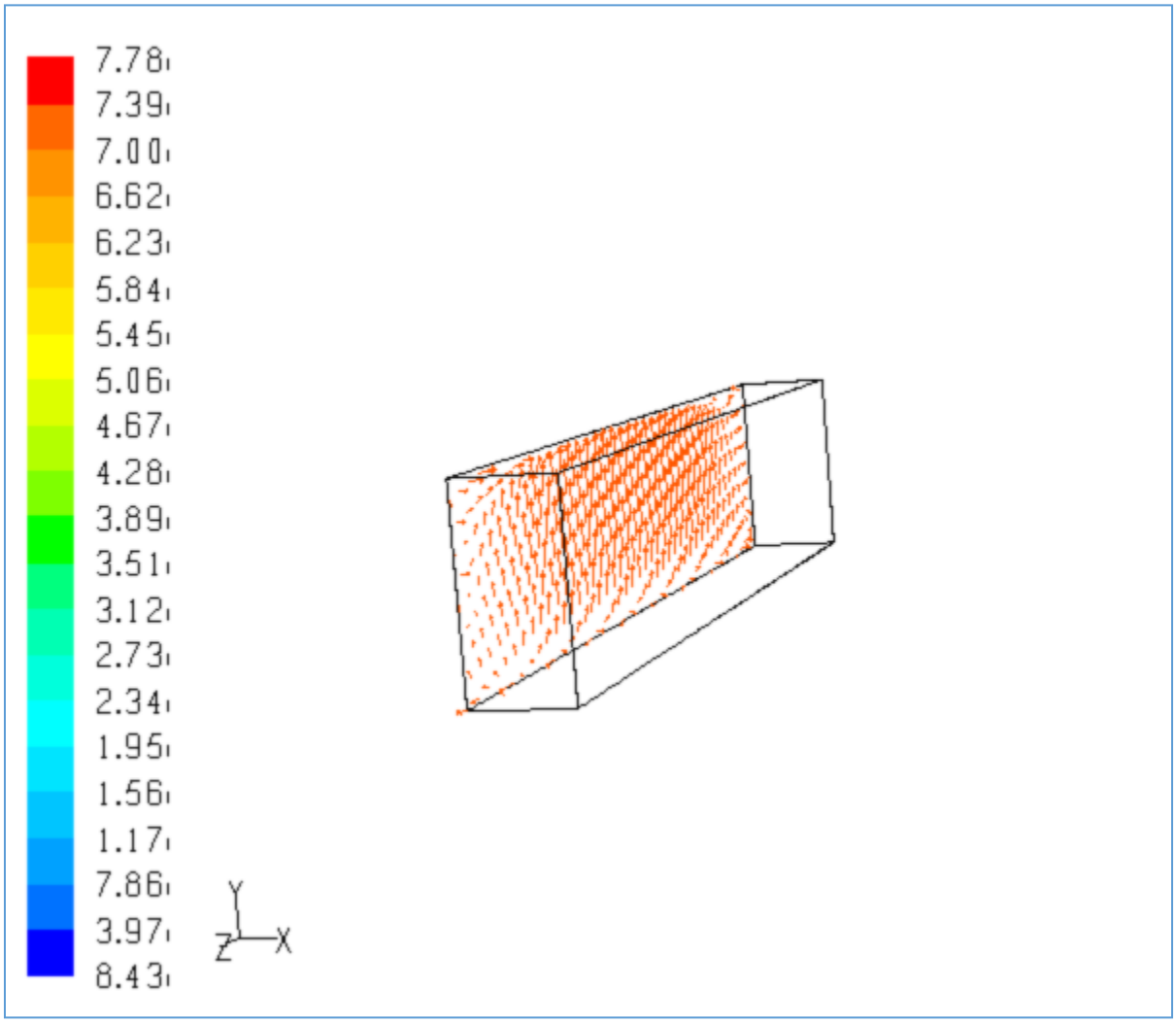

Fig. 5.19 Velocity vectors at X=0

Just like with the PISO method, the intense heat generated by the hot wall accelerates the air as it flows around the wall. Hot air is seen flowing upwards from the isothermal hot wall, and then turns to flow towards the cold wall via the ceiling of the cavity. Therefore buoyancy effects that

are thermally generated results to density gradients in the fluid next to the wall and cause the heated fluid to rise as is evident with the velocity vectors.

The air particles rise because of the cold drift of denser fluid particles from the cold surface that flows in to take up the created space. So the internal energy due to heating on the hot surface becomes the source that sustains natural convection transport mechanism in the 3-D rectangular cavity.

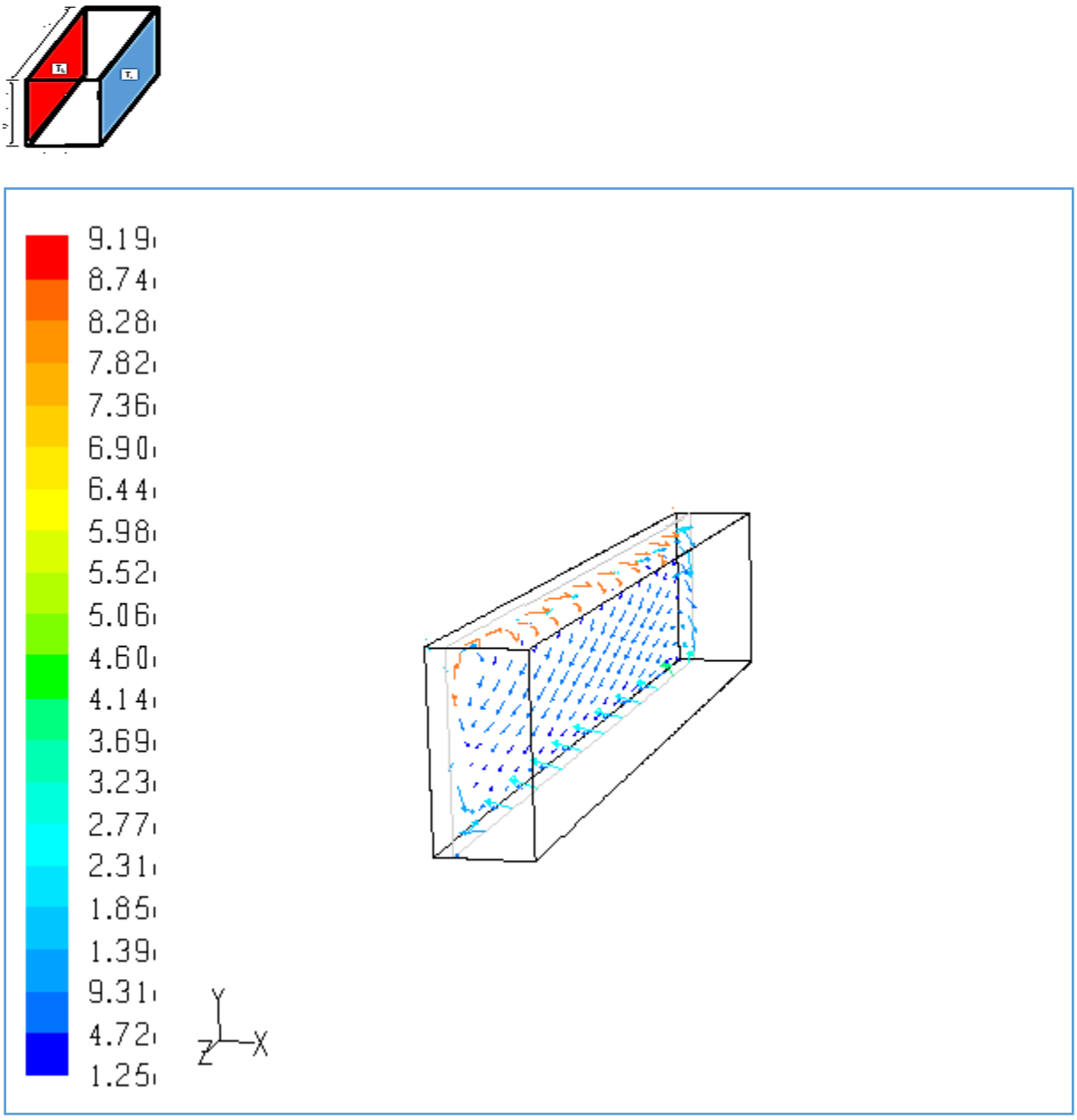

Fig. 5.20 Velocity vectors at X=0.1

As shown in figure 5.20, the driving force for the fluid motion is buoyancy, which is the gravity field acting on density difference. Buoyant force causes denser parts of the fluid to move downwards and less dense parts to move upwards. Hot air is seen flowing upwards from the isothermal hot wall, and then turns to flow towards the cold wall via the ceiling of the cavity.

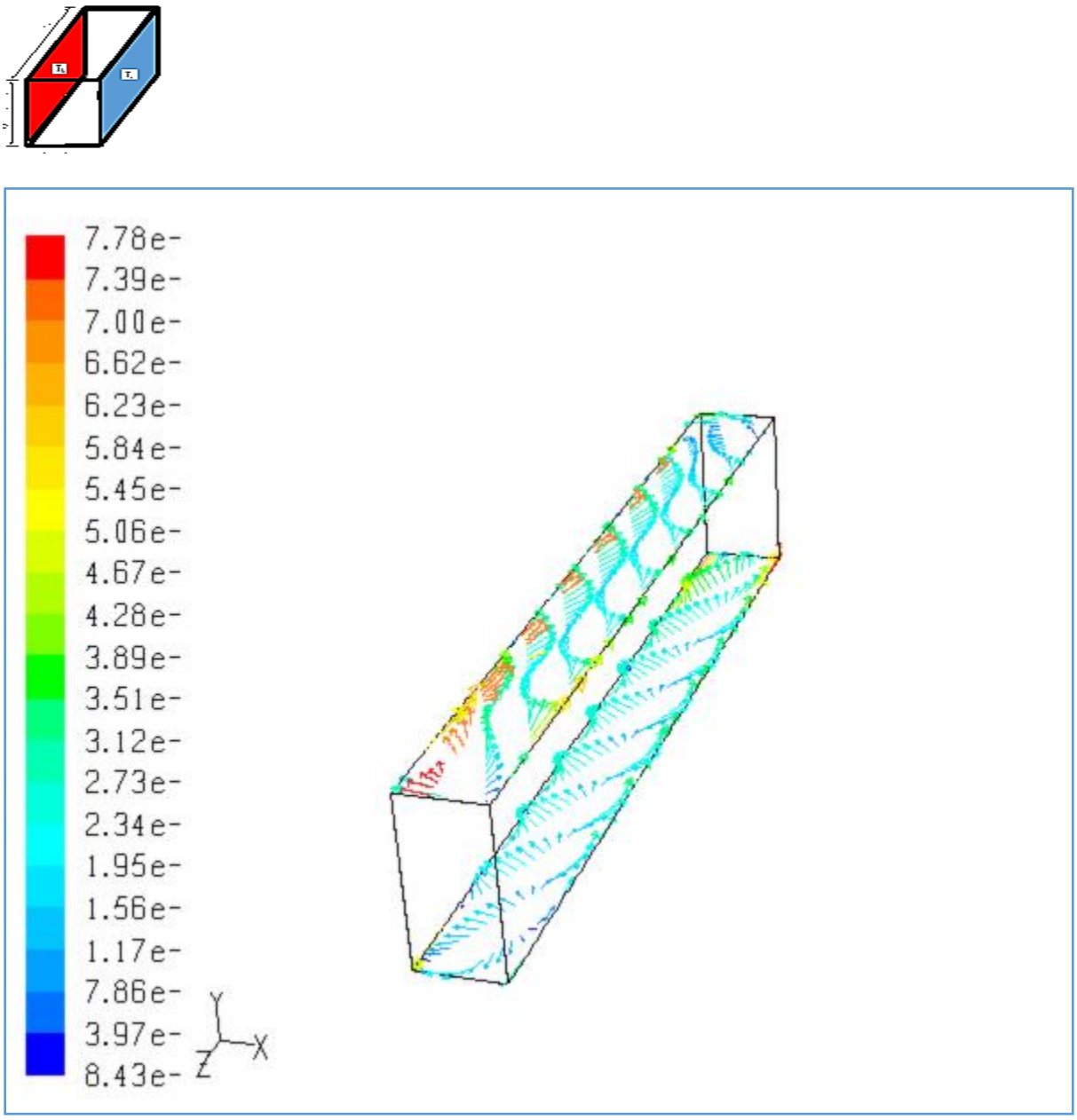

Fig. 5.21 Vector plots at Y=0 and Y=1

Analogous to PISO profiles on the same walls, in SIMPLEC the flow tends to form small rolls along these horizontal adiabatic walls as in figure 5.21. These rolls are a product of turbulence due to the collision of counter rotating streams at the confluence. Then, the flow develops non-zero vorticity and a strong vortex generating mechanism in the boundary layer. That is why this

fluid is rotational and three-dimensional and these re-circulation structures (eddies) are an evidence of turbulent-flow.

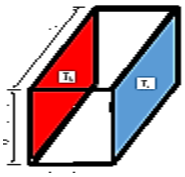

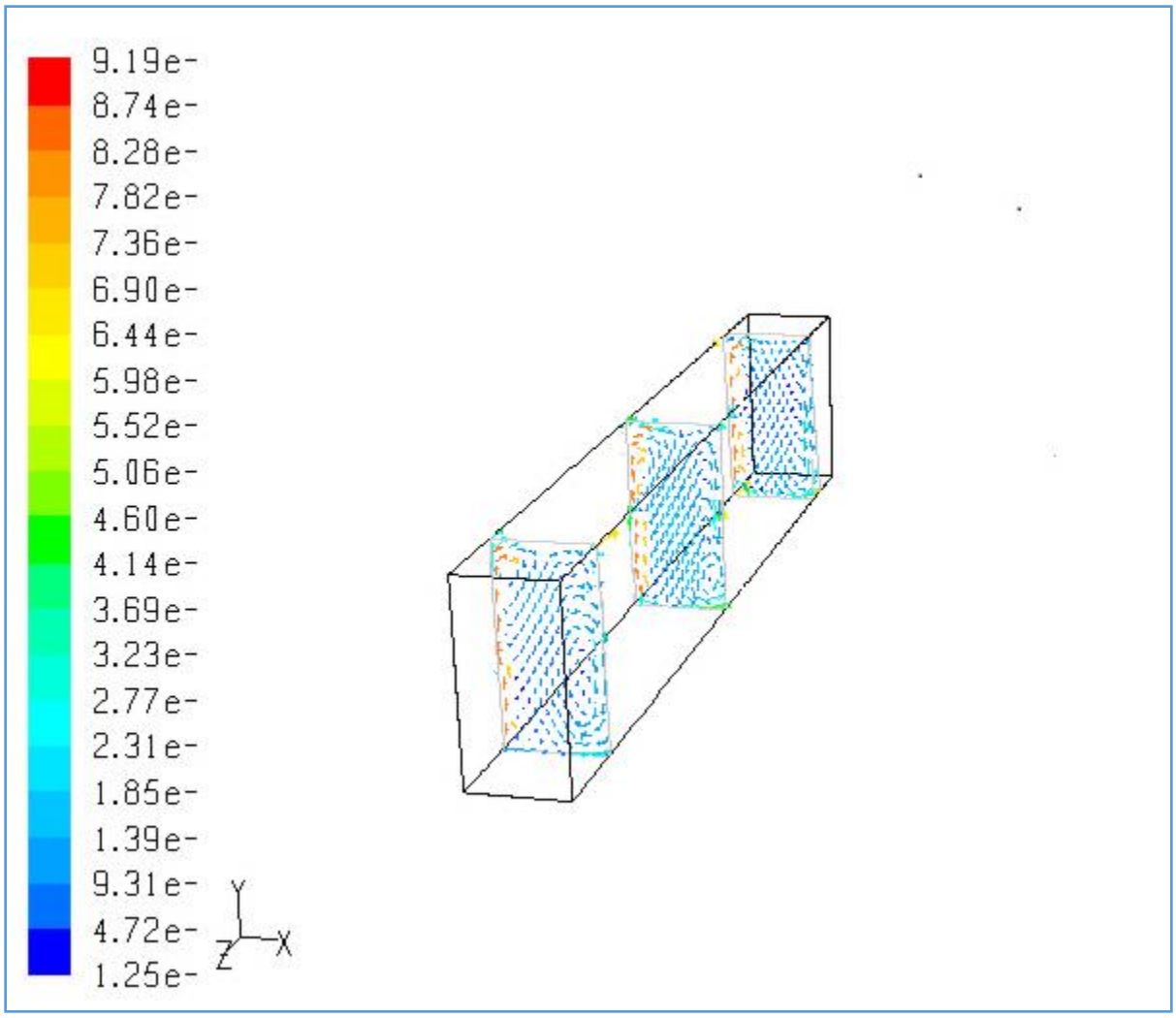

Fig. 5.22 Velocity vectors at Z=0.1, Z=0.5 and Z=0.9

figure 5.22 shows two developed boundary layers from the opposite- thermally active walls, colliding at the confluence region of the heater and the window. Mixing process takes place in the region of confluence leading to the exchange of heat between the two fluid layers. This

process is called diffusivity and it transfers heat energy from the hot to the cold regions of the enclosure,

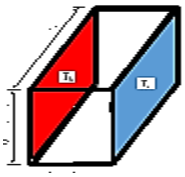

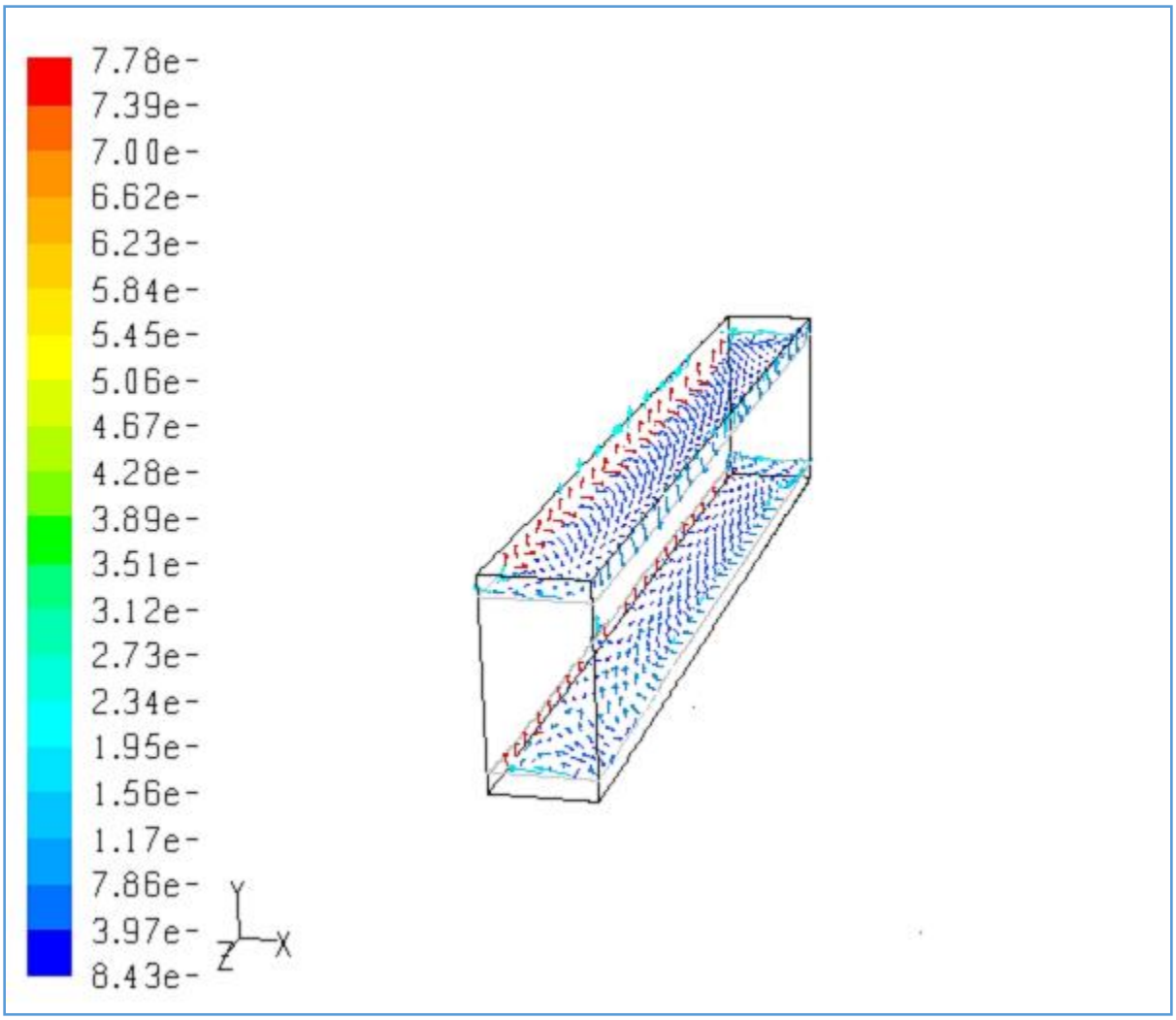

Fig. 5.23 Velocity vectors at Y=0.1 and Y=0.9

Further evidence of diffusivity is depicted in figure 5.23. Density differences due to differences in temperature causes a very strong flow from the hot surface towards the cold surface of the enclosure. On the floor, an equally strong stream due to buoyancy induced density gradients is

flowing from the window towards the heater. This implies the convectional currents are clockwise.

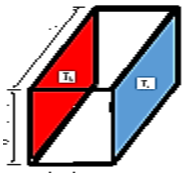

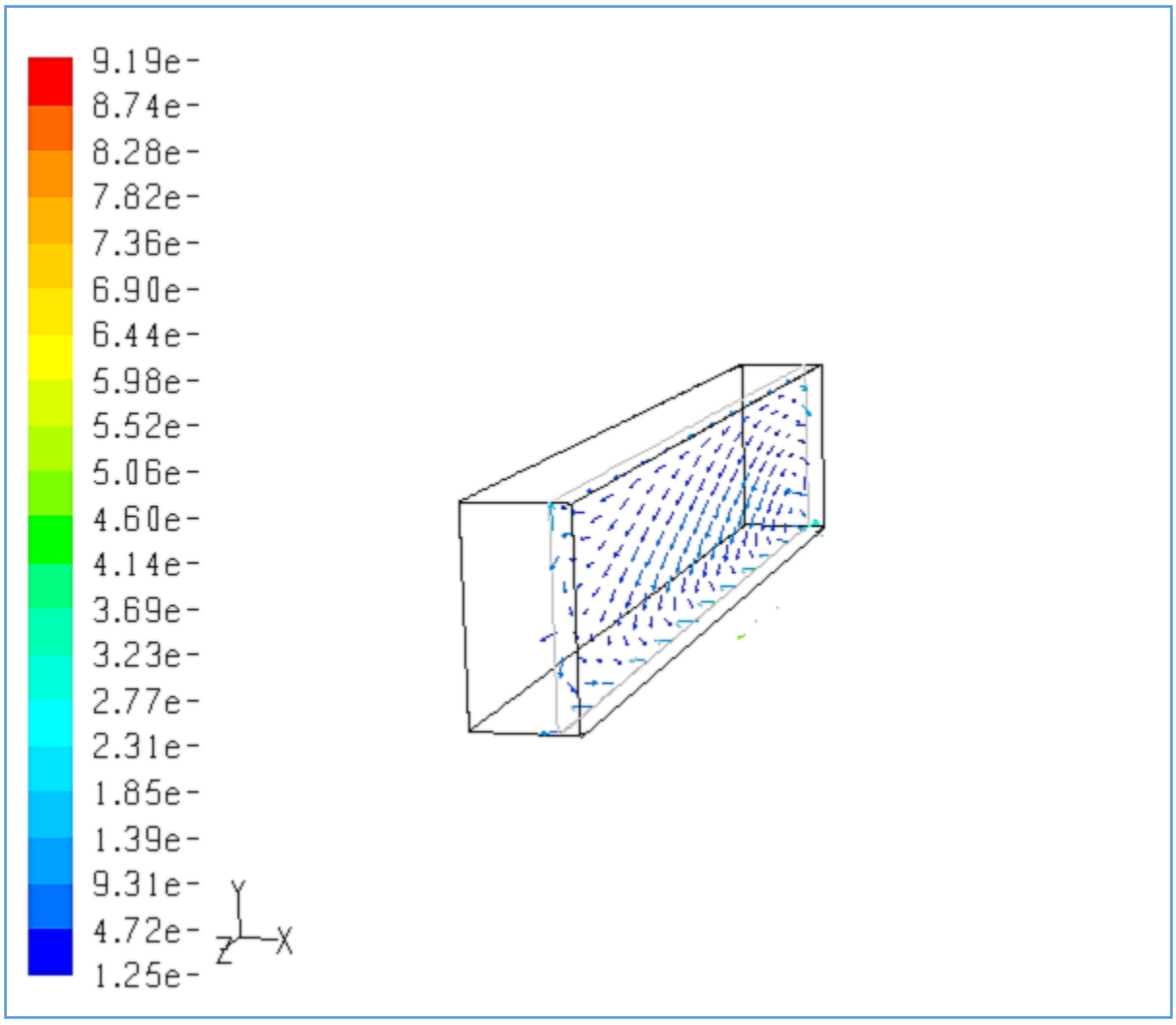

Fig. 5.24 Velocity vectors at X=0.9

Figure 5.24 shows velocity vectors at X=0.9 Just like is with PISO, the conventional currents in SIMPLEC near the cold surface are downwards and clockwise. The density gradients arise from

temperature gradients in the fluid. Buoyancy effects which are thermally generated will cause the cooled fluid to flow downwards. This sets up a cold convectional current near the cold surface that will turn clock-wise to flow towards the heater due to thermally generated density gradient.

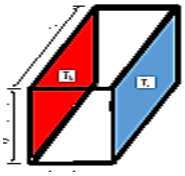

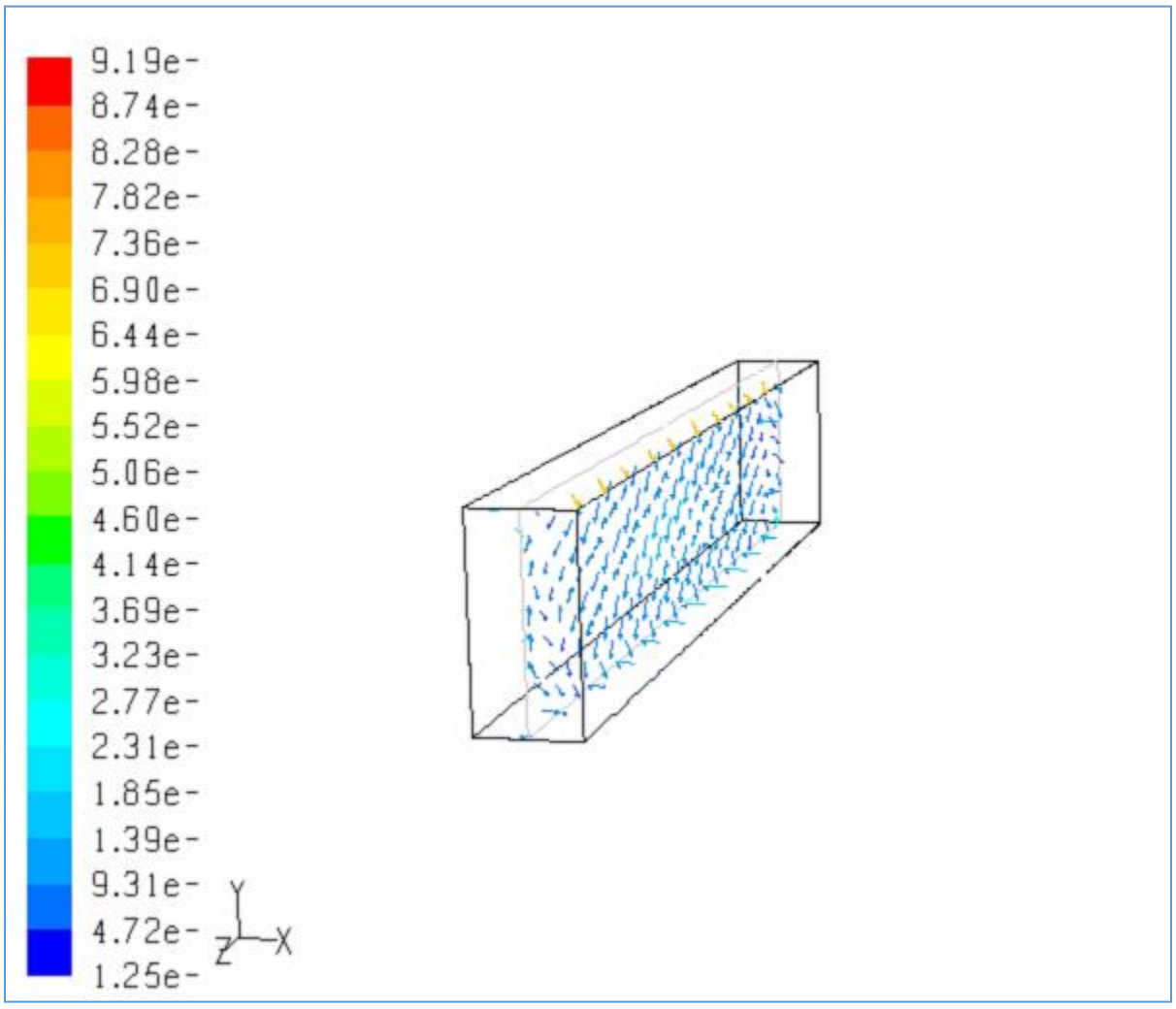

Fig. 5.25 Velocity vectors at X=0.5

Figure 5.25 shows velocity vectors at X=0.5. At the confluence of the heater and window. Two streams collide in the region between the window and the heater. The convectional currents due

to buoyancy causes homogenization of fluid particles. Mixing process takes place in this region leads to the exchange of momentum and heat between the hot and cold streams. This is shown by the upward and downward motion of vectors in figure 5.25.

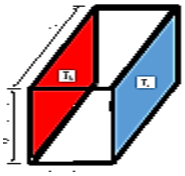

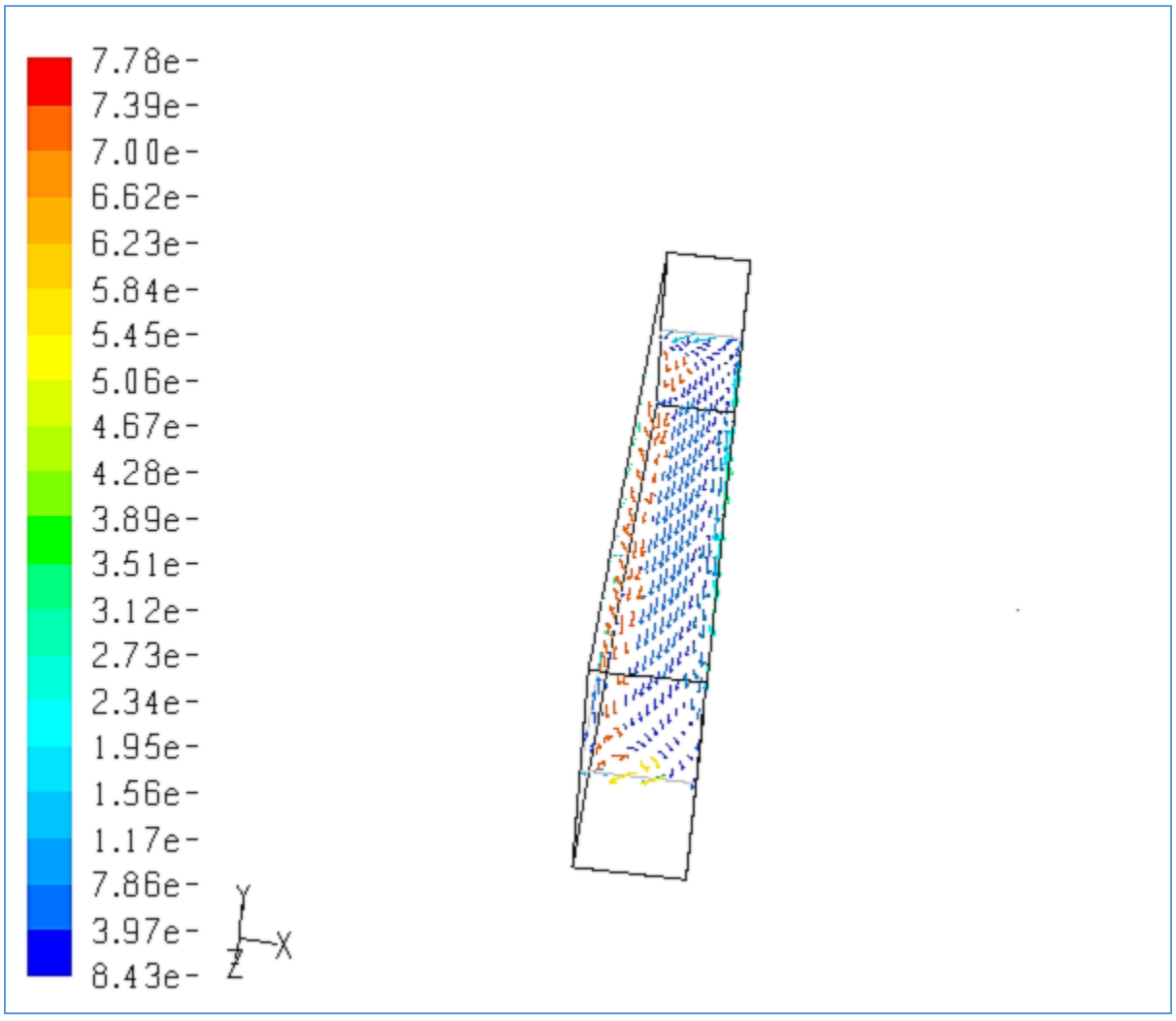

Fig. 5.26 Velocity vectors at Y=0.5

Figure 5.26 shows the velocity vectors at Y=0.5. The profiles depict that at the mid-horizontal plane, the particles along the hot surface are upward moving due to thermally generated buoyancy effects. There is also evidence of mixing and exchange of heat between hot and cold particles through the presence of both red-colored and blue colored vector plots at the confluence, a process that transfers heat energy from the hot to the cold regions of the enclosure.

Diffusivity as a characteristic of turbulence is therefore evident where the randomness of the flow:-

i. Causes rapid transport of momentum, mass and energy in the cavity
ii. There is enhanced homogenization of fluid particle

Most of the kinetic energy of this turbulent is produced by shear, friction and buoyancy and is contained in the large flow structures at the roof and floor as in figure 5.21. This energy is transferred by turbulence energy cascade and is then dissipated by viscous forces at the Kolmogorov scales when the cold and hot streams collide at the confluence as in figure 5.25 and figure 5.26 above.

Figure 5.21 brings out the aspect of rotationality in turbulence flow since the velocity vectors at the roof show non-zero vorticity. It is evident the strong three-dimensional vortex generation mechanism that causes the hierarchy of eddies. Evidently, vortex stretching mechanism transfers energy and vorticity to increasingly smaller scales before they are smears out by dissipation at the Kolomarov scales in the confluence by molecular viscosity.

5.7 Static Pressure Profiles by PISO Method

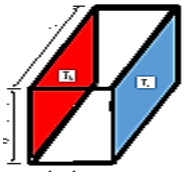

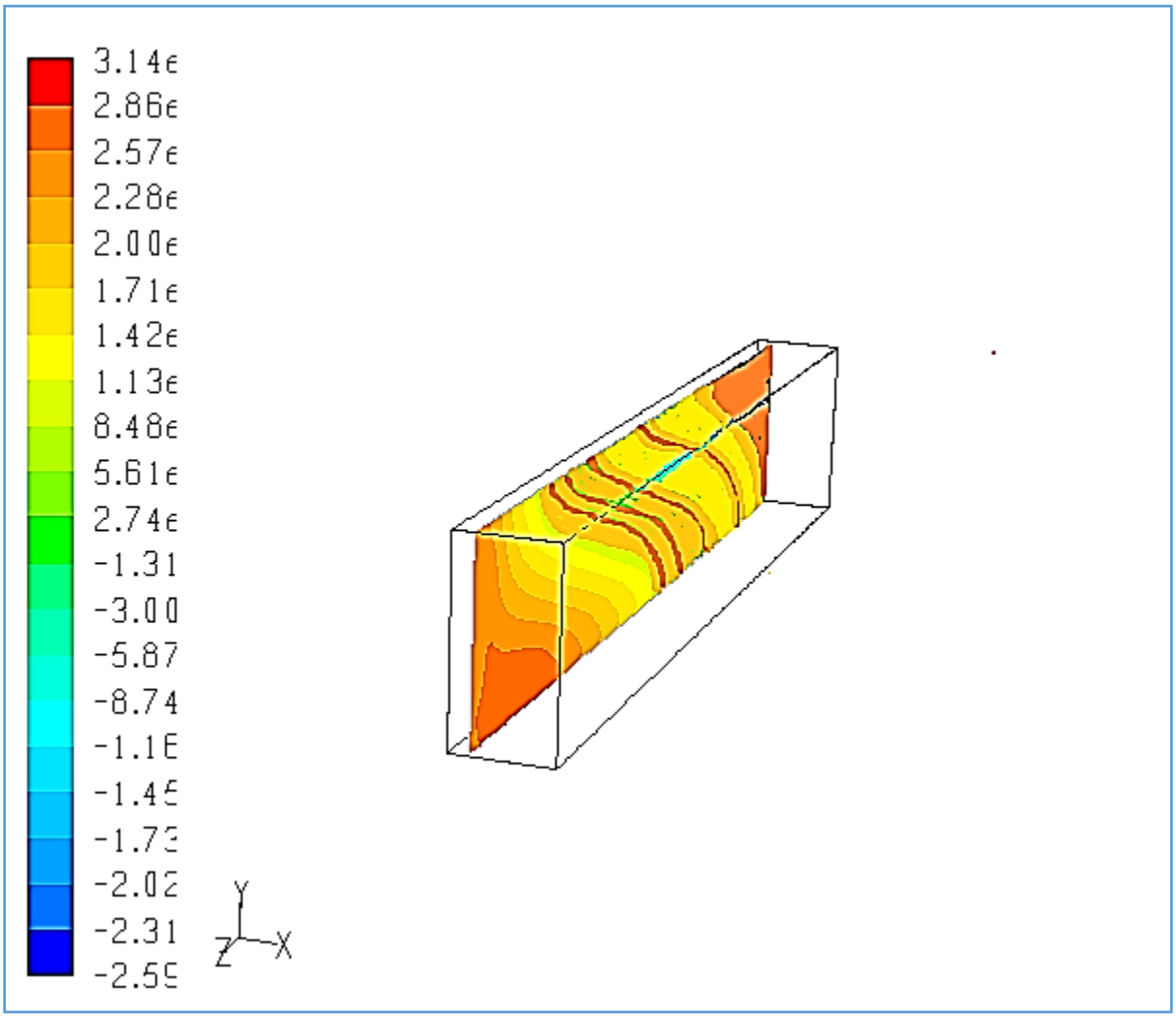

Fig. 5.27 Contours of Static pressure at X=0.1

Figure 5.27 and figure 5.28 show the profiles of static pressure at X=0.1 and at X=0.5. From figure 5.27, static pressure is generally high near the hot surface.

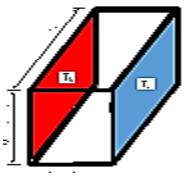

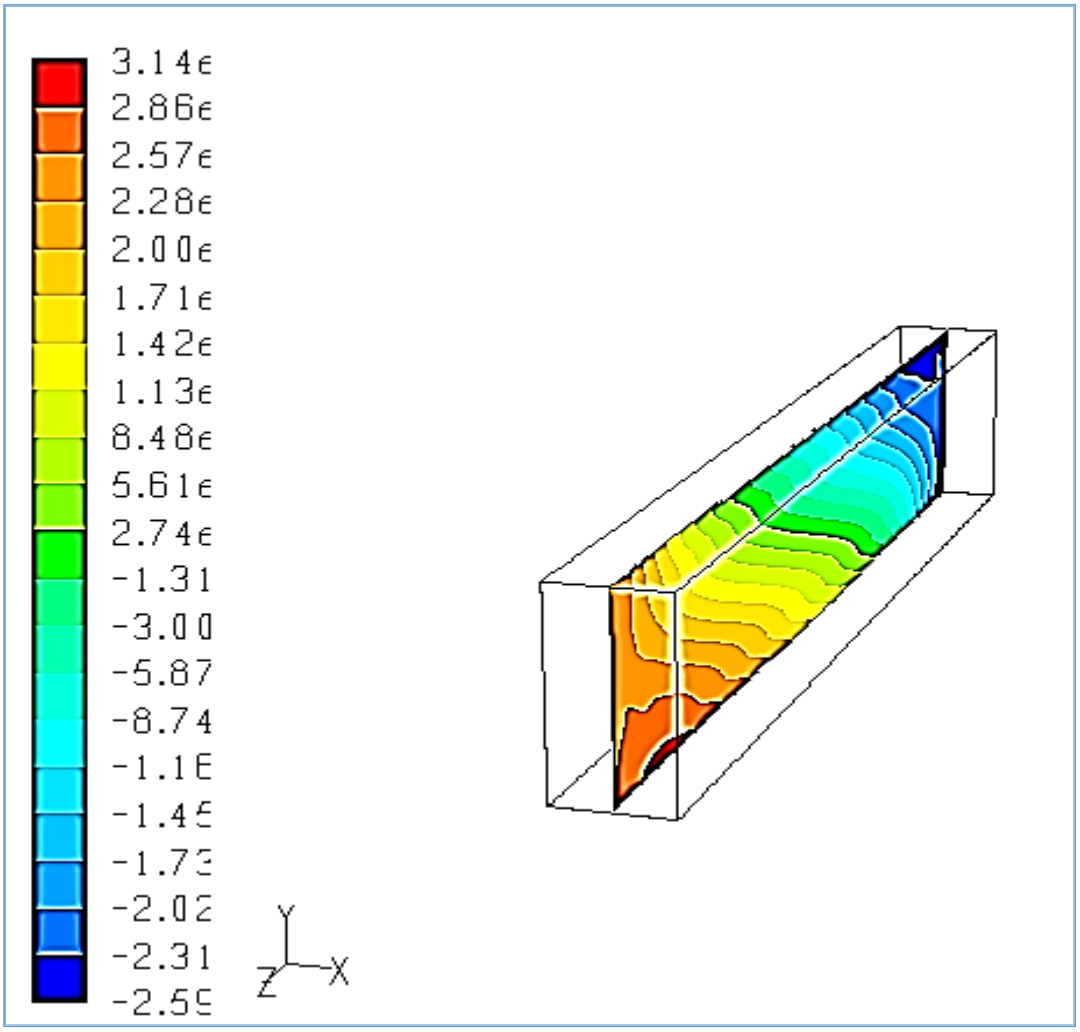

Figure 5.28 Contours of Static Pressure at X=0.5

This is because the generated pressure, due to buoyancy driven convective currents, is more intense near the hot surface as is evident from the color codes of static pressure. Given that the pressure is a function of the buoyancy, as the bouyancy force increases, Static Pressure increases accordingly.

At the confluence of the thermally active surfaces, static pressure decreases away from the front wall due to the direction of the convective currents as shown in figure 5.18. Fluid pressure is proportional to the frequency with which the cavity wall is hit by the particles so the rate of mass increase on the front wall is higher than at the back.

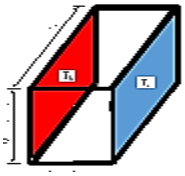

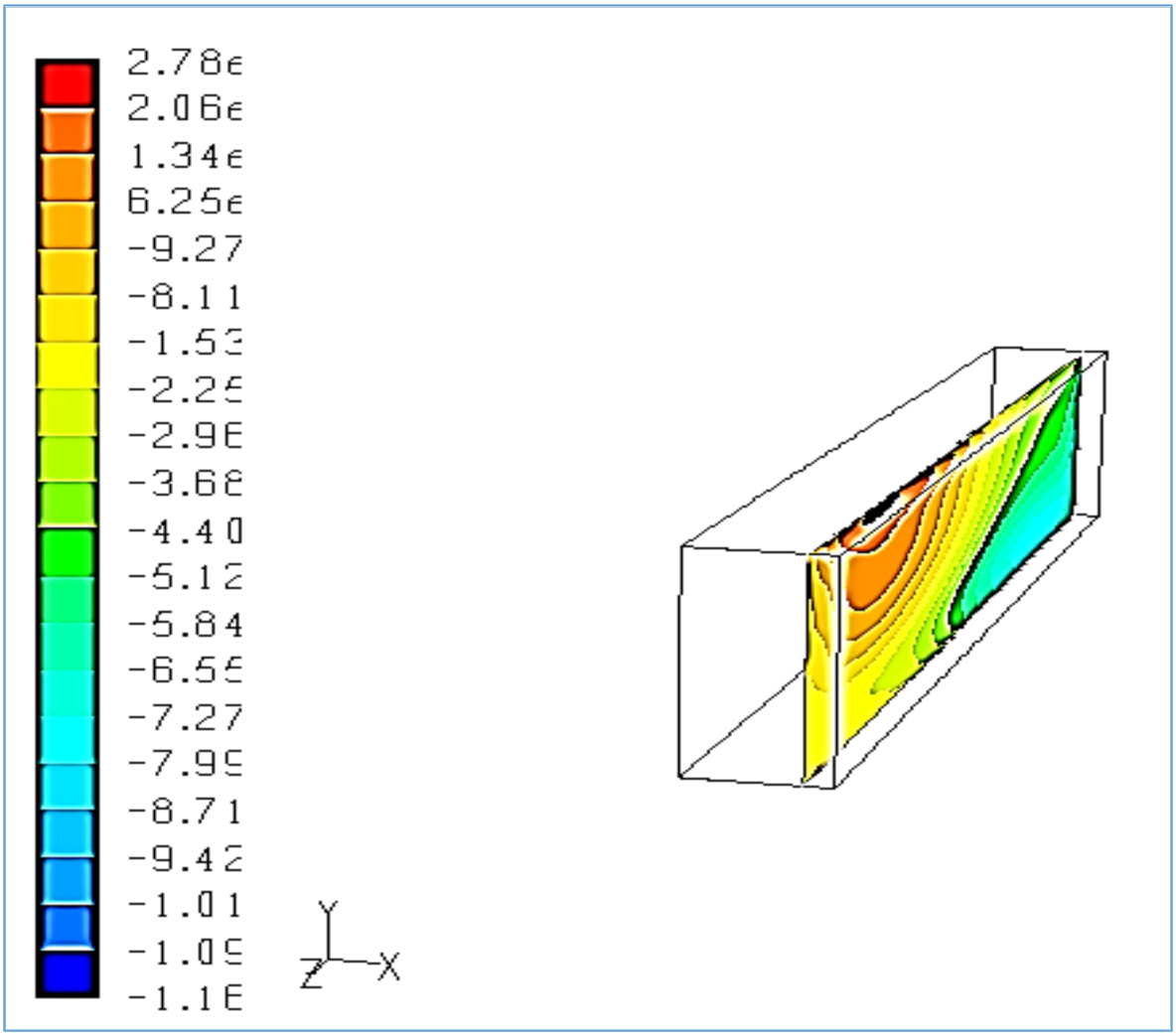

Fig 5.29 Contours of Static Pressure at X=0.9

On the contrary, it is evident that the static pressure, near the cold side decreases downwards, owing to the motion of the fluid particles downwards after being cooled, as shown in figure 5.29. The pressure is intense at the top given the thermally induced energy of the oncoming stream, after diffusivity at the confluence, but the kinetic energy dies out gradually after the heat dissipation due to the local minimum temperature along the window.

Generally, there is more static pressure near the hot surface than on the cold side of the cavity given that, the conventional currents move from right, via the floor, to left before turning back, as shown in figure 5.14. So pressure increases when the hot surface is bombarded more by on-coming cold conventional current.

5.8 Static Pressure Profiles by SIMPLEC Method

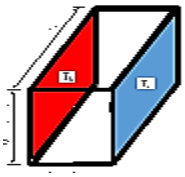

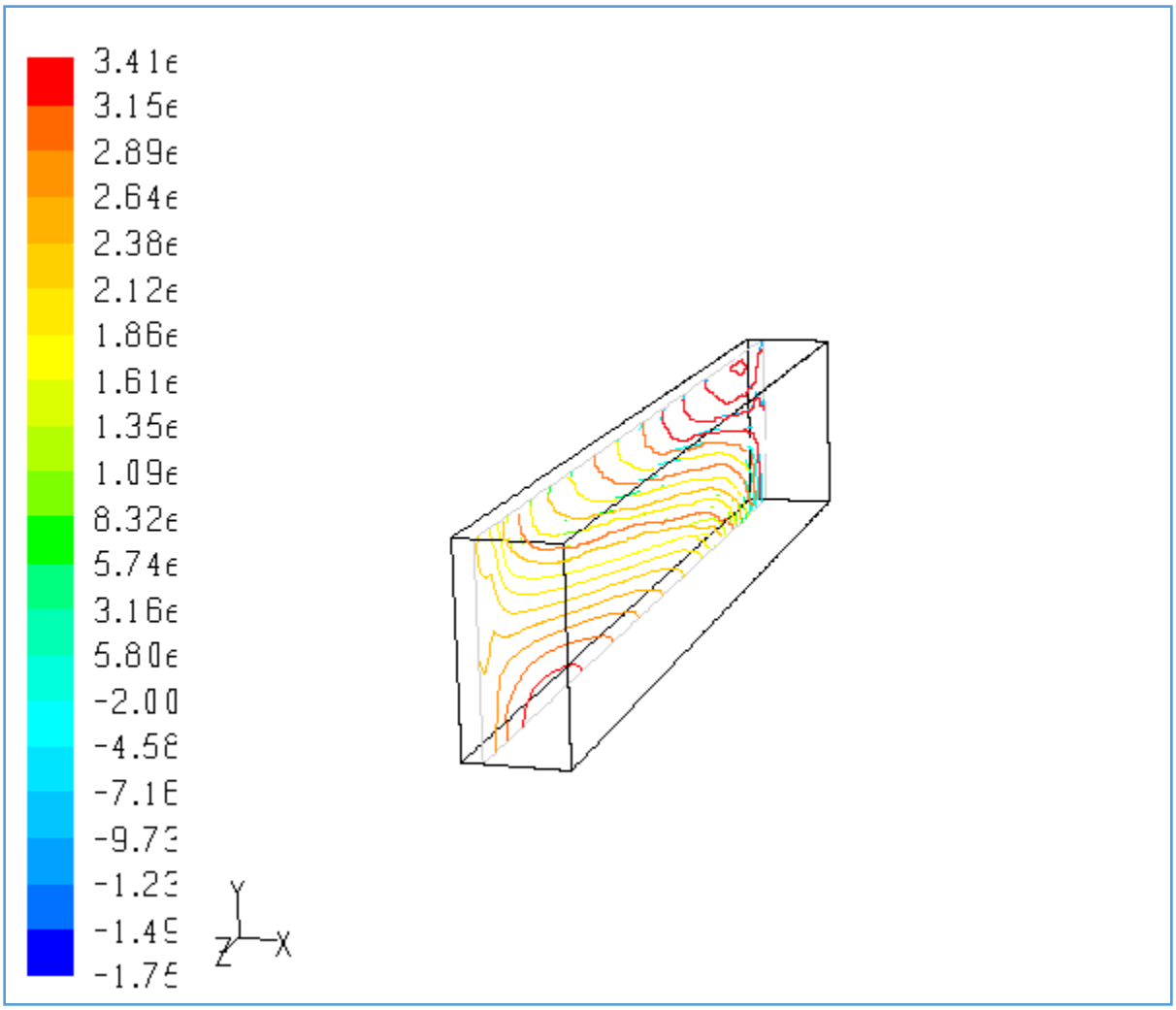

Fig. 5.30 Contours of Static pressure at X=0.1

Figure 5.30 and figure 5.31 show the profiles of static pressure at X=0.1 and at X=0.5. From figure 5.30, static pressure is generally high near the hot surface. This is because the generated

pressure, due to buoyancy driven convective currents, is more intense near the hot surface as is evident from the color codes of static pressure

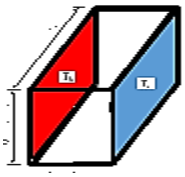

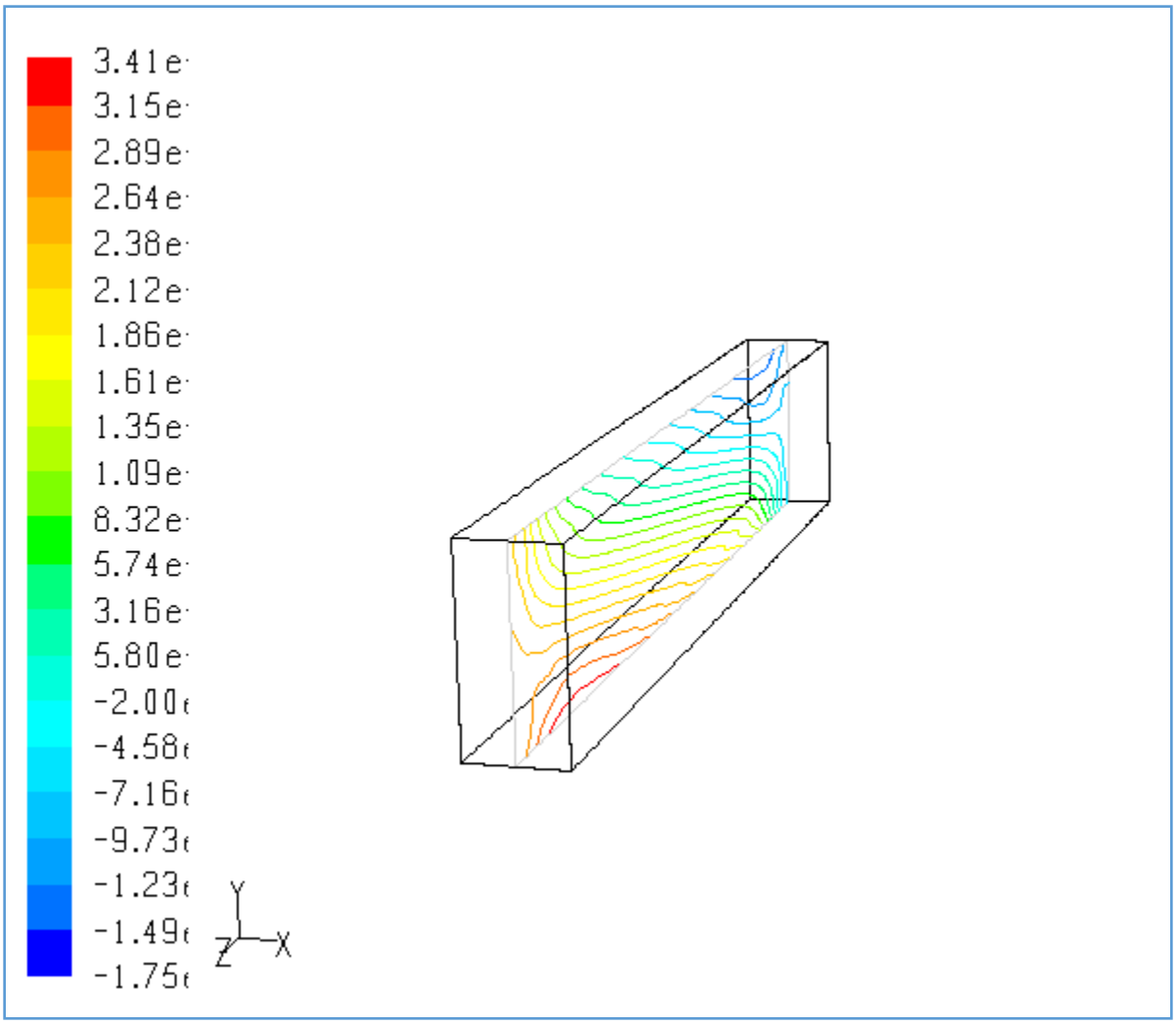

Fig. 5.31 Contours of Static pressure at X=0.5

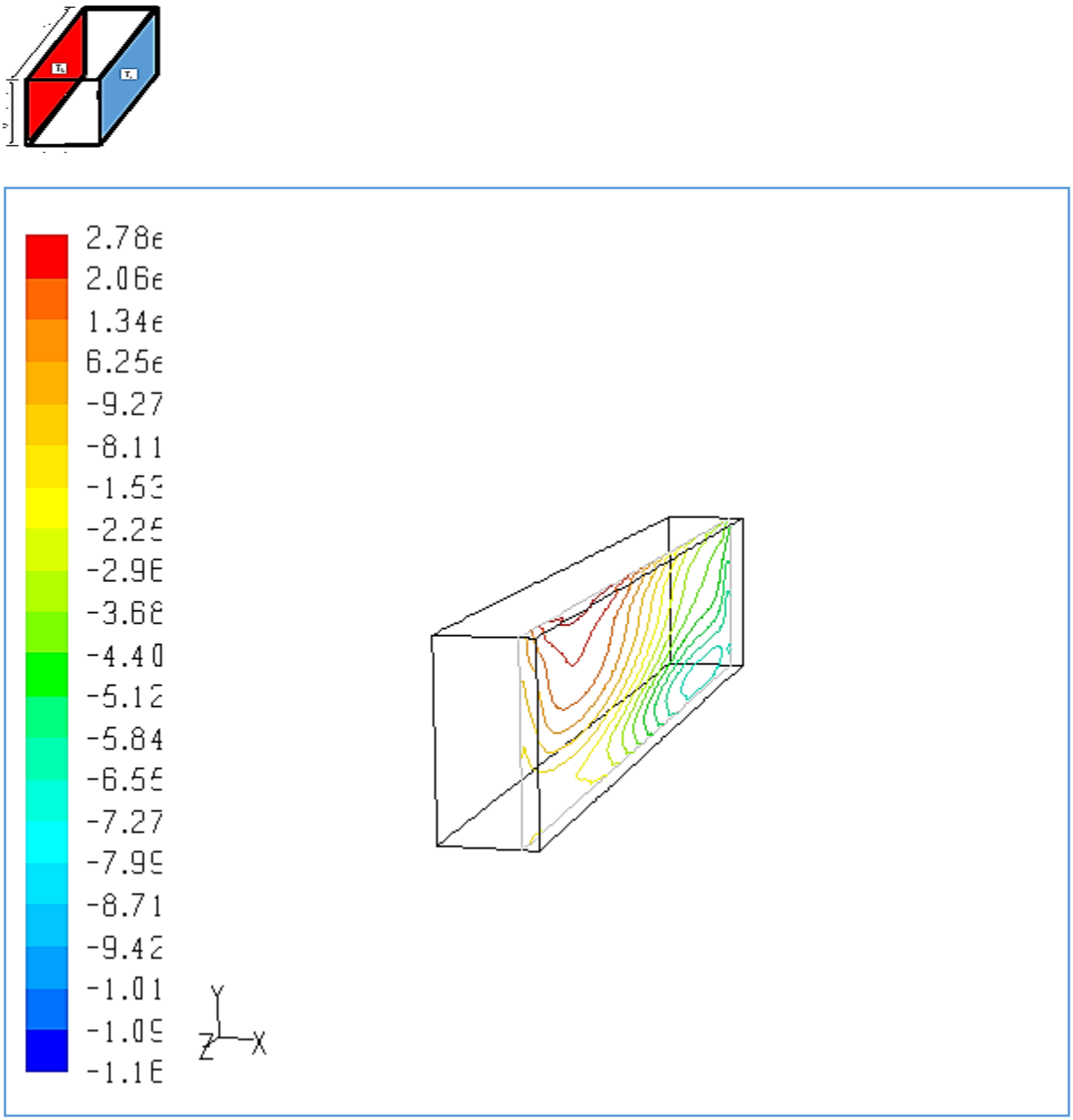

Fig. 5.32 Contours of Static pressure at X=0.9

There is though a striking similarity between these pressure profiles and pressure profiles by PISO method. The profiles by SIMPLEC appear to be less intense than those by PISO method due to lower velocity gradients and lower dynamic viscosity values.

5.9 Temperature Profiles between the Isothermal Walls by PISO Method

The flow movement of the convection is initialized by the temperature difference between the vertical walls. Thus, the temperature profile is one important aspect to understand the dynamics of the flow. Figure 5.33 displays the typical temperature and profile at Z=0.5.

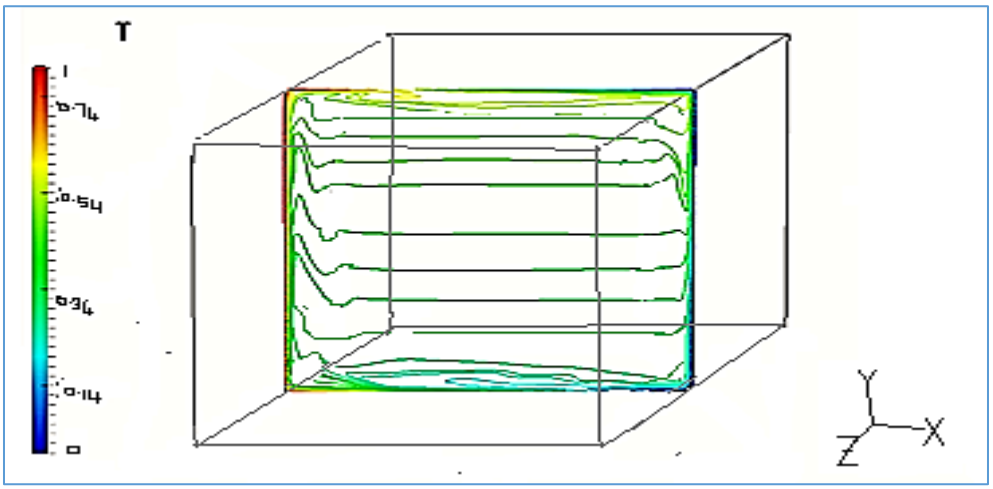

Fig 5.33 Temperature Isotherms at Z=0.5

The buoyancy induced motion of air in the enclosure is in a state of turbulent flow because the thermal boundary layer is thin along the walls while the core is thermally stratified. The flow gradient is very large in the boundary layer. This boundary layer is the source of skin friction drag, shear stress and buoyancy and has actually decreased pressure drag, a force that would pull kinetic energy out of the air as justified by high turbulent kinetic energy as shown in figure 5.7. A turbulent layer friction has affected the airflow more in the outer region of the turbulent flow layer given the no slip boundary condition in this study. The thermal boundary layer near the

heated walls and a variation of its thickness along the heated walls can clearly be seen. Further, a dependence on the particular boundary condition is visible.

5.10 Wall Shear Stress along the Heated Walls

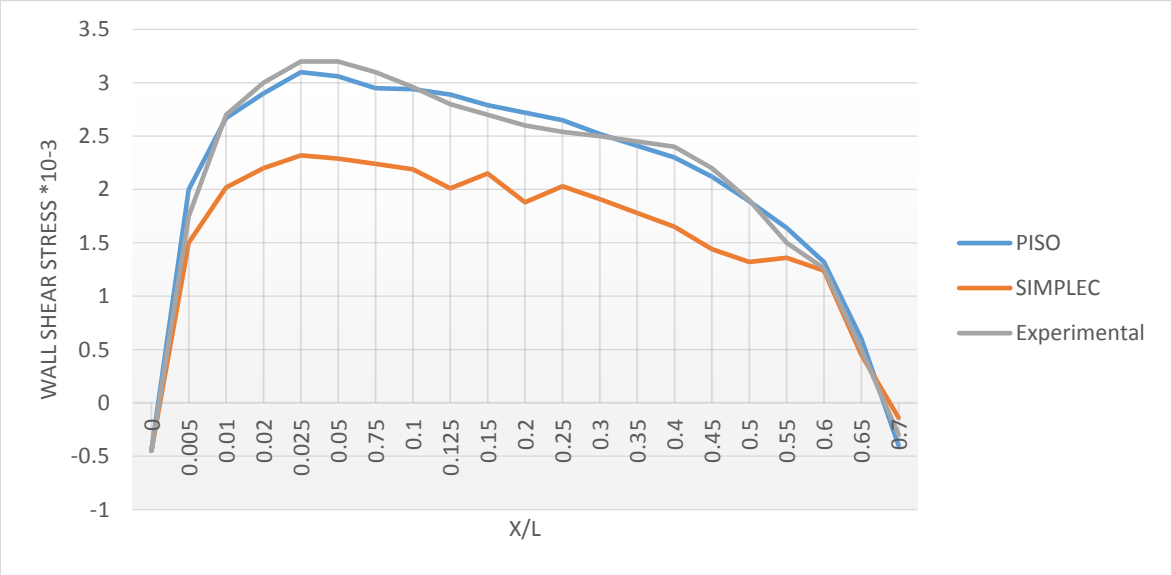

Fig 5.34 Wall Shear Stress Profile at Z=0.5

Figure 5.34 shows wall shear stress profiles between the thermally active walls.

This is the shear stress in the fluid next to the wall. Wall shear stress is proportional to the velocity gradient of the fluid next to the wall and it is the product of dynamic viscosity and wall shear stress rate as compared with equation (5.1);

$$T_w = \mu(\frac{\partial u}{\partial x})_{y=0} \qquad (5.1)$$

where μ, $\frac{\partial u}{\partial x}$, and y are the dynamic viscosity, velocity gradient near the wall (wall shear stress rate) and distance to the wall respectively.

Since wall shear stress is directly proportional to wall shear stress rate, it follows that;

i) It falls and rises with the fall and rise of velocity along the vertical heated walls

ii) The simulation profiles show an asymmetrical form, which is founded in the asymmetrical velocity profile.

iii) The values along the heated walls in this study for PISO are higher than those of SIMPLEC due to higher velocity gradients and higher dynamic viscosity values.

iv) The simulation reveals negative values in the top hot and bottom cold corner which indicate anti-clockwise vortex regions since negative wall shear stress implies negative velocity gradient indicating the fluid is rotational and there is presence of eddies. This is the result of the eddies that are evident in the cavity at Y=0 and Y=1 in figure 5.13

5.11 Velocity Profiles between the Isothermal Walls by PISO Method

Shows a snapshot of the horizontal velocity isotherms at the mid XY-plane. The plot reveals an exterior circulation zone as well as an interior one. The exterior circulation zone indicates a unicellular convention behavior where a buoyancy induced single cell of conventional current flows clockwise along the walls. The interior circulation zone indicates a bi-cellular convectional behavior where two buoyancy induced cells of conventional currents, flow in a clockwise direction, one near the hot and the other near the cold surface.

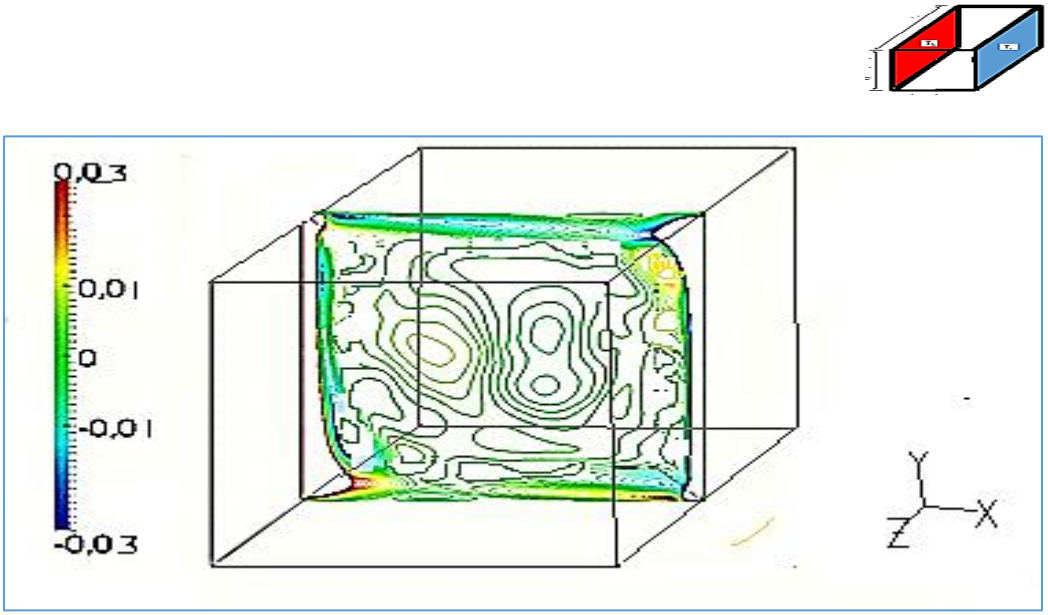

Fig 5.35 Horizontal velocity profiles at Z=0.5

The left cell is driven by the heater while the right cell is driven by the window. Furthermore, (i) smaller circulations appear additionally in the bottom left and top right corner as well as top left and bottom right corner (ii) the simulations reveal negative values in the top hot and bottom cold corner which indicate anti-clockwise vortex regions (iii) Velocity boundary layer is thicker than the thermal boundary layer (figure 5.33), hence convective heat transfer is more significant than conduction for turbulent natural convective transport mechanism in a 3-D enclosure. These simulations indicate the formation of re-circulation structures of non-zero vorticity, which portray rotationality and hence regions of high turbulence. The horizontal velocity component reveals peak values close to the vertical, heated walls.

In the next chapter, the conclusions drawn from numerical data will be stated, recommendations made and suggestions for further studies given.

CHAPTER SIX

SUMMARY, CONCLUSIONS AND RECOMMENDATIONS

The conclusions and recommendations made in this chapter are based on the results discussed in chapter six. Basing on the validations in chapter five, our code is correct and the results are reliable.

6.1 Summary

The purpose of this study has been to carry out a numerical investigation of turbulent natural convection in a 3-D enclosure using the *k-ω SST* model and the PISO method.

The objectives were achieved as follows

i) Numerical data, for SIMPLEC method using the *k-ω SST* models for the temperature and velocity near the hot wall and the cold wall, was obtained and discussed.

ii) Simulated data for velocity and temperature, obtained using PISO algorithm, SIMPLEC algorithm and the two- equation *k-ω SST* model, near the hot wall and the cold wall was compared.

iii) The change in velocity profiles, temperature profiles, convergence time, stability and accuracy of the numerical method and any additional findings, when the primitive variable, not the vorticity vector potential formulation, is employed to solve the momentum equation, was determined.

iv) The better method in terms of convergence, stability and accuracy between PISO method and SIMPLEC method was determined in carrying out numerical investigation of turbulent natural convection in a 3-D cavity, was determined.

v) Numerical results were validated using experimental benchmark data found by Ampofo *et al.* (2003), conclusions based on the numerical data were made and recommendations for future studies given.

6.2 Conclusions

Based on the data from the simulations, the following conclusions were obtained;

i) In this thesis,

   a) Different temperature conditions resulted in two large cells in circular motions, both of which rotate in a clockwise direction.

   b) Both the experimental data and simulation using PISO return a non-dimensional temperature of 0.5 at the core of the cavity and almost zero towards the cold

   Therefore

   a) The results show that in an enclosure environment, the natural turbulence flow is responsible for temperature distribution.

   b) Temperature profiles are important for thermal comfort (including air velocity, temperature and humidity levels), efficiency of energy balance and the effectiveness of the ventilation system when modeling air flow in buildings.

ii) Turbulent natural convention behavior, for air in the cavity, obeys the unicellular convection behavior, which underscores the importance of the present study in the room

air distribution to facilitate room ventilation in order to eradicate moisture, dust, smoke, carbon dioxide and airborne bacteria like mycobacterium tuberculosis, varicella zoster, plasmodium falciparum, Rhino virus and Trycophyton rubrum.

iii) From the numerical results obtained, velocity and thermal profiles have a good agreement (Figures 5.6, 5.7, 5.10, 5.35). So, use of $k-\omega\,SST$ model to model the non-linear turbulent correlations and the primitive variable to solve the momentum equation brings out aspects of the flow that would otherwise have been subdued by body and surface forces in the absence of an extremely fine mesh.

iv) The flow is characterized by low Reynolds turbulence intensity and thermal stratification which provides thermal options of keeping items at the stated temperature in an enclosure without the use of an internal heat source. Like health facilities, the transit, handling, and storage of temperature-controlled drug products within complex supply

v) Optimal conditions for an actively growing plant, in greenhouses, are an air temperature of 293K to 300K, 60-80% relative humidity and 20-100 photo-synthetically active radiation (PAR); the kind of thermal variables that fall within the confines of data used in this study. The profiles findings in this thesis would be very instrumental in accomplishing greenhouse temperature control using the cheaper options like natural ventilation and shading.

vi) Physical characteristics of indoor environment in stadia, as in thermal conditions, humidity levels, air velocity, static pressure profiles, thermal conditions, indoor humidity, and pressure differences across the building envelope, draught and noise affect human responses individually and collectively. Hence, the static pressure, thermal and velocity profiles predicted in this thesis would provide a basis to make building codes that could ensure quality, healthy properties and sustainable use of natural resources like energy.

vii) It is now possible to solve numerically the strong coupling between velocity and pressure in the RANS equations at high Rayleigh numbers, using FVM, $k-\omega\, SST$ model and PISO.

viii) The data for thermal profiles found in this thesis can be helpful in determining and controlling the micro-climate in poultry houses for the thermal comfort of the birds such as temperature, relative humidity, air composition, air speed and air movement for poultry's optimum performance.

ix) From the numerical data, the numerical method produced a solution which approached the exact solution by Ampofo and Karayiannis (2003) as the grid spacing reduced to zero. Further, the method is stable, the governing equations consistent. Therefore using Lax's equivalence theorem, Lax and Richtmyer (1956), this code is valid, stable and consistent.

x) Both PISO and SIMPLEC algorithms converge to the same solution. But with differences in speed and stability. Therefore, for turbulence natural convection kind of flows, PISO

algorithm is faster and more numerically elaborate, stable and accurate than SIMPLEC algorithm because, besides the quoted evidence, it allows for the use of larger under-relaxation factors than SIMPLEC.

xi) The thermal boundary layer is thinner than the velocity boundary layer (Figures 5.33 and 5.36). This means, fluid temperature within the enclosure increases, not by flowing from isothermal wall into the bulk of the air, but by natural turbulent transport mechanism. Hence, convective heat transfer is more significant than conduction and air flow in this enclosure (Figure 3.3) is characterized by high momentum convection and low momentum diffusion.

xii) The use of the primitive enabled the solution to converge after just 250 iterations in CPU time of 45 minutes. For vorticity-vector potential formulation, Awuor (2012), the $k-\omega\ SST$ model took 1 hour to converge after 1000 iterations. Hence the use of PISO method coupled with the $k-\omega\ SST$ model is an improvement in terms of convergence time and speed since it is easy to fix boundary conditions, computational effort per unit time (figure 5.4), faster diminishing of the absolute error and solving the pressure term and as a result, profiles for wall shear stress and static pressure can be obtained

xiii) The use of FVM and PISO technique is an improvement on the use of FND to discretize and vorticity vector potential formulation to solve the time averaged momentum equations as per Awuor (2012) in terms of

a) The primitive method being extended to 3-D

b) Conserving variables regardless of the cell shape.

Because of (a) and (b), it brings out non-deterministic properties as 3-D rotationality, diffusivity, 3-D static pressure and wall shear stress profiles. Therefore mass, momentum and energy are conserved better and turbulent fluctuations in all directions can be accounted for.

6.3 Recommendations

Based on the comparison of the results obtained in this work with those obtained experimentally obtained benchmark results by Ampofo and Karayiannis (2003) we recommend Finite Volume Method, the *k*-≤SST model and PISO method for

i) Cases of coupled, non-linear, partial differential equations where an implicit solution is required.

ii) Solutions for pressure-velocity linked equations in which a staggered grid is required in order to obtain a strong coupling between velocity and pressure.

iii) Predictions of high speed and large flow problems that require less CPU time, more stability and more accuracy.

iv) Turbulent flows with Reyleigh number $\geq 10^9$ because such flows are characterized by large flow gradients and therefore require flexible spatial discretization and large memory capacity in order to capture the flow physics in the regions of adverse pressure gradients.

6.3.1 Suggestions for Further Studies

1. In this study, we used an incompressible fluid. We suggest that further numerical investigation can be conducted of the rectangular cavity using compressible fluids.

2. We suggest that a parametric study be undertaken in an air-filled rectangular enclosure for a colliding boundary layer problem that is where only one wall is heated and cooled, not opposite walls.
3. It is suggested that further investigation of the effect of surface material and radiation properties on air flow in an enclosure be undertaken.
4. It is suggested that Reynolds Stress Model can be used to compare the PISO method and the vorticity vector potential formulation to investigate the 3-D enclosure for air.

REFERENCES

Ampofo F. and Karanyiannis T. G. (2003), Experimental Benchmark Data for Turbulent Natural Convection in an Air-Filled Square Cavity, *Intenational Journal of Heat Mass Transfer*, **46**, 3551-3572.

Awuor K. (2012), Turbulent Natural Convection in an Enclosure: Numerical Study of Different k-epsilon models, Ph.D. Thesis, Kenyatta University, Kenya, 1-102.

Berghein C., Penot F., Mergui S. and Allard F. (1993), Numerical and experimental evaluation of turbulent models for natural convection simulation in a thermally driven square cavity, *Proceedings on Adaptive Selection Mode Error Concealment (ASMEC) Conference*, 1-12.

Bird R. B., Steward W. E. and Lightfoot E. N. (2007), Transport Phenomenon, Wiley & Sons Inc., **2**, 1-54.

Boussinesq J. (1903), Th´eorie Analytique de la Chaleur, Gauthier-Villars, *the Astrophysical Journal*, **136**, 1126.

Cebeci T. and Smith A. M. O. (1974), Analysis of Boundary Layers, Applied Mathematics and Mechanics, Academic Press, New York, **15**, 4-45.

Davidson L. and Nielsen P.V. (1996), Large Eddy Simulations of the Flow in a Three-Dimensional Ventilated Room, *Proceedings Roomvent '96*, **2**, 161-168.

Dol H. S. and Hinjalic K. (2001), Computational Study of Turbulent Natural Convention in a side Heated Near-cubic Enclosure at High Re, *International Journal of Heat and Mass Transfer*, **4**, 2323-2344.

Eckert E. R. G. (1950), Introduction to the Transfer of Heat and Mass, **1**, 3-98.

Faghri, A., Zhang y. and Howell J. (2010), Advanced Heat and Mass Transfer, Global Digital Press, 2-100.

Gatheri F. K. (2005), The use of Mesh Generation Functions for the Solution of Natural Convection Problems, *East African Journal of Physical Sciences*, **6** (1), 21-31.

Gatheri F. K. (2005), Variable False Transient for the Solution of Coupled Elliptic Equations, *East African Journal of Physical Sciences*, **6** (2), 117.

Gatheri F. K., Reizes J., Leonardi E. and Graham V. D. (1993), The use of Variable False Transient Factors for the Solution of Natural Convection Problems, *Australian Heat and Mass Transfer Conference*, University of Queensland, **5**, 68-69.

Gatheri F. K., Reizes J., Leonardi E., and Graham V. D. (1994), Natural Convection in an Enclosure with Localized Heating and Cooling: A numerical Study, Heat Transfer, G.F. Hewitt, **2**, 361-366.

Harlow F. H, Nakayama P. I. (1968), Transport of Turbulence Energy Decay Rate, Los Alamos Science Labaratory, LA-3854, 86-127.

Harlow F. H. and Welch J. E. (1965), Numerical Calculation of Time-Dependent Viscous Incompressible Flow of Fluid with Free Surface, *The Physics of Fluids*, **8**, 2182-2189.

Hatsopolous, G. N. and Keenan J. H. (1965), Principle of General Thermodynamic, John Wiley and Sons Inc., 123-190.

Hewitt, Duncan R., Jerome A., Lister R., and John R. (2014), High Rayleigh Number in a Three-Dimensional Porous Medium, *Journal of Fluid Mechanics*, **748**, 879-895.

Incropera, DeWitt, Bergman and Levine (2007), Introduction to Heat Transfer, Wiley & Sons Inc., **5**, 234-518.

Ingham D. B. (1978), Free-Convection Boundary Layer on an Isothermal Horizontal Cylinder, *Journal of Applied Mathematics and Physics*, **29**(6), 871-883.

Jiyuan T., Guan H. Y. and Chaoqun L. (2012), Computational Fluid Dynamics, A Practical Approach, Elsevier Inc., **2**, 1-404.

Jones P. J. and Whittle G. E. (1992), Computational fluid dynamics for building air flow prediction current status and capabilities, *Building and Environment*, **27** (3), 321-338.

Jouvray A. and Tucker P. G. (2005), Computation of the flow in a ventilated room using non-linear RANS, LES and hybrid RANS/LES, *International Journal for Numerical Methods in Fluids*, **48** (1), 99 – 106.

Jouvray A., Tucker P. G. and Liu L. (2007), On Nonlinear RANS models when predicting more complex geometry room airflows, *International Journal of Heat and Fluid Flow*, **28**, 275–288.

Kays, William, Crawford, Michael, Bernhard and Weigand (2005), Convective Heat and Mass Transfer, McGraw-Hill, **4**, 200-448.

Keating A. and Piomelli U. (2006), A Dynamic Stochastic Forcing Method as a Wall-layer Model for Large- Eddy Simulation, Journal of Turbulence, **7**, 12-20.

Krepper E. and Rzehak, R. (2011), CFD for Sub-cooled Flow Boiling: Simulation of DEBORA Experiments, Elsevier B.V., 84-126.

Krepper, E., Koncar B. and Egorov Y. (2006), CFD Modeling of Sub-cooled Boiling – Concept, Validated and Application to Fuel Assembly Design, Elsevier B. V., 231-302.

Launder B., Reece G. and Rodi W. (1975), Progress in the development of a Reynolds-stress turbulence closure, *Journal of Fluid Mechanics*, **68** (3), 537-566.

Launder B. E. and Spalding D. B. (1974), The numerical computation of turbulent flows, *Computational Methods in Applied Mechanics and Engineering*, **3**, 269-289.

Lax P. D. and Richtmyer R. D. (1956), Survey of the Stability of Linear Finite Difference Equations, *Communications on Pure and Applied Mathematics*, **9**, 267-293.

Menter F. R. (1994), Two-equation eddy viscosity turbulence models for engineering applications, *The American Institute of Aeronautics and Astronautics (AIAA) Journal*, **32** (8), 1598-1605.

Nielsen P. V. (1974), Flow in Air-Conditioned Rooms, Ph.D. Thesis, Technical University of Denmark, Copenhagen, Denmark, 24-116.

Okwoyo M. J., Okello J. A., Sigey J. K. and Mairura O. E (2013), Natural Convection With Localized Heating and Cooling on Opposite Vertical Walls in an Enclosure, *The Standard International Journals (SIJ) Transactions on Computer Networks Communication Engineering (CNCE)*, **1**(4), 72-78.

Ostrach S. (1953), An analysis of laminar free-convection flow and heat transfer about a flat plate parallel to the direction of the generating body force, NACA, Report 1111, Madison, 64-79.

Pantaker S. V. (1980), Numerical Heat Transfer and Fluid Flow, Series in Computational Methods in Mechanics and Thermal Sciences, Hemisphere Publishing Corporation, **1**, 25-39.

Prandtl L. (1945), A new representation of fully developed turbulence, Jet Propulsion Labaratory Publication (JPL-P), **13**, 6-19.

Peng S. H. and Davidson L. (2001), Large eddy simulation for turbulent buoyant flow in a confined cavity, *International Journal of Heat and Fluid Flow*, **22**, 323-331.

Peng S. H. and Davidson L. (1999), Computation of turbulent buoyant flows in enclosures with low Reynolds-number k-ω models, *International Journal of Heat and Fluid Flow*, **20**, 172-184.

Reynolds O. (1894), Dynamical theory of turbulent incompressible viscous fluids and the determination of the criterion, Phil. Trans. R. Soc. London A, **186**, 123-161.

Shur M., Spalart P. R., Strelets P. R. and Travin A. (1999), Detached-Eddy Simulation of an Airfoil at High Angle of Attack, *4th International Symposium on Engineering Turbulence Modeling and Experiments*, **4**, 669-678.

Sigey J. K., Gatheri F. K. and Kinyanjui M. (2004), Numerical Study of free Convection in an Enclosure, Ph.D. Thesis, Jomo Kenyatta University of Agriculture and Technology, Kenya.

Sigey J. K., Gatheri F. K. and Kinyanjui M. (2004), Numerical Study of free Convection in an Enclosure, *Energy Conversion and Management*, **45**, 2571-2582.

Spalart P. R., Jou W. H., Stretlets M. and Allmaras S. R. (1997), Comments on the feasibility of LES for wings and on the hybrid RANS/LES approach, *Proceedings of the First AFOSR International Conference on DNS/LES*, **1**, 4-8.

Squires K. D. (2004), Detached-Eddy Simulation: Current Status and Perspectives, Proceedings of Direct and Large-Eddy Simulation, *Journal of Turbulence*, **5**, 10-15.

Tennekes H. and Lumley J. L. (1972), A First Course in Turbulence, The MIT Press, 20-41.

Thompson C. P., Wilkes N.S. and Jones I. P. (1987), Numerical studies of buoyancy-driven turbulent flows in a rectangular cavity, *International Journal for Numerical methods in engineering*, **24**, 89-99.

Tian, Y. S. and Karayiannis, T. G. (2000), Low Turbulence Natural Convection in an Air Filled Square Cavity, *The Thermal and Fluid Flow Fields. International Journal of Heat and Mass Transfe*r, **43**, 849-866.

Tong, L. S. (1965), Boiling heat Transfer and Two-Phase Flow, Wiley & Sons Inc., **2**, 11-65.

Wilcox D. C. (1998), Turbulence modeling for Computational Fluid Dynamics, DCW Industries Inc., Canada, **2**, 103-217.

Zimmermann C. (2014), Modelling Turbulent Heat Transfer in a Natural Convention Flow, *Journal of Applied Mathematics and Physics*, **2**, 662-670.